12-8-2006

Enhancements of a three dimensional target model for deep ground penetrating radar systems

Lonnie Parker

Enhancement of a Three Dimensional Target Model for Deep Ground Penetrating Radar Systems

By

Lonnie T. Parker, IV

A Thesis Submitted

In Partial Fulfillment of the

Requirements for the Degree of

MASTER OF SCIENCE

In

Electrical Engineering

Approved by the
Thesis Committee:

_____
Dr. Vincent J. Amuso, Electrical Engineering Dept. Head, Thesis Advisor

_____
Dr. Sohail Dianat, Professor/ Graduate Program Chair, Electrical Engineering

_____
Dr. Eli Saber, Associate Professor, Electrical Engineering

Rochester Institute of Technology
Rochester, NY
November 2006

I, Lonnie T. Parker, IV, hereby grant permission to the Wallace Library of the Rochester Institute of Technology to reproduce my thesis in whole or in part. Any reproduction will not be for commercial use or profit.

Date:_____ Signature of Author:_____

Table of Contents

List of Tables

List of Figures

Acknowledgements

I would first like to thank my Lord and Savior, Jesus Christ, through whom all things are possible. Second, I would like to thank my parents for their support, love and continued guidance during my time in school. Third, I would like to thank my advisor, Dr. Amuso, for giving me the freedom to develop my own understanding of Electrical Engineering and for his patience and advice during this process. I'd like to thank my thesis committee, the faculty and staff of the Electrical Engineering department. A special thank you also goes to Ms. Patti Vicari, Ms. Florence Layton, and Ms. Jill Lewis for their own contribution to my education. It has been a wonderful experience at RIT and I am greatly appreciative to all those who have helped me throughout my time here.

Abstract

Both commercial and military industries incorporate the use of Ground Penetrating Radar (GPR). In the case of the military, a stationary object, such as a bunker or tunnel, can be detected. Even high-resolution, three-dimensional (3D) and two-dimensional (2D) imagery of energy reflected by the target and its surrounding environment can be produced. This is accomplished using multiple scene perspectives inherent in advanced Synthetic Aperture Radar (SAR) techniques.

Although underground target detection can be successful, the return data, usually suffers a significant degree of signal degradation due to the ground medium and target composition. A valid theoretical target model must account for adverse affects such as specular and diffuse reflections, dispersion and attenuation in order to provide an accurate representation of the simulated GPR scenario.

It is the aim of this thesis to demonstrate the benefits of a high fidelity GPR target model. Demonstrated in the model is the ability to record estimative return power as a function of multiple variables including frequency, target depth, target composition, ground medium, complex antenna patterns, and transmitted power. Using ray-tracing, a bidirectional reflectance distribution function (BRDF), and 3D geometric analysis, the specular and diffuse reflective and refractive sub-surface energy interactions known to take place for a spatially complex target are simulated. Results culminate in the comparison of 3D and 2D imagery generated using this target model with imagery generated using previous models.

Chapter 1

Introduction

Radar systems are an effective tool for obtaining information about a particular object in a specific location. Whether that object is an airborne commercial craft or a military base on the ground, different types of radars have been designed, tested, and proven to provide accurate detail about a target's geographical position, speed, heading, etc. There is a direct relationship between the amount of information that radar can provide and its usefulness in a real-world application.

GPR holds significant weight in various applications. This technology is extremely useful as it satisfies both a commercial need such as evaluating the homogeneity of soil for valid construction sites, as well as a military need in the case of locating stationary targets such as bunkers and tunnels used of enemy forces.

When considering the target's location, size and shape, along with a host of other variable system parameters (i.e. frequency, ground properties, antenna type, etc.), it is advantageous to have a software tool available that allows different experimental scenarios to be simulated. By providing preliminary predictions as to what a particular target scenario might reveal during post-processing of experimental data, time and money can be saved when developing an actual hardware representation of the simulation tool.

At the RIT Radar Lab in Rochester, NY, such a simulation tool has been under development. The simulated GPR considered is a bistatic synthetic aperture radar system. This allows the use of separate transmit and receive antennas (bistatic) along with multiple receiver locations (SAR) to allow for a higher resolution system than most mono-static radars currently allow. The software has been designed to model the complex

energy interactions that take place underground when a target of homogeneous composition is illuminated with electromagnetic energy by this system. The simulation tool then renders a 3D image of that target using SAR signal processing techniques.

The techniques used to model the propagation of electromagnetic waves and the unique transmission and reflection properties are the ray-tracing concept and the BRDF [11]. Based on the particle-like behavior of electromagnetic energy, these waves are approximated as a series of straight beams or rays. Methods to describe and record their interaction with matter include fundamentals of geometric physics. This technique only allows for the limited modeling of specular reflection, transmission, and path attenuation calculations. The BRDF incorporates the diffuse, dispersive, and diffractive elements inherent in a signal when electromagnetic energy is incident upon a surface. These interaction phenomena are accounted for, in combination with the ray-tracing technique to form an accurate GPR target model.

1.1 Problem Statement

Since 2001, the GPR software has been upgraded by previous RIT Master's students, each one contributing their own improvements. Ray-tracing was initially implemented to extend the capabilities of the software to simulate energy reflections of rectangular targets of varying width, height and depth [1]. Where ray-tracing fell short in only accounting for specular reflections, this was followed by the implementation of a customizable BRDF to allow simulation of diffuse as well as diffractive reflections from the static rectangular shape [11]. While these features are highly valuable contributions, the target model is limited in two respects. First, due to the complexity of the energy interactions that occur underground, there are signal attenuation effects that must be

accurately accounted for. This is attributed to the system, ground medium, target reflection and target transmission properties unique to each scenario, specifically, as the frequency of the signal varies. Secondly, a more realistic model should allow simulation of different target shapes and sizes. This makes for a more robust system, extending its capabilities beyond rectangular approximations. These and additional upgrades are summarized below:

- Enabling the analysis of any target shape, size, and homogeneous composition (such as an air-filled tunnel or bunker) using CAD Solid Works as a supplemental software tool.
- Detailed observance to Snell's Laws of reflection/ refraction, Fresnel's equations, Helmholtz's Reciprocity Rule, and the Laws of Conservation of Energy.
- Integration of previous software features (ray tracing, BRDF).

The results presented in this thesis implement a discrete set of energy interactions identified as Initial Target Interactions (ITI), Secondary Target Interactions (STI), and Final Target Interactions (FTI). This is an original concept for the analysis of 3D GPR targets and incorporates the modeling techniques of ray-tracing and the BRDF to provide a more accurate target model than the one currently in use.

1.2 Overview

The remainder of this thesis outlines improvements to a ground penetrating synthetic aperture radar target model. These improvements and their reasoning are organized as follows:

Chapter 2: Includes a literary review of ray-tracing and the BRDF.

Chapter 3: Discusses the necessary background theory, practices associated with radar relative to the simulated target model.

Chapter 4: Description of the ground penetrating radar system.

Chapter 5: Description of the ground penetrating radar target model and its modifications.

Chapter 6: Simulated results generated using the GPR target model with analysis.

Chapter 7: Summary, conclusions drawn from the experiments conducted, and proposed future work.

Chapter 2

Review of Literature

To correctly model a realistic GPR system, a slew of parameters and fundamental components must be accounted for. In the case of bistatic GPR, the simulated target, ground properties, the propagated signal, and antennas used for transmitting and receiving each possess their own uniqueness that must be outlined and specified.

Target modeling must account for different sizes, shapes, and compositions. This is due to the various complex energy interactions that can take place when a signal is incident upon its surface. These issues are complicated by the nature of ground medium through which electromagnetic energy is allowed to propagate. Permeability, conductivity, and permittivity each contribute to signal degradation, including attenuation, dispersion, diffraction, and diffusion, and must be modeled accordingly. The signal, itself, also has variable characteristics. Defining amplitude, frequency, and periodicity of signal transmission makes for a multifaceted system component. The final considerations lie in the hardware from which energy is emitted (the transmitter), and detected (the receiver). Directivity and polarization must be accounted for when considering signal transmission, and contribute to this extensive list of GPR system features. To correctly model each of these, the ray-tracing technique and bidirectional reflectance distribution function have been utilized and their implementation improved upon.

2.1 Ray-Tracing Technique

Typically, modeling of the propagation of electromagnetic waves is a complicated feat. The use of the Finite Difference Time Domain technique [1] in GPR target modeling

is undesirable and requires extensive computational power. A more desirable alternative is the use of ray-tracing to approximate electromagnetic waves and the nature of its energy-matter interactions.

The ray-tracing technique may be considered in either of two formats, forward or backwards ray-tracing [16]. In the former, straight lines, or rays, are originated at the transmitter, propagated through the sub-surface scene, and target reflections are collected by the receiver. The latter simulates the opposite, where rays originate at the receiver and are traced from receiver to target to transmitter. The decision of which approach to implement is determined by the size of the transmitter, or source, relative to the receiver. A large source favors backward ray-tracing while a small source favors the forward approach. In the case of a GPR using SAR, the forward ray-tracing technique is preferred due to the large receiver array in comparison to the single transmitting antenna.

2D cases incorporating forward ray-tracing into a GPR model are presented by Cai and McMechan [3] and Goodman [4]. Though their contributions are significant, the scope of each is limited. While Cai and McMechan consider specular reflection and path attenuation of the signal as a function of frequency, only the ground's dielectric permittivity is included as a medium property. Additionally, Goodman's work, through the use of scene segmentation, neglects inclusion of anisotropic target properties. In either case, these 2D models effectively ignore important medium properties as well as diffuse and diffractive elements inherent in the system. The latter of these is addressed in the next section of this chapter.

Glassner incorporates geometric physics to describe 3D ray-target surface interactions [16]. In this method, targets are composed of triangular facets and the normal

vector to each facet serves a primary reference when calculating the angles of reflection and refraction due to incident energy. This facet concept is extended by Jeter and his work in the modeling of rectangular targets [1]. Jeter's integration of ray-tracing into this specific GPR system serves as the backbone of the target construction model used in this research for designing targets of variable sizes and shapes.

Antenna modeling with the ray-tracing technique is accomplished by mimicking the direction and strength of transmitted rays based on the directivity and gain of an antenna's radiation pattern. For isotropic antennas, this is not a concern, but is easily implemented for directive antennas. Additional influences in this approach include selecting the best antenna type relative to the transmitted signal bandwidth. For this CWLFM system, Lestari, Yarovoy, and Ligthart's findings support the use of a capacitively-loaded bow-tie antenna [8]. When investigating the performance characteristics of this antenna type against a dielectric-filled Transverse Electric and Magnetic (TEM) horn, and dielectric embedded shielded dipole, the bow-tie was the most suitable for a wide range of low frequency electromagnetic radiation [11]. The primary antenna type considered for this research is the isotropic bow-tie antenna.

As mentioned earlier, methods to model signal degradation are limitedly addressed by Cai and McMechan. Accounting for these attenuation, dispersion, diffraction, and diffuse reflections during energy-matter interactions becomes inherently complicated in ray-trace modeling. Attempts to approximate these phenomena by Sato, Wakayama, and Takemura highlight the inclusion of supplemental rays to the edges of incident target surfaces [2]. Alternatively, Goodman combines data from scenes with

differing materials to imitate these effects [4]. These previous works have led to the addition of a technique specifically designed to account for this complexity, the BRDF.

2.2 Bidirectional Reflectance Distribution Function (BRDF)

Within the varied list of features describing a GPR system, the nature of electromagnetic wave reflections from a surface are also characterized by a host of properties. As a signal, these include attenuation, diffusion, diffraction, and dispersion in addition to the predicted specular traits. As a means to model these properties, many different computer graphics techniques have been developed. Based on incident electromagnetic energy, one such rendering technique is the BRDF [11, 21-22].

Through influential by work Beckmann in the area of shadowing functions in scattering field algorithms [17, 18], Torrance and Sparrow proposed their own analytical model. This was based on geometric optics through a combination of applied physics and computer graphics. This model effectively accounted for both specular and diffuse reflections of targets defined by tiny, randomly disposed, mirror-like facets [11, 19], but was limited in accuracy. In compliance with the fundamental laws of optics, a more computationally and physically accurate model was developed by Phong [20]. His approach was based on defining a normal vector to the target surface as a frame of reference. This work made way for Cook and Torrance to present a model which related the brightness of an object to the intensity and size of the incident energy which interacts with it [11]. All of these contributions have amalgamated to produce several additional reflectance models, one of which is considered in this research, the BRDF.

In line with the same principles behind bistatic radar, determining the intensity of reflected energy using the BRDF is based on three vantage points: the source location of

incident energy, the target at which the reflection takes place, and the position of an observer viewing the reflection. Specifying incoming and outgoing energy at a given point on a surface is the basis for the BRDF [11]. A customizable BRDF is proposed by Schlick and his work is founded in varying position, incident direction, observed direction, and wavelength to accurately account for specular and diffuse reflections. Kapfer incorporates Schlick's work into this GPR model while modifying one of the parameters that defines the BRDF. This modification includes replacing the way spectral reflections are calculated [11].

This research also incorporates the BRDF into the intricate geometric analysis demanded by the ray-tracing technique as a way to correctly simulate target detection specific to this GPR system.

Chapter 3

Theory

The bare-bones of a radar system demand a transmitter, target, receiver, and a signal to relay information. In this GPR system, a discussion of how these components are used to accomplish the task of detecting a target underground encompasses a wide range of topics. Each topic is founded in the principles of electromagnetism and communications. Furthermore, modeling this target detection requires that a correlation be established between the physical system and the theoretical concepts used to simulate it. These target detection methods and the representations used to model them are described in the following sections.

3.1 Radar and Target Detection

Many liken target detection using radar to the concept a person letting out a loud, brief, yelp and perceiving the echo from a canyon wall. Fundamentally, the transmitter is the person's voice, the target is the canyon wall causing the echo, the receiver is the person's ear, and the signal is the yelping sound. By knowing the speed of sound, the density of the air, and the time between when the signal was instantiated and then audibly detected, an approximation of the canyon's distance from the individual can be calculated. This is analogous to radar with the exception that instead of using sound waves, electromagnetic waves are transmitted, reflected, and received as the relayed signal. Beyond distance, radar also offers information about a target's position (i.e. direction of distance), velocity, and type. For this GPR, only position and type are considered since subsurface targets are not expected to be mobile. This requires an extensively sophisticated system with carefully designed parameters.

3.1.1 System Parameters

The transition in scope from the movement of free electrons to the creation of electromagnetic waves to the formation of electromagnetic fields is well documented by Jeter and Kapfer [1, 11]. Sufficient for this discussion, the reader must understand that electromagnetic waves, in the form of a time-varying signal, are used to carry information about a target. The mathematical representations for the electric and magnetic components which form this signal are shown below.

$$E(z,t) = \mathrm{Re}[\hat{E}(z)e^{j\omega t}]$$
$$H(z,t) = \mathrm{Re}[\hat{H}(z)e^{j\omega t}] \qquad (3\text{-}1)$$

Where $\hat{E}$ ≡ Electric field intensity (phasor)
$\hat{H}$ ≡ Magnetic field intensity (phasor)
t ≡ Time
z ≡ Position
ω ≡ Frequency

In general, the transmitter radiates energy in the form of a signal with predefined characteristics (frequency, amplitude, periodicity, etc). The signal then propagates through a medium until either: 1) all the energy in the signal is dissipated, i.e. lost, in the medium or 2) the signal collides with the intended target, the signal is re-directed, and any remaining energy is collected by the receiver. Once received, it is the properties of these waves (time delay, diffusion, attenuation, dispersion, diffraction) that are translated using various signal processing techniques into an interpretable format.

In the case of the echo analogy, it stands to reason that the more faint the sound of the yelp, the farther the canyon wall is from the person detecting it. Since a key parameter in successful target detection using radar is the strength of the return signal, an important starting point in designing a radar system is determining, *a priori*, what the maximum detectable range of the radar will be. In other words, what is the largest distance away

this system should be capable of target detection. Although there are many variations, one version of the governing radar range equation is found in Equation (3-2).

$$R_{\max} = \left[\frac{P_t G A_e \sigma}{(4\pi)^2 S_{\min}} \right]^{1/4} [m] \qquad (3\text{-}2)$$

Where $R_{\max}$ ≡ Maximum detectable range
P_t ≡ Transmitted power
G ≡ Antenna Gain
A_e ≡ Effective antenna aperture
σ ≡ Radar target cross section
S_{min} ≡ Minimum detectable signal

With the exception of the radar cross section (RCS), selecting suitable values for the remaining variables that make up (3-2) are left to the designer. The versatility inherent in this equation justifies the need for different types of radars to be custom built for different applications.

Selection of appropriate hardware is paramount to successful target detection. The hardware is characterized by antennas and their operational parameters (radiation pattern, radiation efficiency, input impedance, resonant frequency, and bandwidth). The simplest antenna configuration is monostatic radar, consisting of one antenna with the dual responsibility of transmitting and receiving the signal of interest. This idea can be extended to bistatic and multi-static configurations, where there are multiple antennas performing similar functions as it relates to signal transmission and reception. The GPR system considered exhibits the properties of a pseudo-monostatic or bistatic system, requiring two separate antennas (1-transmission, 1-reception). This configuration was chosen due to the nature of the model and its incorporation of SAR signal processing techniques to interpret the radar return data.

Not only is a strong return signal a desired trait of radar return data, but a high resolution image holds significant weight as well. Based on the principles of antenna theory, the larger an antenna used in radar, the greater the obtainable resolution will be in the return data. Radar angular resolution is directly proportional to the physical size of the antennas used during signal transmission and reception [11]. The spatial resolution of a system is segmented into two categories: cross-range and slant range. Slant range is simply the maximum distance away a target can be detected (R_{max}), and is discussed earlier in the chapter. Cross-range resolution designates the minimum detectable distance between two objects within the 3dB beam width of the radar. This is typically calculated in radians because of the curvature associated with the radiation pattern of the antenna used, like an arc outlining part of a circle. If, for example, a radar system from a far off distance can distinguish between two objects separated by 16 radians, this value is said to be the radar's cross-range resolution.

$$\theta_{3\,dB} \approx \frac{0.89\lambda}{D}\,[radians] \qquad (3\text{-}3)$$

Where $\theta_{3\,dB}$ ≡ Cross-range resolution
λ ≡ Wavelength of transmitted signal
D ≡ Physical antenna length

This frequency dependence in the cross-range resolution can complicate the system, requiring different signal processing techniques. One such technique is Synthetic Aperture Radar (SAR).

SAR borrows from the concept of a person looking at an object, such as another human face, from multiple angles as a way to more thoroughly describe that object. In practice, this method considers an iterative process whereby a transmitted signal follows the typical path of propagation (transmitter – target – receiver), the receiver is

repositioned, and the process is repeated. Implementing this concept in radar requires several discrete sets of return data be collected for one particular target location. The consequences include requiring more resources (data collection and signal processing time) to provide this high resolution, however, the decision to implement a SAR system is at the mercy of the designer.

The calculable resolution obtainable in a focused SAR system is directly related to the physical size of the individual receiver antenna used.

$$\Delta X_{SAR} = \frac{D}{2}[m] \qquad (3\text{-}4)$$

Where ΔX_{SAR} ≡ Cross-range resolution
D ≡ Physical antenna length

As (3-4) suggests, the resolution is proportional to the physical aperture of the antenna. No longer is the resolution dependent on the frequency of the transmitted signal and the reduction of the antenna's length actually improves the system resolution. This is counter-intuitive based on the established rules for non-SAR systems.

By accounting for these multiple signal transmissions and receptions, a much desired high resolution image can be obtained in both 2D and 3D for a given target. For this research, SAR techniques were implemented and headline the key features of this GPR system. The next challenge in target modeling is accurately describing the environment in which GPR operates. The ground medium and its contribution to target modeling is the next most pertinent concern.

3.2 Propagation and Medium

One major concern specific to GPR is the consideration of ground properties through which a signal is expected to propagate. In reality, the earth is a heterogeneous combination of layered soil compositions, though simulations are often limited to

homogeneous ground compositions. Sand, rock, gravel, etc. can each be described by their electrical properties and how a signal, given its electromagnetic components, will behave when propagating through these materials. The three ground properties of interest are dielectric permittivity, conductivity, and permeability.

The dielectric permittivity (also known as the relative permittivity, ε_r) of a material is defined as the degree to which a medium resists the flow of electric charge. It is the ratio of the electric displacement to the electric field strength [13] and relates the permittivity of that material to the permittivity of free space [24] as the absolute permittivity.

$$\varepsilon = \varepsilon_r \varepsilon_o \quad [F/m] \qquad (3\text{-}5)$$

Where ε ≡ Absolute permittivity
ε_r ≡ Relative permittivity of a material
ε_o ≡ Permittivity of free space (8.854×10^{-12} [F/m])

The next ground property is electrical conductivity (σ). This parameter provides a quantitative measurement of how "well" a material allows an electromagnetic wave to propagate through it. Often associated as the inverse of resistance because of its units of measurement (Siemens per meter, *S/m*, or [Mhos/m]), the conductivity of a soil composition is a function of its volume, density, electrolytes in ground water and the conductivity of the mineral phase [11, 26]. Mathematically, conductivity is related by the ratio of current density to the electric field through the material.

$$\sigma = \frac{J}{E} \quad [S/m] \qquad (3\text{-}6)$$

Where σ ≡ Conductivity
J ≡ Current density in a surface
E ≡ Electric field through a surface

The final property considered in a GPR medium is its relative permeability (μ_r). In contrast to relative permittivity and its relationship between a material and the electric field strength, this ground characteristic is a quantitative measurement of the interactions between the medium and the magnetic field strength. Like absolute permittivity, this measurement requires a reference, thus absolute permeability relates a material's relative permeability to that of free space.

$$\mu = \mu_r \mu_o \quad [rad/m] \qquad (3\text{-}7)$$

Where μ ≡ Conductivity
μ_r ≡ Relative permeability of a material
μ_o ≡ Permeability of free space
(4π x 10^{-7} [H/m])

These are the intricacies which describe the medium in which a GPR signal propagates. Once outlined, the nature of the physical interactions that take place between the signal, the medium, and the intended target can be specified. This furthers the understanding of GPR and the need for an accurate target model.

The details associated with the transfer and movement of electromagnetic energy through air proliferate when the medium of propagation changes. Due to the many directional components and varying intensities of energy inherent in reflections of anisotropic surfaces, changes in the associated signal must be accounted for. Even soil compositions with a low dielectric permittivity can significantly distort the integrity of a signal as it reflects from a target beneath the surface of the earth. Fortunately, these distortions can be accounted for and constitute the next major contribution to this target model. The laws of reflection, refraction, and conservation of energy contribute to this description of propagating energy underground and are described in the next section.

3.3 Energy Interactions

Radar relies heavily on the concept of energy interacting with matter. Without these interactions, it would be very difficult to detect the presence of a target. Along side radar, computer graphics is another industry which contributes to the understanding of energy-matter interactions in the context of light striking different surfaces [11]. For our purposes, we retain the idea of electromagnetic energy transferred from one source or location to another.

3.3.1 Reflection & Transmission: Types and Principles

When energy is reflected from a surface, there are two types of reflections that can take place: specular and diffuse. The latter will be discussed later in this section. According to Snell's Law, specular reflection is defined as a reflected ray which resides in the plane of incidence and has an angle of reflection equal to the angle of incidence [11, 28].

$$\theta_i = \theta_r \quad [rad] \tag{3-8}$$

Where θ_i ≡ Angle of incidence
θ_r ≡ Angle of reflection

Consider two people of the same height, standing a distance of Y meters apart. The Law of Reflection (also known as the Law of Reflection) states that if one person bounces a ball forward at an angle, J, such that the ball strikes the ground midway (Y/2) between the two people, the second person would receive the ball at that same angle, J. This concept is important because the sum of the directional vectors made by the path of the ball is a plane, so the result is the same in two and three dimensions.

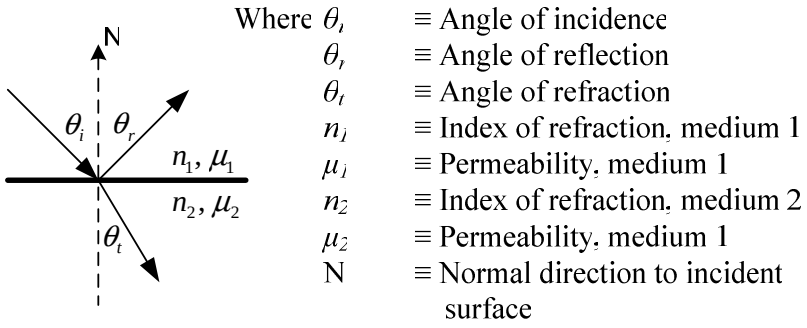

Figure 3.1 2D Energy Reflection/ Refraction model

Since energy is a physical quantity, not necessarily limited in direction, it can disperse as it passes between surfaces; therefore specular reflections are not the only type of reflection a ray experiences when incident upon a surface. While a majority of incident energy may be reflected in a specular direction, an observer from a different angle is likely to view diffuse reflections resultant from that same incident ray. Diffuse reflections account for the rays reflected in all remaining directions other than specular.

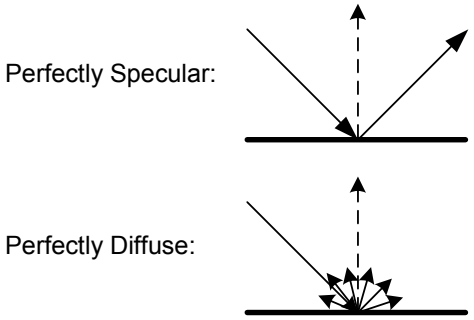

Figure 3.2 Comparison between specular and diffuse reflections

The presence of diffuse reflections obeys the Law of Conservation of Energy which requires that all energy entering a system equals all energy leaving that system. This is validated by the idea that if a quantifiable amount of energy is incident upon a totally reflective surface and the amount of energy received in the specular direction does not equal the incident amount of energy, the difference must be accounted for in energy reflected in directions other than specular. To calculate this quantifiable amount of energy, Fresnel's Equations are used.

These equations provide a mathematical representation relating the reflected and transmitted electric field amplitude to that which is incident on a dielectric. This demonstrates the transfer of energy between two materials of differing dielectric compositions.

$$r_{||} = \frac{E_r}{E_i} = \frac{\frac{n_2}{\mu_2}\cos\theta_i - \frac{n_1}{\mu_1}\cos\theta_r}{\frac{n_1}{\mu_1}\cos\theta_r + \frac{n_2}{\mu_2}\cos\theta_i}$$

$$r_{\perp} = \frac{E_r}{E_i} = \frac{\frac{n_1}{\mu_1}\cos\theta_i - \frac{n_2}{\mu_2}\cos\theta_r}{\frac{n_1}{\mu_1}\cos\theta_i + \frac{n_2}{\mu_2}\cos\theta_r}$$

Where $r_{||}$ ≡ Parallel reflection amplitude
$r_{\perp}$ ≡ Perpendicular reflection amplitude
E_r ≡ Reflected electric field intensity
E_i ≡ Incident electric field intensity
θ_i ≡ Angle of incidence
θ_r ≡ Angle of reflection
θ_t ≡ Angle of refraction
n_1 ≡ Index of refraction, medium 1
μ_1 ≡ Permeability, medium 1
n_2 ≡ Index of refraction, medium 2
μ_2 ≡ Permeability, medium 1

Figure 3.3 Fresnel's Equations

Fresnel's equations include both perpendicular and parallel amplitude components and are found in Figure 3.3. Since power quantities are easier to use than amplitude in the case of GPR systems, the squared magnitudes of these components are expressed in Equation 3.9, as stated by Kapfer [11].

$$R_{||} = \left|r_{||}\right|^2 \qquad (3\text{-}9)$$
$$R_{\perp} = \left|r_{\perp}\right|^2$$

Where $R_{||}$ ≡ Parallel reflection power
$R_{\perp}$ ≡ Perpendicular reflection power
$r_{||}$ ≡ Parallel reflection amplitude
$r_{\perp}$ ≡ Perpendicular reflection amplitude

The variables that contribute to this energy dynamic are the dielectric permeability, angles of incidence and refraction, and index of refraction, which will be discussed in the next section. The remaining topic of interest is the angle of refraction.

The transmission of energy through a surface is governed by the Law of Refraction (also known as Snell's Law). This law states that a refracted ray lies in the

plane of incidence and has an angle of refraction that is related to the angle of incidence, and the wavelength of the incident and refracted ray [11, 28]. This completes a qualitative definition for the Law of Conservation of Energy, shown in (3-10).

$$\Sigma\ Total\ Energy = \Sigma\ Transmitted\ Energy + \Sigma\ Reflected\ Energy + \Sigma\ Attenuated\ Energy \quad (3\text{-}10)$$

Once all quantities can be accounted for in energy-matter interactions (incidence, transmission, and reflection), a closer look into the kinematics behind the behavior of this energy and its varying characteristics in the form of a ray is warranted.

3.3.2 Properties

In GPR work, the change from one dielectric boundary to another is of primary importance for energy interactions. When modeled as a wave, propagating energy is guaranteed to suffer fluctuations in velocity and wavelength. As a ray, aberrations include abrupt shifts in angles of reflection and transmission, and a reduction in intensity (or power). Here, the geometric physics and the variables that control these properties are outlined.

The velocity of an electromagnetic wave propagating through a particular medium is relative to that same wave traveling at the speed of light in a vacuum. This velocity can be expressed as the ratio of c, the speed of light ($\approx 3 \times 10^8$ m/s), to the index of refraction of the medium which the energy, or ray, passes through. This index of refraction, *n*, is an empirically defined value. By exchanging the two quantities, *v* and *n*, in the definition of wave velocity, the index of refraction of a medium can be calculated experimentally.

$$v = \frac{c}{n}[m/s] \qquad (3\text{-}11)$$

Where v ≡ Wave velocity through a medium
c ≡ Speed of light in a vacuum
n ≡ Index of refraction of medium

Another unstable property caused by changing dielectric boundaries is the wavelength of a wave. This is a measurable distance between two successive peaks of the signal.

$$\lambda_n = \frac{\lambda}{n}[m] \qquad (3\text{-}12)$$

Where λ_n ≡ Wavelength in a medium
λ ≡ Wavelength in free space
n ≡ Index of refraction of medium

The change in wavelength reflects the change in the velocity of a wave as it travels from one medium to another. This emphasizes the importance of a medium's dielectric permittivity and permeability characteristics as discussed in Section 3.2.

The angle of incidence and the angle of transmission are heavily influenced by this index of refraction. Used to describe the change between these angles, a mathematical relationship for Snell's Law is expressed in (3-13).

$$n_1 \sin\theta_i = n_2 \sin\theta_t \qquad (3\text{-}13)$$

Where n_1 ≡ Index of refraction of medium 1
θ_i ≡ Angle of incidence
n_2 ≡ Index of refraction of medium 2
θ_t ≡ Angle of refraction

As one experimentally changes the angle of incidence, while holding the indices of refraction of both mediums constant, the variation in the angle of transmission is evident. Further testing of this relationship reveals that beyond a certain angle of incidence, Snell's Law is no longer valid. This angle is referred to as the critical angle. The stipulation exists such that any ray incident to a surface with an angle greater than the critical angle, measured relative to the normal of the surface, will exhibit total internal

reflection. Hence, there will be no transmission of energy through a surface, and all energy will be reflected, as illustrated in Figure 3.4 and Equation (3-14). This is taken into account in the GPR work for this research.

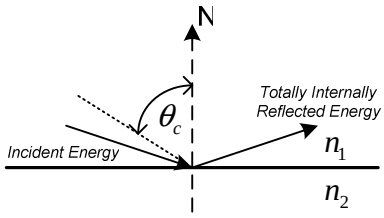

Where θ_c ≡ Critical angle
n_1 ≡ Index of refraction, medium 1
n_2 ≡ Index of refraction, medium 2
N ≡ Normal direction to incident surface

Figure 3.4 Critical Angle and Total Internal Reflection

$$\theta_c = \sin^{-1}\left(\frac{n_2}{n_1}\right) \qquad (3\text{-}14)$$

Where θ_c ≡ Critical angle
n_1 ≡ Index of refraction of medium 1
n_2 ≡ Index of refraction of medium 2

The final characteristic for discussion is the decrease in strength or attenuation of a ray during its propagation through a GPR scene. The degree of a signal's attenuation can vary depending on the initial transmitted power, dielectric properties of the medium, the distance traveled through the medium, and the frequency of the signal. Path attenuation is a critical factor in GPR calculations because of the signal processing required to interpret the return signal. Strong returns with abundant energy reflections indicate one type of target scenario while weak and scattered energy returns make for ambiguous results.

As mentioned, the attenuation a signal experiences is a function several properties. When considering an electromagnetic wave propagating in a lossy medium in three dimensions, the general wave equation is expressed in (3-15) for a positively traveling wave in the z-direction.

$$E(z) = \hat{a}_x(E_0^+ e^{\gamma z}) = \hat{a}_x(E_0^+ e^{-(\alpha + j\beta)z}) \quad (3\text{-}15)$$

Where
- E_0^+ ≡ Electric field intensity
- $\hat{a}_x$ ≡ Unit vector (x-direction)
- γ ≡ Propagation constant
- α ≡ Attenuation constant
- β ≡ Phase constant
- z ≡ Propagation depth

Defined as the exponent in the wave equation, the propagation constant is explicitly defined in (3-16).

$$\gamma = \alpha + j\beta = \pm\sqrt{j\omega\mu(\sigma + j\omega\varepsilon)} \quad (3\text{-}16)$$

Where
- γ ≡ Propagation constant
- α ≡ Attenuation constant
- β ≡ Phase constant
- ε ≡ Absolute permittivity
- σ ≡ Conductivity
- μ ≡ Absolute permeability
- ω ≡ Angular frequency

Derivations of these expressions can be found in [1, 13]. From here, the attenuation and phase constants can be extracted. More specifically, the attenuation term, $e^{-\alpha z}$, represents the direct affect of path distance on signal degradation. Explicitly, the attenuation and phase constants are represented in (3-17).

$$\alpha = \omega\sqrt{\mu\varepsilon}\left\{\frac{1}{2}\left[\sqrt{1+\left(\frac{\sigma}{\omega\varepsilon}\right)^2} - 1\right]\right\}^{\frac{1}{2}} \ [Np/m]$$

$$\beta = \omega\sqrt{\mu\varepsilon}\left\{\frac{1}{2}\left[\sqrt{1+\left(\frac{\sigma}{\omega\varepsilon}\right)^2} + 1\right]\right\}^{\frac{1}{2}} \ [rad/m] \quad (3\text{-}17)$$

Also taken from the work of Kapfer, the following five conclusions have been made based on previous studies relating the variables influencing path attenuation:

1. The underground propagation depths of EM waves are directly related to signal and ground parameters in a GPR environment.
2. The ground parameters that affect the propagation depth of the transmitted signal the most are the conductivity and permittivity of the ground.

3. A dry sandy environment proves to be the best propagating medium according to its conductivity and permittivity characteristics.
4. The signal parameter that affects the propagation depth the most is the transmit frequency. Depending upon the transmit frequency of the GPR system, great depths can be achieved through lower frequencies.
5. The parameter which least affects the propagation depth of the electromagnetic wave in a medium was the permeability of the ground. [11]

In addition to the complex interactions outlined here, a theoretical model which best represents a comprehensive energy interaction is the bidirectional reflectance distribution function. This is used as the backbone tool in calculating all energy-target sub-surface interactions that take place in this GPR model and is discussed in the next section.

3.3.3 BRDF

When a source of energy is made to reflect from a surface, the amount of energy received, or observed, varies as a function of the observer's position. The BRDF provides an approximation of this return energy and is a function of the incident power and that which is observed. This is expressed as a ratio in (3-17).

$$BRDF = \frac{Observed\ Reflected\ Power}{Incident\ Power} \tag{3-17}$$

Both empirical and theoretical BRDF models are available for use; however, empirical models are computationally expensive and are not realistic for real-time systems [11]. Kapfer summarizes the development of theoretical BRDF models and their foundation in geometric optics. According to his findings, theoretical and empirical data match so closely that the use of these analytical models is a legitimate alternative.

The BRDF makes use of several view points relative to two specific directions: the angle of incidence and the angle of observance. From these two angles, combined with the normal vector of the reflecting surface, the spherical coordinates system is divided as illustrated in Figure 3.5.

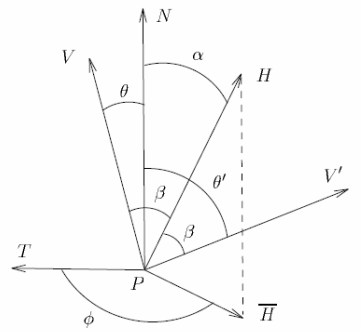

Where N ≡ Microfacet surface normal unit vector
V ≡ Observed energy direction unit vector
V' ≡ Incident energy direction unit vector
T ≡ Projection unit vector of observed direction vector on microfacet surface
H ≡ Bisector unit vector between observed direction vector and incident energy direction vector
$\overline{H}$ ≡ Projection unit vector of bistatic vector on microfacet surface

Figure 3.5 BRDF Geometry[1]

Each angle in the BRDF coordinate system is a variable in the calculation of the BRDF that will be defined now but not referenced until Chapter 5:

$t \equiv \cos \alpha$
$u \equiv \cos \beta$
$v \equiv \cos \theta$
$v' \equiv \cos \theta'$
$w \equiv \cos \varphi$

This reflectance model is preferable for several reasons. Its ability to model isotropic and anisotropic surfaces is of primary importance. An anisotropic surface can be described as one whose reflective properties vary as a function of incident angle, much like a diamond reflecting light at varying angles. Since a majority of realistic target scenarios will not be perfect in their geometry, it is helpful to have a model which can account for physical anomalies in target shape. In simulation, an isotropy factor contributes to the BRDF calculation by indicating the percentage of reflections which should be counted as isotropic in nature.

The next benefit to the BRDF is its ability to model heterogeneous surfaces, i.e. a change from one dielectric to another. Again, since this work revolves around energy propagating between mediums of varying dielectric properties, an analytical

[1] Image: Schlick, "A Survey of Shading and Reflectance Models", Computer Graphics Forum, v13, n2, p. 121-132, June 1994

representation which accurately portrays this type of scene is beneficial. The inclusion of different indices of refraction is embedded within the final expression for the BRDF.

The third component to the BRDF is its flexibility in modeling varying directions. Not only will certain energy reflections be diffuse in nature, but the direction of these diffuse reflections will not be uniform. This introduces the need to simulate three dimensional diffuse reflections in varying directions and is accomplished using a spectral (roughness) factor to indicate what percentage of the reflections from the target will be specular. From this, the remaining reflections are categorized as diffuse. Figure 3.6 gives a complete pictorial explanation of the energy interaction at the surface of a target by including this directional contribution.

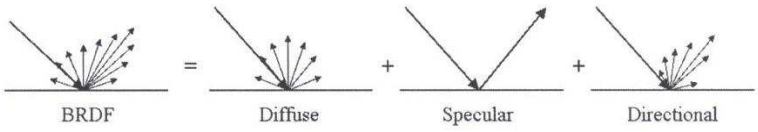

Figure 3.6 BRDF energy contributions: Diffuse + Specular + Directional

Kapfer replaced one component in Schlick's customizable BRDF with his own tested approximation. This adjustment included replacing the spectral factor used to calculate the BRDF with a Fresnel Equation approximation. Kapfer uses the averages of parallel and perpendicular polarization power terms to replace a wavelength dependent constant from Schlick's work. His experiment to test the limits of his approximation can be found in [11].

From these various contributors, the BRDF is represented by (3-18).

$$BRDF = S_{\lambda}(R_{||}, R_{\perp}) * D(t, v, v', w) \qquad (3\text{-}18)$$

Where S_{λ} ≡ Spectral factor
$R_{||}$ ≡ Parallel polarization power term
$R\perp$ ≡ Perpendicular polarization power term
D ≡ Directional factor
t ≡ cos α
v ≡ cos θ
v' ≡ cos θ'
w ≡ cos φ

The dynamic properties of the BRDF have allowed the incorporation of its energy interaction modeling features with ray-tracing to provide an all-inclusive realistic GPR target model.

Chapter 4

Description of System

Beyond the fundamentals of traditional radar, the implementation of a GPR requires a thorough list of specifications. Features describing the hardware and configurations, transmission signal, and the environment (i.e. ground medium characteristics) provide identity to the system. Additionally, advanced signal processing techniques to eliminate ambiguous return data are required for image generation based on the return energy collected from multiple receiver locations. Whether this return energy is realistic (collected during field testing) or simulated (as generated in this work), the building blocks remain the same. These include the GPR system, the pre-image processor, and the SAR image processor.

4.1 Ground Penetrating Radar (GPR) System

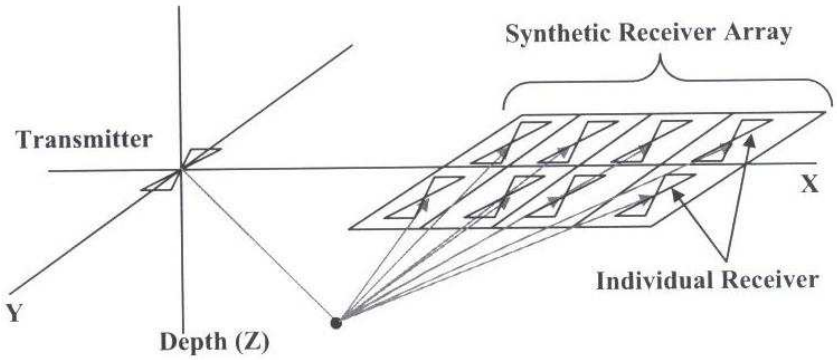

Figure 4.1 GPR physical set-up[2]

Both in practice and in modeling, the GPR system considered in this work is represented as a bistatic synthetic aperture radar system transmitting a CWLFM signal. The bistatic feature indicates the use of two bow-tie antennas, the first of which is dedicated to signal transmission. The other, used for reception, is placed in multiple locations during testing to form a grid configuration, effectively creating a larger

[2] Courtesy of Jeter thesis [1]

synthetic receiver. As discussed in Chapter 3, this matrix of receiver locations provides a larger effective antenna aperture and allows reflected energy returns to be received from many angles due to its varying positions.

The specific energy signal transmitted is the CWLFM sinusoid or "chirp" signal. Generated at the transmitter, the chirp linearly decreases in frequency over time and is repeated to create a continuous signal.

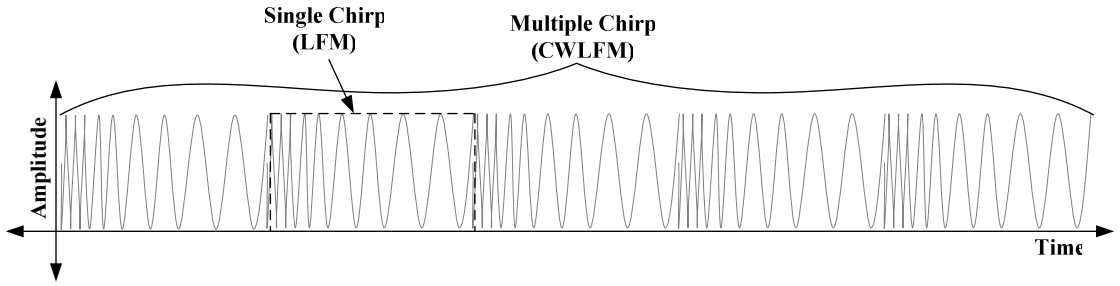

Figure 4.2 Continuous Wave Linear Frequency Modulated "Chirp" Signal[3]

As a wideband signal, its frequency range for GPR applications typically falls between 3-66 MHz with a 1-2 ms transmit period [11]. The benefit of using this signal type is in the increased amount of information available in the return. The lower frequencies of a chirp signal experience less attenuation at deep ground levels of propagation while the higher frequencies provide improved resolution at shallower depths. For the purposes of this work, a frequency band of 1 – 10 MHz will be considered to demonstrate the effects of depth on signal return as a function of frequency and is discussed in Chapter 6. This signal type can be represented mathematically as shown in (4-1).

[3] Courtesy of Kapfer thesis [11]

$$s(t) = a(t)\cos(2\pi f_{start} t + \pi\gamma t^2) \qquad (4\text{-}1)$$

Where $s(t)$ ≡ Transmitted LFM signal
$a(t)$ ≡ Transmit Amplitude
f_{start} ≡ Start frequency
t ≡ Time
γ ≡ Chirp rate

The "linear" property of the signal is expressed in the argument of the cosine term. This allows a simpler interpretation, graphically, such that the chirp signal is best represented on a Frequency v. Time axis in Figure 4.3.

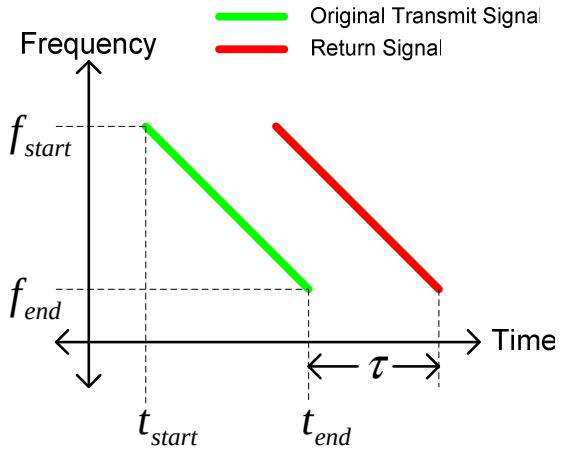

Figure 4.3 Chirp Transmit/Return Signal

To determine a target's range, the time difference, τ, is calculated between transmission and reception of this frequency-varying signal. Using the original transmit signal as a reference, the return signal will indicate the approximate distance between the transmitter and an intended target. The specifics behind signal reception include mixing and low-pass filtering. This process is known as "de-chirping" the signal.

The nature of a chirp signal delayed in time provides both amplitude and phase information about a target. A large amplitude in the return indicates that an electrically large target is reflecting a significant percentage of the original transmit energy. A delay in time, τ, corresponds to a change in frequency. This change in frequency, in turn,

corresponds to a particular phase delay and consequently, a target's distance from the system. These two pieces of information are acquired independently.

The amplitude is calculated as a function of path distance using our ray-tracing technique and BRDF model discussed earlier. As the propagation of the signal through a homogeneous medium (not air) experiences increases in path distance, attenuation will reduce the signal's amplitude.

In simulation, phase information is collected by determining the direct line-of-sight distance between transmitter-target and target-receiver. These scalar values are summed and divided by the velocity of the propagating signal through the scene. Detailed in (4-2), this relationship provides the time difference between transmission and reception and contributes to an important ratio.

$$\Delta t = \frac{D_{Total}}{v} = \frac{R_1 + R_2}{(c/n)} \qquad (4\text{-}2)$$

Where
- Δt ≡ Transmitted signal time delay
- D_{Total} ≡ Total distance traveled
- R_1 ≡ Distance from transmitter to target
- R_2 ≡ Distance from target to receiver
- v ≡ Signal velocity
- c ≡ Speed of light (8.854×10^{-12} [F/m])
- n ≡ Index of refraction of medium

The hardware approach to obtaining phase information is through the use of a mixer and low-pass filter. By mixing the return chirp with its reference signal, the result is a time-varying signal with a low fundamental frequency and supplemental higher harmonics. After low-pass filtering the higher harmonics, the remaining fundamental frequency represents a phase shift. The inverse of this phase shift provides the time difference between the return and its reference. The hardware block diagram of these signal conditioning techniques is shown in Figure 4.4.

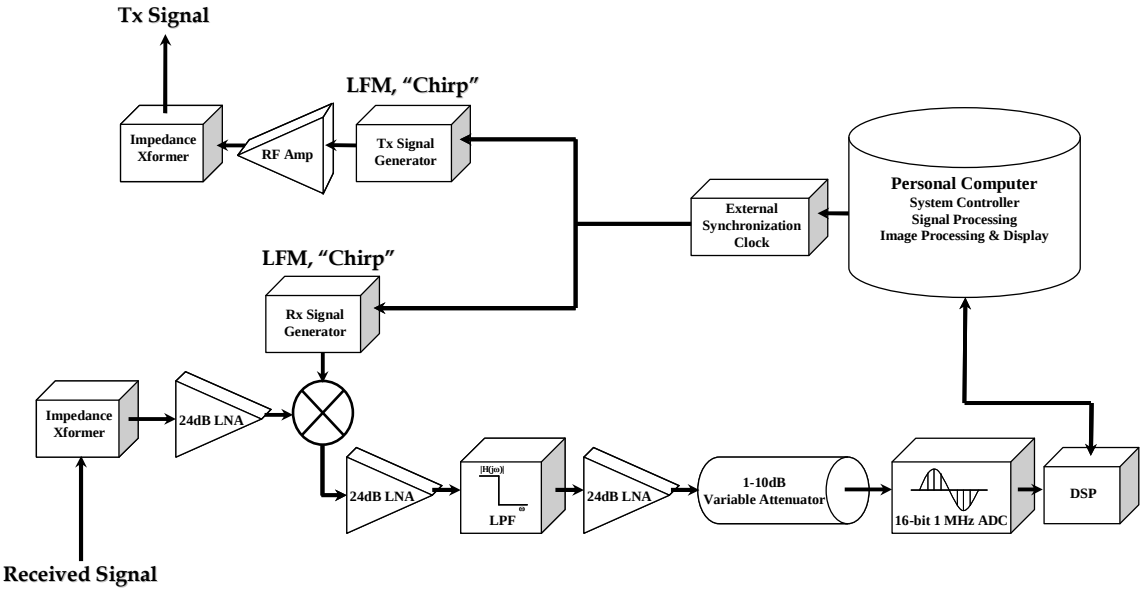

Figure 4.4 Complete GPR System *(Image reproduced from AFRL)*

Beyond the transmitter, receivers, and antennas, an external clock is required to correctly synchronize the mixing of the two signals. The low-pass filtering can be accomplished using discrete components (resistors and capacitors), and any microprocessor with a specified resolution acts as suitable analog-to-digital converter. The final two blocks included (pre-image processor and SAR processor) are discussed in section 4.2. Whether in simulation or hardware, the individual de-chirped return can be represented as shown in (4-3).

$$r(t) = a(t)\cos(2\pi f_{start}(t-\tau) + \pi\gamma(t-\tau)^2) \qquad (4\text{-}3)$$

Where $r(t)$ ≡ Returned LFM signal
$a(t)$ ≡ Received amplitude
f_{start} ≡ Start frequency
t ≡ Time
τ ≡ Delay
γ ≡ Chirp rate

Accounting for each receiver, the total return from a target is expressed as a summation of this signal and can be condensed into the form of (4-4).

$$\sum_{n=1}^{N} a(t) * \mathrm{Re}\left[e^{-j\theta_{m,n}}\right] \qquad (4\text{-}4)$$

Where $a(t)$ ≡ Received amplitude
$\theta_{m,n}$ ≡ Phase shift
N ≡ Number of interactions
m ≡ Receiver location
n ≡ Target location

The signals received in each grid position require extensive magnitude manipulation, phase alignment and corrective processing techniques. This is accomplished during the pre-image and SAR processing stages.

4.2 Pre-Image Processing

In addition to pre-conditioning that the return signal experiences in a GPR system (mixing, low-pass filtering), there are several layers of corrective signal processing required. These processing stages were developed by the Air Force Research Laboratory (Rome Research Site) and a local subcontracting software development company in Utica, NY. In order for the SAR processor to correctly translate the return signal with a 3D image, a series of normalization, filtering, and other popular techniques are imposed on this data. The block diagram in Figure 4.5 summarizes these various steps.

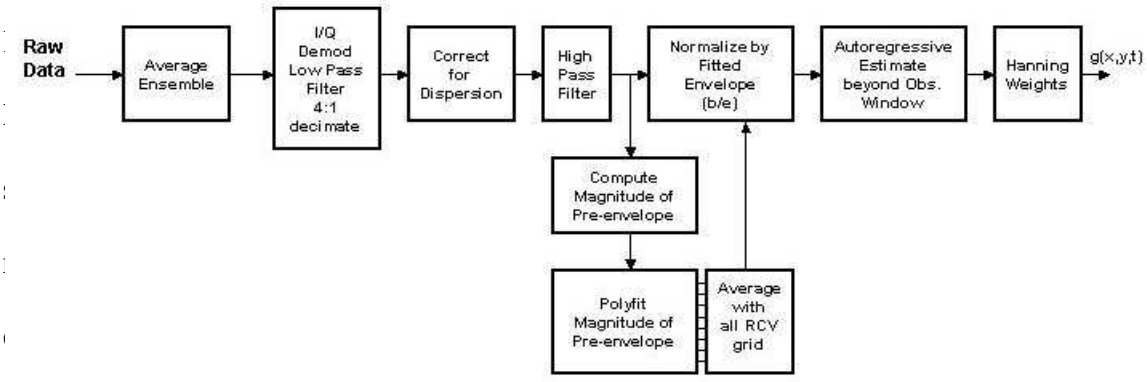

Figure 4.5 Pre-Image Processing Block Diagram[4]

[4] Courtesy of AFRL

Through a combination of coherent averaging and transmission methods to cancel static frequency interference [29], the received signal without noise is shown in Figure 4.6.

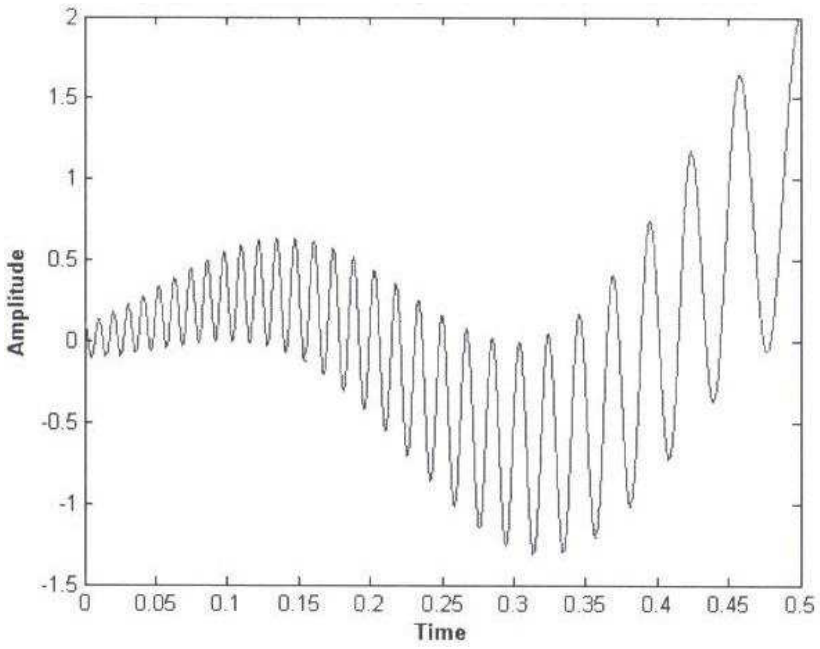

Figure 4.6 Received waveform *(Image reproduced from [11] with authors permission)*

The signal is then subject to in-phase and quadrature-phase (I-Q) demodulation in order to extract phase information from the signal using a Hilbert Transform. A closed form solution is represented by (4-5).

$$H[x] = \sum_{m=-\infty}^{\infty} x(m)W(n-m) \qquad (4\text{-}5)$$

Where $H[x]$ ≡ Discrete Hilbert Transform
$x(m)$ ≡ Discrete data

$$W(k) \equiv \begin{cases} \dfrac{1}{\pi k} & k \neq 0 \\ 0 & k = 0 \end{cases}$$

As discussed in Chapter 3, the ground medium through which the signal propagates typically causes dispersion. This signal corruption leaves undesirable variations in the velocities and wavelengths associated with the signal. This masks any relevant phase information worth extracting. An experimental dispersion compensation algorithm was

introduced to the pre-image processing phase and leverages upon the incorporation of a nonlinear phase component to the received signal [11, 29-30].

For this GPR system, direct path must also be accounted for. Direct path is experienced when a signal bypasses the intended path of propagation towards the sub-surface target and propagates directly from transmitter to receiver. Much like a current in a circuit choosing the path of least resistance, electromagnetic energy tends to behave in a similar fashion by propagating through air, instead of the intended ground medium, with greater velocity. As a result of this deviating path, a noticeably brief delay, as compared to signals traveling through the ground, exists between signal transmission and reception producing an identifiable set of low frequencies. This signal anomaly can be removed through the use of a high pass filter. Corrective measurements to limit direct path include alignment between transmit and receive antennas however the inclusion of the high-pass filter stage in the pre-image processing still proves beneficial.

Aside from frequency-based properties in the return signal, the attenuation experienced as a result of the highly lossy ground medium and depth of propagation requires considerable attention. As mentioned earlier, the multiple frequency signal components that contribute to the chirp signal are attenuated differently dependent on their value. High frequency components tend to experience greater attenuation at lower depths while the opposite is true for components at lower frequencies. This is best understood mathematically in (3-16) and (3-17), highlighting the attenuation constant, α. This constant is defined as a function of frequency, thus any increase in frequency results in a corresponding increase in the attenuation constant. Combined with a lengthy path of propagation, the problem of amplitude reduction is exacerbated. To compensate for these

drastic variations in amplitude values, the inverse of the determined envelope of the received signal is obtained and the data is fitted to this envelop for normalizing purposes. Both the inverse of this envelop and the resultant fitted waveform are shown in Figure 4.7 and 4.8, respectively.

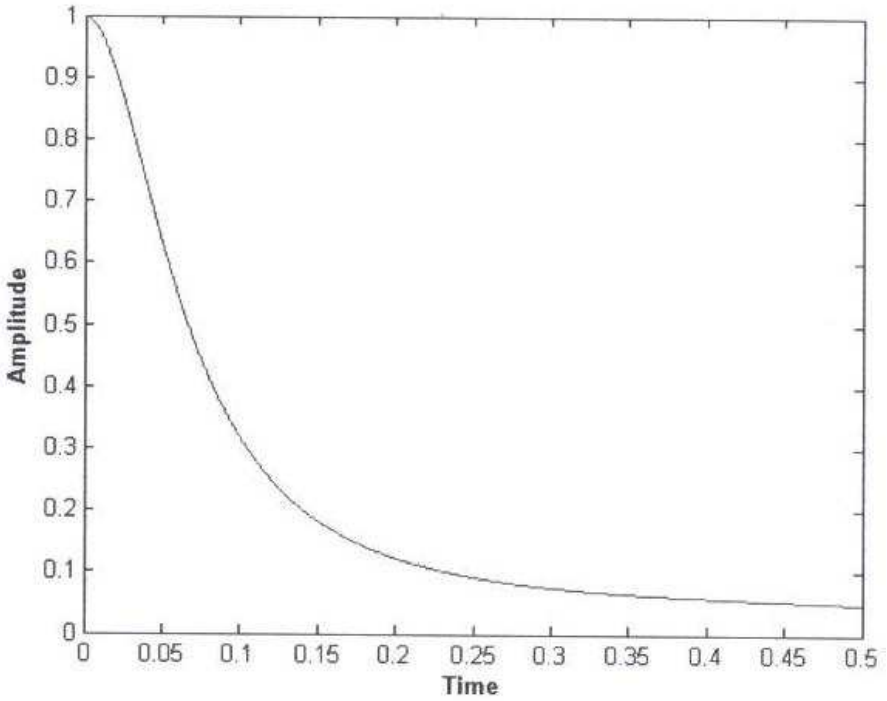

Figure 4.7 Inverse of detected envelope *(Image reproduced from [11] with authors permission)*

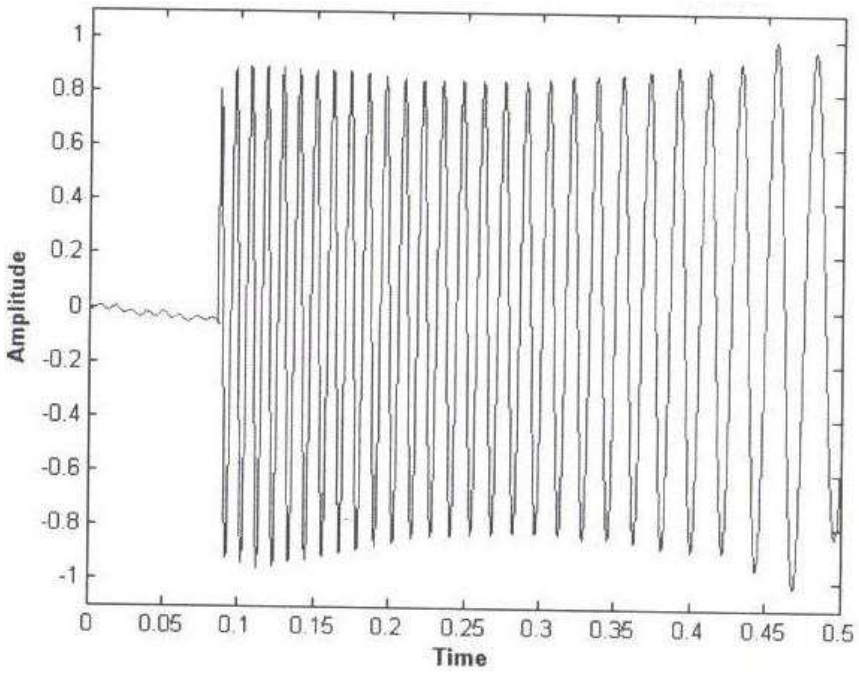

Figure 4.8 Envelop Fitted Normalized Received Waveform *(Image reproduced from [11] with authors permission)*

An irregularity commonly associated with input data to the pre-image processor is the presence of undesired information in the form of sidelobes. This is found during frequency domain analysis of the averaged received signal. As a finite pulse width signal, these detected sidelobe levels are dampened using Hanning weighting techniques and resolution is improved. An example weighting window is shown in Figure 4.9.

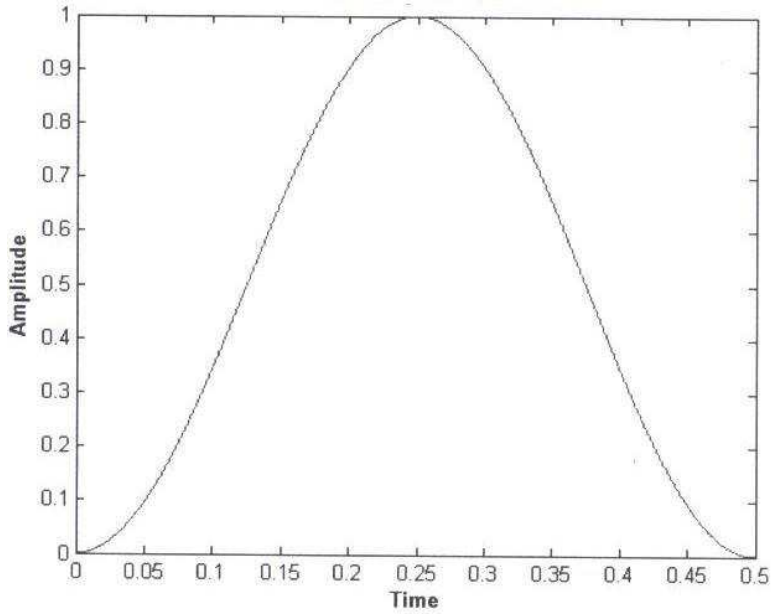

Figure 4.9 Hanning weighting envelope *(Image reproduced from [11] with authors permission)*

This resolution is not achieved at the cost of losing valuable information at the beginning and end of the received signal [11]. To counteract this loss, the Burg Parametric Spectral Estimation Method is implemented to recover this information [29, 30] through interpolation techniques. To guarantee that strong returns recovered at the beginning and end of the signal are sustained, weighting is performed last in the pre-image process.

Whether experimental or simulated data, these techniques are valid for a range of GPR applications and are not unique to this work only. The specifics behind the GPR system, its components and properties produce data which can be easily integrated as input to this processing stage.

4.3 Synthetic Aperture Radar Processing Technique

At the conclusion of pre-conditioning and pre-processing follows the SAR imaging processing method. This stage produces a 3D set of data points containing varying magnitudes and location designators that accurately describe the detected energy

return in the simulated GPR scene. Based on frequency and amplitude characteristics of input data, steps to accomplish this include scene dissections and resolving a multi-dimensional elliptical ambiguity associated with the SAR methodology. The entire block-diagram associated with the SAR processor can be found in Figure 4.10. This includes a host of functional blocks that amount to phase alignment of the pre-processed return data, honing in on how much energy was reflected in the simulated scene, and assigning pixel intensity values in the correct location to accurately describe the target.

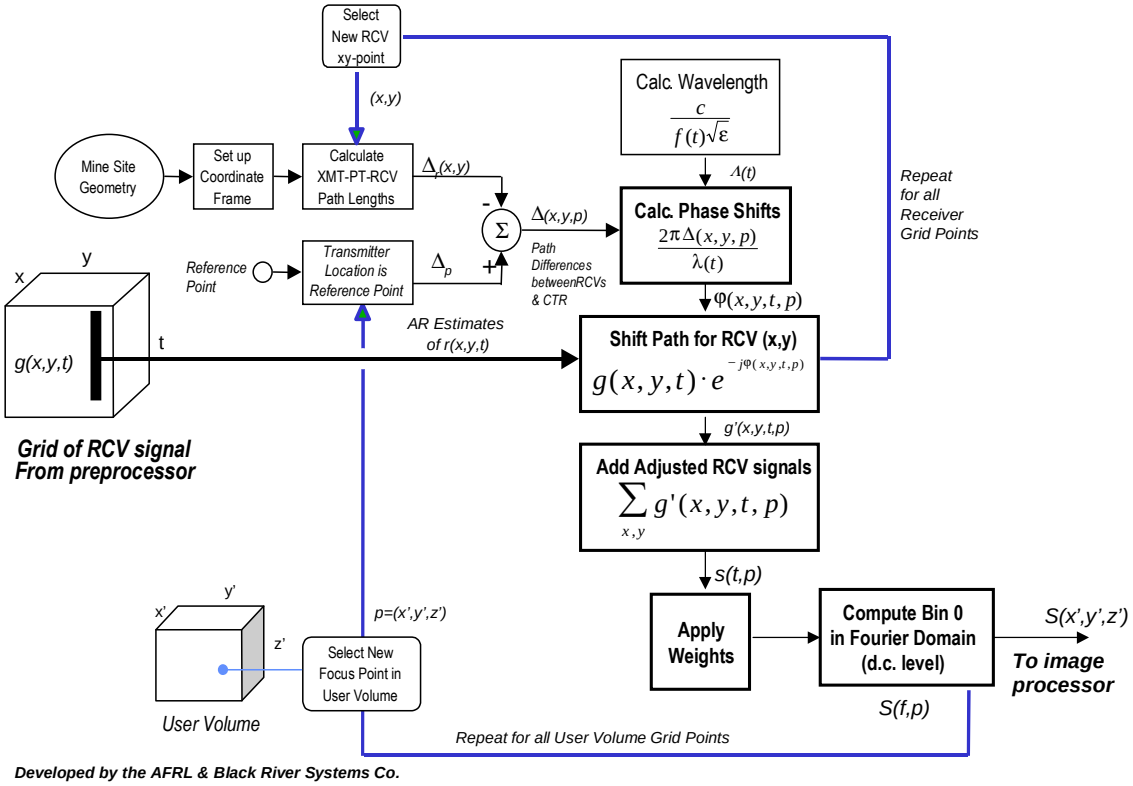

Figure 4.10 SAR image processing block diagram *(Image reproduced from [1] with authors permission)*

Prior to data manipulation and interpretation, the GPR scene of interest is divided into voxels. The same way pixels detail the features in a two-dimensional image, these voxels are likened to 3D pixels and serve as a measure of resolution when imaging the

underground target. An example of how the GPR scene is segmented is shown in Figure 4.11.

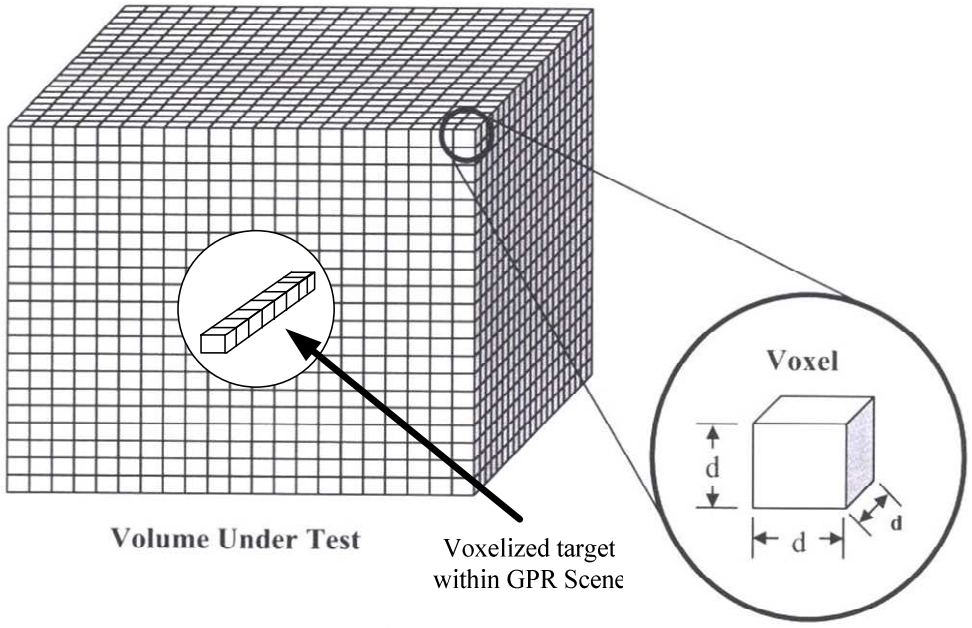

Figure 4.11 Voxels representation *(Image reproduced from [11] with authors permission)*

This resolution is user-defined in the software and presents direct trade-offs between speed and target truth when running the algorithm. The better the specified resolution, the greater latency experienced in producing results.

Incorporating return data to form a SAR image begins pictorially with an understanding of Euclidean distance relative to a given transmitter, receiver, and voxel under test (VUT) location. For a given set of these locations in $\Re^3$, the total bistatic Euclidean distance is illustrated in Figure 4.12.

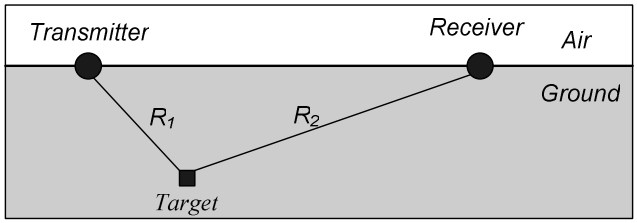

Figure 4.12 2D Euclidean distance: Transmitter to VUT to Receiver

While the transmitter and receiver locations remain fixed, the target's true location can vary in any number of directions. This variation is considered in two dimensions along an ellipse whose foci are defined by transmitter and receiver locations. The result is in an elliptical ambiguity associated with the distance calculated, as seen in Figure 4.13, since the SAR processor is not privy to information about the true target location.

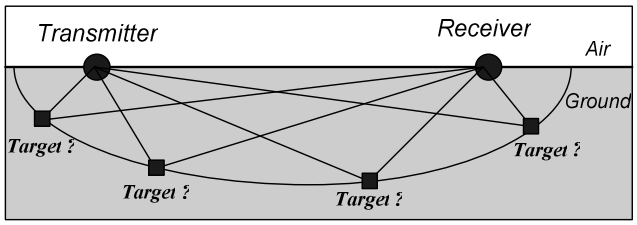

Figure 4.13 2D Euclidean distance: Elliptical

As the cross-sectional view shows in Figure 4.14, the volume of the imaged scene becomes an area under test and the VUT becomes a point under test (PUT). Additionally, multiple ellipses produced by different transmitter-receiver combinations for each PUT illustrate a common intersection point. It is this geometric agreement that allows the SAR processor to assign a quantitative pixel intensity to describe a given location. Given a greater number of ellipses that intersect for a given PUT increase, a larger intensity value for that PUT exists. In three dimensions, an ellipsoid (three-dimensional ellipse) is formed for each transmitter – VUT – receiver location specified. By repeating this process for every VUT, a SAR image is produced.

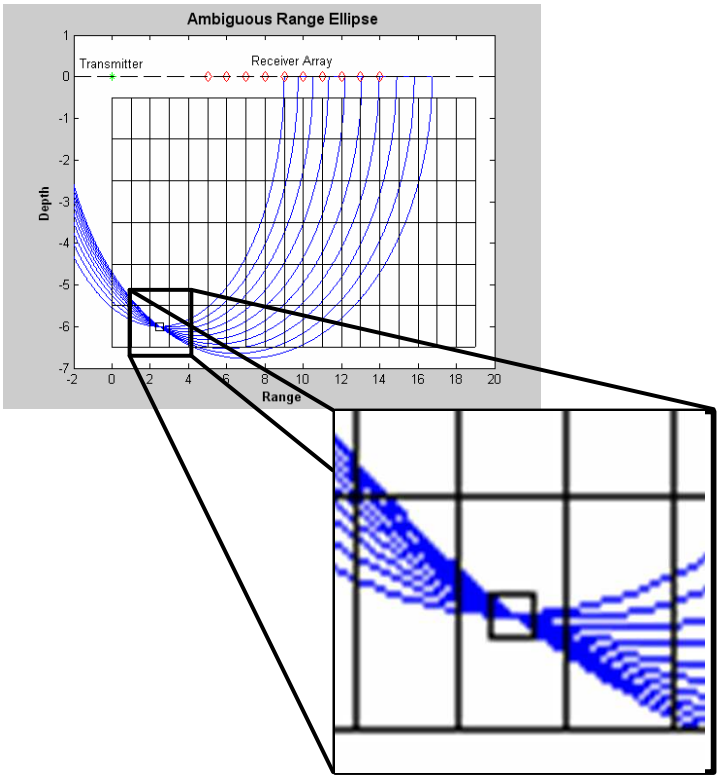

Figure 4.14 Area Under Test: Elliptical ambiguity for multiple receiver locations *(Image reproduced from [11] with authors permission)*

While this is a visual representation of SAR image formation, mathematically, the SAR processor actually employs an iterative sequence of phase alignment and weighting techniques. This processing relies solely on provided input data in the form of multiple time-dependent signals of varying amplitude and frequency in complex form. The average amplitude of return data from all receivers for a particular VUT is used as the intensity value that contributes to the SAR image. Since different VUT's will produce varying intensity values, often, the lesser of these can be interpreted as clutter in the SAR image. By increasing the threshold of the SAR data, this clutter can be removed and a clearer view of the intended return is available as seen in Figure 4.15.

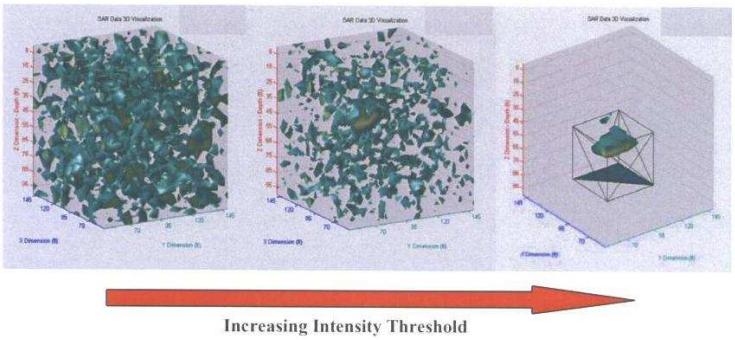

Figure 4.15 Increased threshold to reduce clutter *(Image reproduced from [11] with authors permission)*

A cleaner view of an isolated SAR image is shown in Figure 4.16.

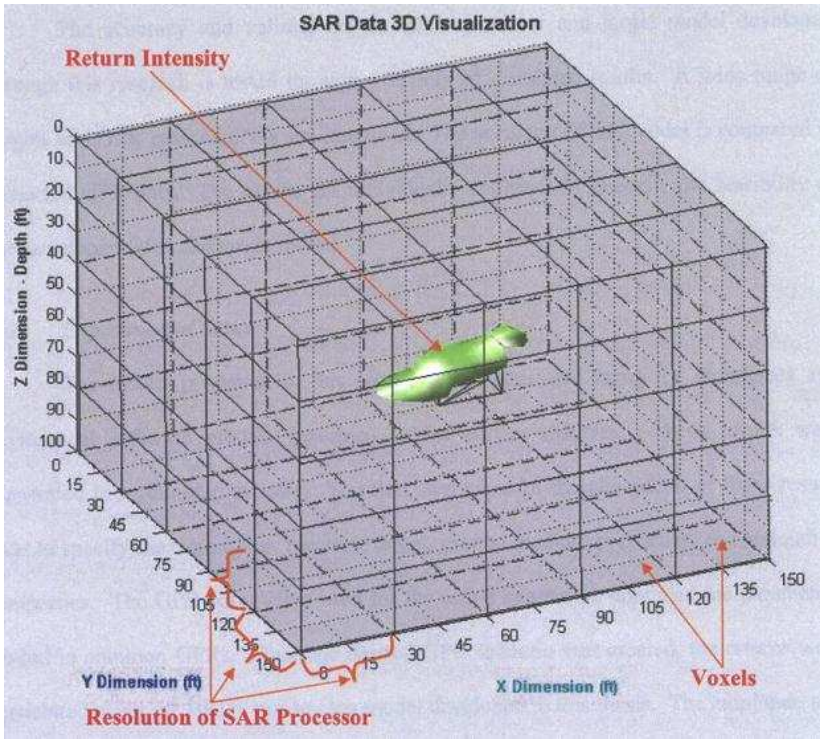

Figure 4.16 Increased threshold to reduce clutter *(Image reproduced from [11] with authors permission)*

Like the pre-image processor, the SAR processor is a modular signal processing tool that can be customized to suit a host of GPR scenarios. Its versatility is well suited to this GPR model.

Chapter 5

GPR and Target Model

To this point, the topics concerning ground penetrating radar have been addressed. The environment of operation, the hardware used, the energy interactions known to take place, and the necessary signal processing has been outlined to an extensive degree. The aim of this chapter is to discuss, in detail, the specifics associated with accurately modeling the raw data return associated with a GPR target. It has been discussed in Chapter 4 that the software initially developed by the Air Force Research Labs and Black River Systems can be segmented into three components: the GPR target model, the pre-image processor, and the SAR processor. Here we explain the first of these system blocks and the methods which allow the simulator to produce raw GPR data based on geometrically accurate energy interactions. This process requires three stages: 1) transmission of the initial energy from a source location, 2) recording attenuation during signal propagation and 3) tracking the signal through multiple target interactions while accounting for reflected energy at the receiver. The various contributors to the entire GPR scene (transmitter, receivers, target, and ground medium) shown in Figure 5.1, each carry their own unique modeling characteristics to combine into one comprehensive GPR target model.

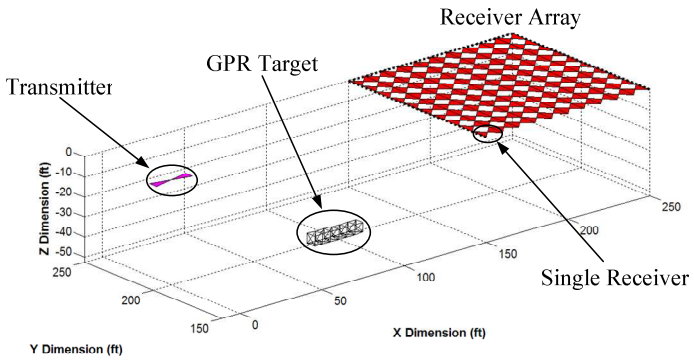

Figure 5.1 GPR Physical Hardware Scene Set-up

5.1 Transmission System: Antennas, Power and Ray Generation

The source location of energy is the transmitting antenna in the bistatic configuration. A wide-bandwidth, isotropic bow-tie antenna was chosen for this system. This antenna type has been shown, experimentally, to cater to the CWLFM signal used in GPR modeling and its uniform elevation and azimuth radiation patterns simplify the simulation of energy propagation. As discussed in Chapter 3, energy originates at the transmitting antenna in the form of electromagnetic waves. The complexity associated with the nature of these waves has led to the use of ray-tracing as an appropriate alternative. The gain and radiation patterns associated with the transmitting antenna combined with the power and direction characteristics of the rays modeled in the ray-tracing technique produce a versatile transmission system.

The power and direction associated with the transmit antenna must be truthfully represented when generating individual rays. Due to the isotropic nature of the bow-tie antenna, power will radiate uniformly in all directions analogous to a spherical shape. This power density is represented in (5-1).

$$P_d = \frac{P_t G}{4\pi R^2} \tag{5-1}$$

Based on the gain of the antenna (G), the amount of power transmitted in watts (P_t), and the distance to the target in meters (R), the amount of power received by a target at any distance is provided in Watts per meter squared. To obtain surface power reflected from the target, its RCS in (meters)^2, must be multiplied to this ratio to arrive at the total power received by the target.

In the case of the GPR simulator, the location of an intended target is known, *a priori*. Additionally, the target of interest is fragmented into smaller triangular facets to accommodate the geometry necessary for ray-tracing. Using this target distance from the transmitter and the definition of triangular facets, each generated ray is assigned to propagate to a specific target facet. As the distance of each facet from the transmit antenna changes, the power density can be adjusted accordingly and an initial amount of power incident to that facet can be modeled. The use of an isotropic radiator emphasizes the one-to-one relationship between the number of rays and the number of target facets of interest.

The rules governing the size and number of facets are rooted in the cross range resolution of the radar system. The resolution of radar is defined as the minimum detectable separation between two targets at a given distance from those targets. While the resolution of certain radar systems is dependent on the individual frequencies of the transmitted signal, SAR resolution is a function of the physical size of the individual receiver antennas. (3-4) describes the resolution as one half the physical length of the antenna aperture used to form the receiver array. As it relates to simulation, this resolution also controls the size of the triangular facets which compose the target of

interest. If the center of each of these target facets is defined with the appropriate separation, as specified by the system resolution, then this electrically accurate target can be incorporated into the GPR model. To accomplish this, Solid Works, a computer-aided design software tool, is used to generate a stereolithography (.STL) file type. The GPR target model includes handles to read in this file and execute an extensive geometric analysis relative to the locations of the transmitter, target, and receiver array. This analysis is discussed later in this chapter and an example of the .STL format with corresponding output is shown in Figure 5.2.

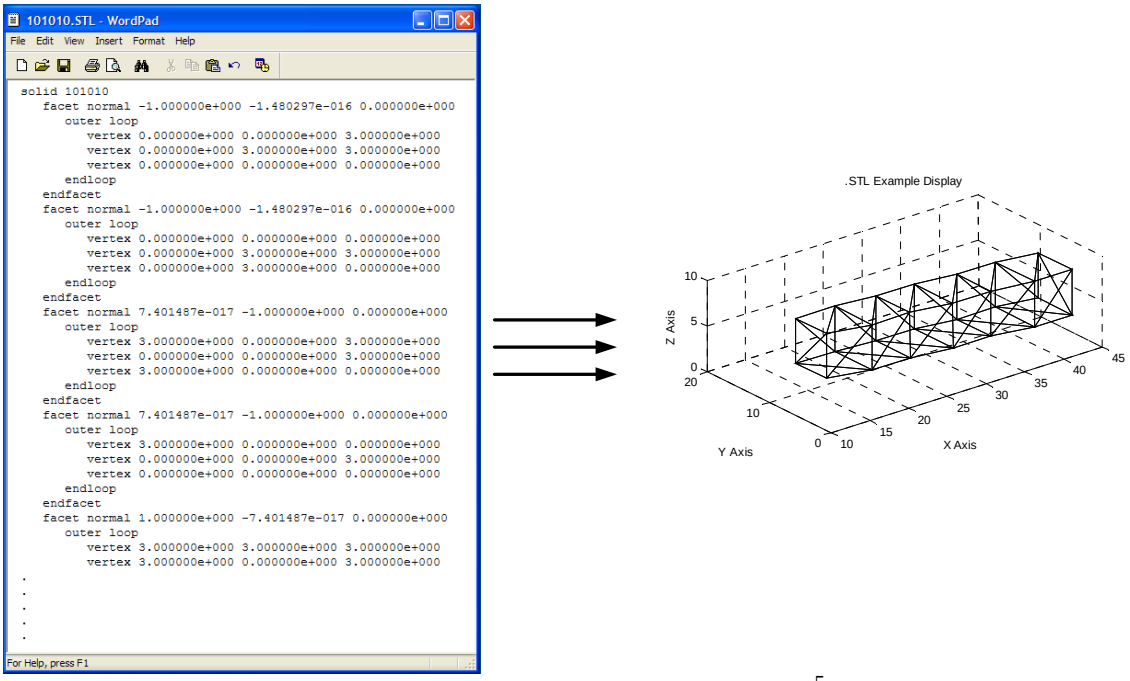

Figure 5.2 STL file format translation to MATLAB display[5]

Beyond the power capabilities of an antenna, its gain or directivity should be discussed. While the gain for this GPR model is unity for all isotropic antennas, certain applications may require focusing a larger percentage of the transmit power towards the intended target, assuming its location is known. By directing a larger portion of the

[5] Source code for plotting .STL file format in MATLAB provided by Dr. David Rosen, Georgia Institute of Technology

transmit power, a larger return is expected from the target. Given the same input power, the gain of any directive antenna is measured as a ratio of that power relative to a lossless, isotropic antenna. (5-2) outlines this ratio of values.

$$G = \frac{(Power\ Density)_{Directive\ Antenna}}{(Power\ Density)_{Lossless\ Isotropic\ Antenna}} \qquad (5\text{-}2)$$

Antenna gains are represented graphically in the form of two 2D radiation patterns with differing angle dependencies: azimuth and elevation. Represented in a spherical coordinate system, the azimuth plane consists of all angles in one complete rotation around a vertical axis, while the elevation plane encompasses all angles as measured from a horizontal plane. These spatial patterns jointly describe the direction in which the most power is radiated by an antenna. Since these patterns are calculated relative to isotropic radiation patterns, the maximum power in these patterns is commonly measured in dBi. A 3D example radiation pattern and its corresponding 2D azimuth and elevation patterns for the bow-tie antenna are found in Figures 5.3 and 5.4, respectively.

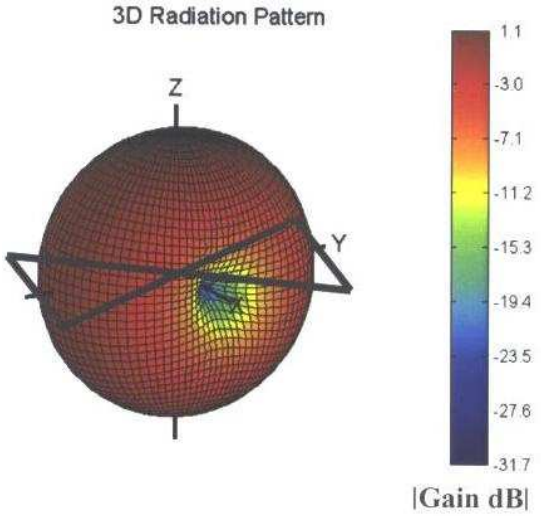

Figure 5.3 3D Bow Tie Antenna Radiation pattern *(Image reproduced from [11] with authors permission)*

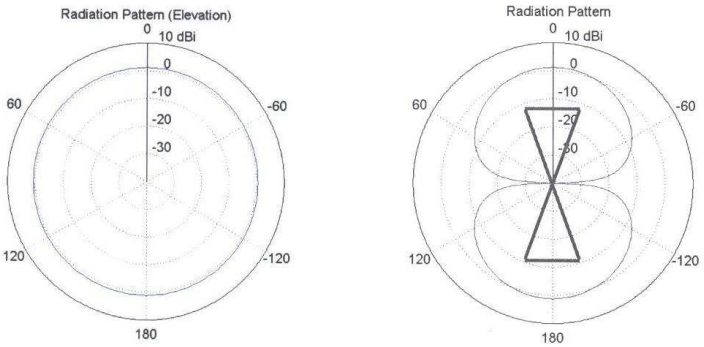

Figure 5.4 Elevation and Azimuth Radiation patterns *(Image reproduced from [11] with authors permission)*

As mentioned earlier, since only an isotropic antenna is considered for this research, directivity is not investigated; however, the GPR target model can accommodate the inclusion of customized antenna patterns to control the directivity of individual rays. Knowing the target facet locations and angular range associated with the desired radiation patterns, the initial power density associated with each transmitted ray can be scaled accordingly. A visual comparison between isotropic and directive ray-tracing GPR modeling is found below.

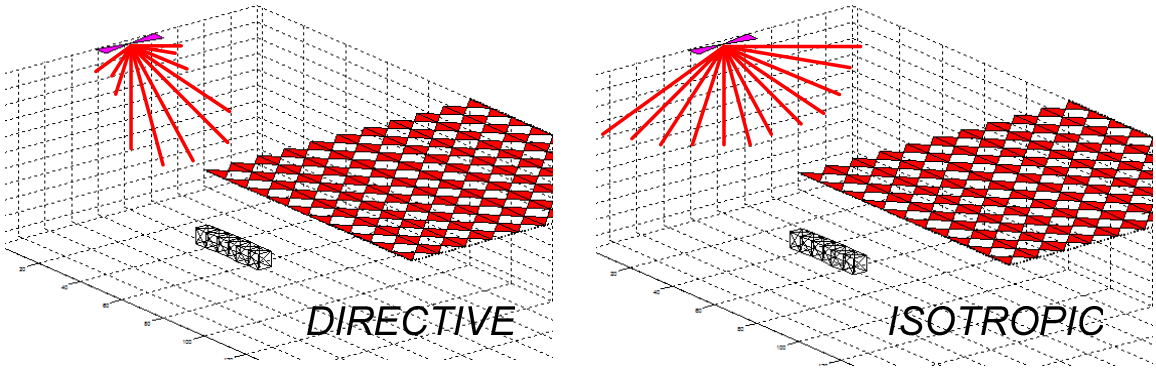

Figure 5.5 Isotropic versus Directive Ray-tracing

5.2 Attenuation

Another significant performance evaluator included in the GPR simulator is the inclusion of amplitude information. This is especially useful when determining the amount of attenuation a transmitted signal experiences as the ground medium or depth of

the target is varied for different experiments. The specific contributor to this type of signal degradation is the attenuation constant shown in Equation 5-3.

$$\alpha = \omega\sqrt{\mu\varepsilon}\left\{\frac{1}{2}\left[\sqrt{1+\left(\frac{\sigma}{\omega\varepsilon}\right)^2}-1\right]\right\}^{\frac{1}{2}} \quad [Np/m] \qquad (5\text{-}3)$$

Where α ≡ Attenuation constant
ε ≡ Absolute permittivity
σ ≡ Conductivity
μ ≡ Absolute permeability
ω ≡ Angular frequency

This constant represents a mathematical dependence on ground medium properties discussed in Chapter 3. Given the signal frequency, conductivity, permittivity and permeability value, attenuation can be calculated for any medium. The nature of this attenuation factor is represented graphically in Figure 5.6 where the attenuation constant is plotted as a function of frequency in the [1 – 10 MHz] range.

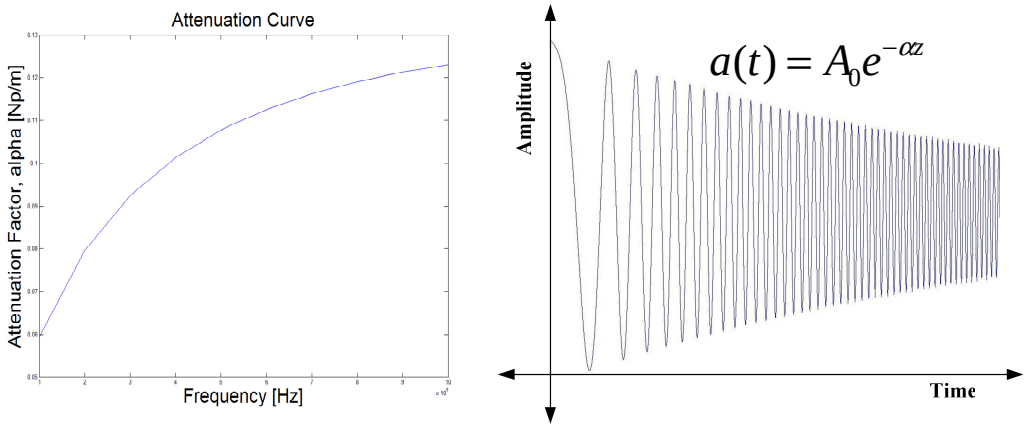

Figure 5.6 Attenuation curve and signal effect

As seen in the figure, the greatest degree of signal attenuation occurs at the higher order frequencies. The current target model demonstrates its fidelity with respect to the ability to incorporate this attenuation feature in the simulated GPR scenarios. This work is based on homogeneous targets in a homogeneous ground medium and the signal attenuation

experienced at multiple frequencies. Future work, as discussed in Chapter 7, may consider a heterogeneous medium of propagation, as shown in Figure 5.7

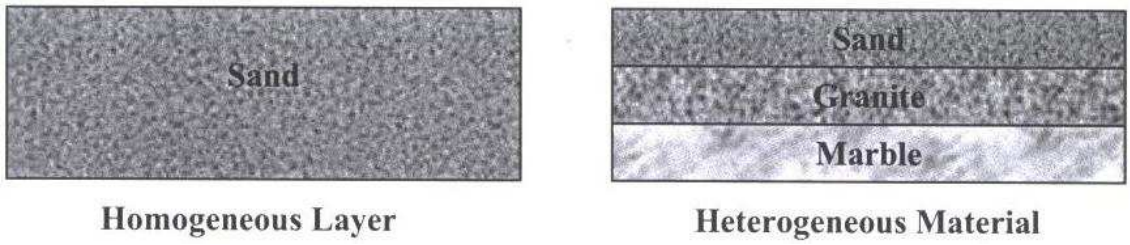

Figure 5.7 Homogeneous vs. Heterogeneous Layers *(Image reproduced from [11] with authors permission)*

5.3 Geometric Energy Interactions and BRDF

The final step that completes an accurate GPR target model is the calculation and tracking of the multiple subsurface ray transmissions, reflections, and target refractions that occur. This GPR model incorporates both specular and diffuse types of reflections using the BRDF, described in preceding chapters, and significantly affects the distribution of energy throughout the underground scene. Due to the intricate nature of the target composition and the potentially numerous energy interactions expected to take place, a framework is required to control how return energy will be recorded. Following the path of propagation from transmitter to target and target to receiver, the interactions at each waypoint are meticulously outlined.

5.3.1 Initial Energy Effects

Beginning at the transmitter, previous work by Kapfer investigated the effects of the air-soil interface. This was only necessary when modeling GPR scenes with the transmitter located several feet above the ground. Unfortunately, there are negative effects associated with this above-ground signal transmission. These effects can be traced back to the complex phenomenology involved when an electromagnetic signal propagates from air to a medium with a considerably higher dielectric permittivity.

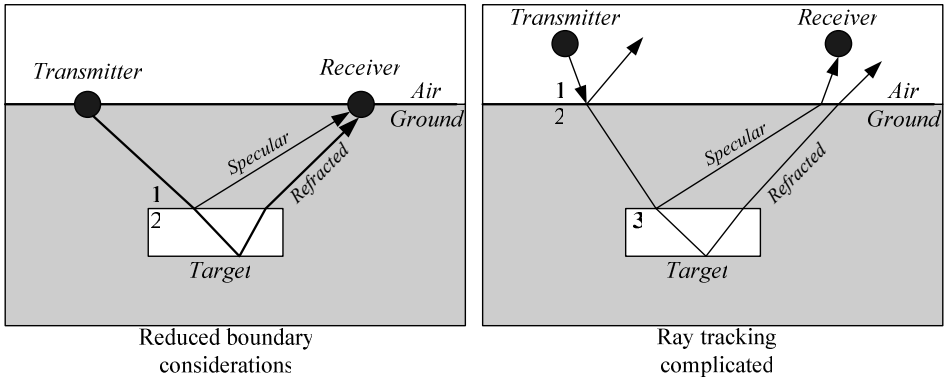

Figure 5.8 Transmitter/ Receiver location: Buried versus above ground scenario

The validity of the ray-tracing concept is also compromised, therefore rendering the model as flawed and inconsistent. Based on this research and other experimental findings [31], it has been determined that a more successful target return is accomplished by placing the transmitting antenna directly on the surface or buried within the same ground medium as the target.

Another interaction discussed by Kapfer but not investigated in this work is the effect of direct path on signal return. This is experienced in the form of ambiguous return energy at the receiver. One such complication includes barely attenuated signals reaching the receiver as a result of direct path and effectively saturating information contained in true return signals from the subsurface target. Bypassing the intended path through the ground medium and propagating directly to the receiver causes additional complications in processing, as discussed in [1], [11] and Chapter 4. The value of directive antenna models is emphasized as direct path can be avoided by radiating less power in the direction of other antennas in close proximity to each other. This GPR target model allows simulated target returns with and without direct path by assigning individual rays to the front end receivers used in the scene.

5.3.2 Initial, Secondary, and Final Target Interactions

There are an infinitely large number of reflections and transmissions that proliferate in a GPR scene when considering energy incident upon a target surface. Realistically, all of these interactions can not be accounted for. Even using ray-tracing, the amplitude associated with each propagated ray tends to be significantly small and undetectable by the receiver array. As mentioned earlier, a structured plan of evaluation must be defined in order to account for those rays which maintain enough power to be detected, their phase recorded and collected for pre-image processing. This plan is outlined as a definition of Initial Target Interactions (ITI), Secondary Target Interactions (STI), and Final Target Interactions (FTI). At each of these points, both specular and diffuse energy interactions are considered with respect to the transmitting antenna and receiver array. The BRDF and the geometric analysis of reflected rays inside and outside of the modeled target are discussed in detail. This plan accounts for the accuracy in return power recorded at the receiver array.

The verity of the target model relies heavily on calculating the BRDF at a number of locations. These locations are defined as the center of each triangular facet used to describe the target in 3D space. Both the size of the facet area and distance between each center point is dictated by the SAR resolution. Consequently, this resolution is a function of the physical receiver antenna size (3-4). Based on the BRDF geometry, the angle definitions and the Fresnel Spectral approximation made by Kapfer, the BRDF is calculated at each target boundary using the composite relationship in Equation (5-4).

$$BRDF = \frac{1}{2}\left(\sqrt{\frac{p}{p^2 - p^2\cos^2\varphi + \cos^2\varphi}} + \frac{1-r}{4\pi\cos\theta\cos\theta'}\left(\frac{r}{\left(1 + r\cos^2\alpha - \cos^2\alpha\right)^2}\right)\sqrt{\frac{p}{p^2 - p^2\cos^2\varphi + \cos^2\varphi}}\right)\left(R_\perp + R_\parallel\right) \quad (5\text{-}4)$$

Where
- r ≡ Roughness factor
- p ≡ Isotropy factor
- R ≡ Perpendicular polarization power term
- R ≡ Parallel polarization power term
- α ≡ Angle from microfacet normal to bisector vector
- θ ≡ Angle from microfacet normal vector to observed vector
- θ' ≡ Angle from microfacet normal to incident energy vector
- φ ≡ Angle between observed projection vector and bisector projection vector

This quantity represents the percentage of incident power at a dielectric boundary reflected (or observed) from a particular location given a specific source position. The most heavily weighed factors in the calculation are the difference in dielectric permittivity, the specular and directional controls, and the three critical locations (source, incident plane, and observer). For the GPR scene, these parameters fit well into the simulation model since only the receiver (or observed) location is varied. To consider a point source target, a 3D color representation is helpful in visualizing the return power distribution of the BRDF.

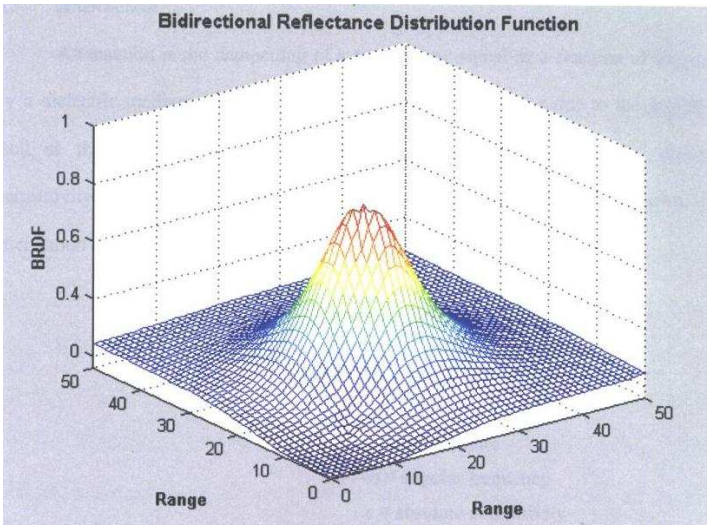

Figure 5.9 Three dimensional BRDF representation *(Image reproduced from [11] with authors permission)*

This point source exhibits isotropic reflections for a given transmitter and receiver array and shows the uniform distribution of return power across the receiver grid. A majority of the energy is located at the center of the synthetic receiver indicating specular reflections, while the diminishing intensities are representative of more diffuse reflections. The locations of these intensities make use of the roughness and isotropy control variables discussed in detail by Kapfer [11].

In determining ITI locations, information for each triangular facet of the target is extracted and stored based on the transmitter and target location. The uniqueness of the geometry requires knowing these fundamental descriptors:

1. The [x y z] coordinates for each of the three points that describe the facet.
2. The center point of the facet.
3. The normal vector describing the direction of the facet in space.
4. The D coefficient to describe the distance of the facet from the origin.
5. Flag values used to indicate whether incident energy will totally internally reflect or partially refract through the facet.

Similar to work by Jeter [1], each facet is represented mathematically by a 6 x 3 grid of data as shown in Table 5.1.

$Point\ 1_x$	$Point\ 2_x$	$Point\ 3_x$	$Center_x$	$Normal_x$	*D Coeff.*
$Point\ 1_y$	$Point\ 2_y$	$Point\ 3_y$	$Center_y$	$Normal_y$	*Total Internal Reflection Flag*
$Point\ 1_z$	$Point\ 2_z$	$Point\ 3_z$	$Center_z$	$Normal_z$	*N/A*

Table 5.1 Facet information storage format

Previous work was limited in modeling targets with the basic shape of a cube, only providing for variations in height, length, or width. A significant upgrade to the GPR simulator is the capability to model targets of any size and shape. This is accomplished using Solid Works, and provides the end-user the ability to create an expanded variety of shapes, assuming the individual facet size corresponds to the system resolution. With this extended capability comes an inherent complexity in the individual analysis of each facet with respect to the transmitter and receiver array, thus the need for each of the columns of data outlined in Table 5.1. This target information is used throughout analysis of the remaining target interactions however it is deliberately collected during the ITI phase of simulation. This allows the information to be segregated into those facets which will totally internally reflect incident power and those that will not.

Using an iterative process, the BRDF is calculated at each receiver for an individual target facet. Taking into consideration the attenuation experienced as a ray propagates through the ground medium, the amount of power a particular receiver will observe is determined. Since each receiver has a different position in the array, this

BRDF value is subject to variation, especially depending on the orientation of the target facet. This is seen in Figure 5.10.

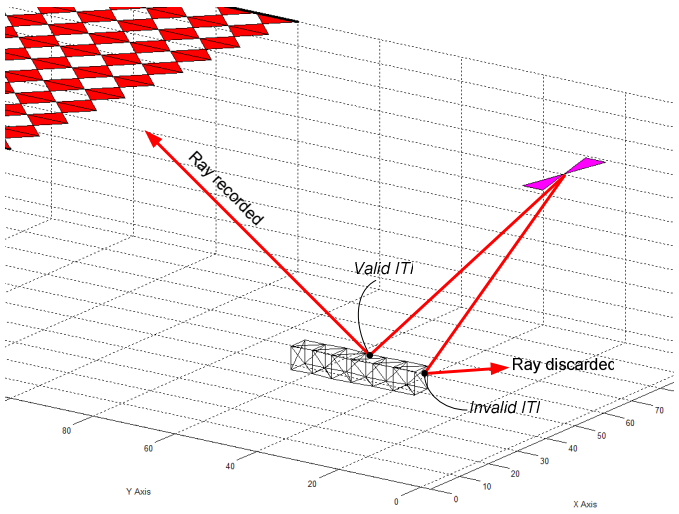

Figure 5.10 Ray-Target facet intersection: Valid versus Invalid

Here, the amount of power observed from a facet directed towards the receiver array will be significantly greater than that from a facet angled horizontally and away from the receiver array. Whether or not total internal reflection occurs, the aim of ITI analysis only requires that the observed power by each receiver be recorded for every facet that is guaranteed to reflect energy. The GPR simulator accounts for those facets which are directed at an angle that would prevent any energy from being observed by any receiver in the array. These interactions are ignored since they do not contribute to the total return.

Once a facet has been identified as an ITI which does not totally internally reflect, it is inferred that a percentage of incident power will refract through that facet in the form of a ray. STI and FTI analysis immediately follow this in a cascaded sequence of “if” statements. Before any additional return energy is calculated, it must be determined whether the refracted ray will propagate back through the GPR scene and intersect with a receiver. Again, there are a potentially large number of rays which may propagate

through the modeled scene; however, these rays are of no interest unless they can be traced back to the receiver array.

Both STI and FTI calculations rely heavily on previous work by Glassner. The intersection between the refracted ray and another target facet (from within the whole target) is calculated and the intersection point is recorded. Glassner's method for accomplishing this is perfectly suited for this application as it requires determining the intersection between a straight line and a triangular plane. Jeter explains this method as it relates to this application [1]. While only one STI will be identified for each ray refracted through the target initially, the complexities associated with the BRDF become a factor in identifying valid FTI facets.

The occurrence of an STI indicates that energy is reflected in both specular and diffuse forms from inside the target as shown in Figure 5.11.

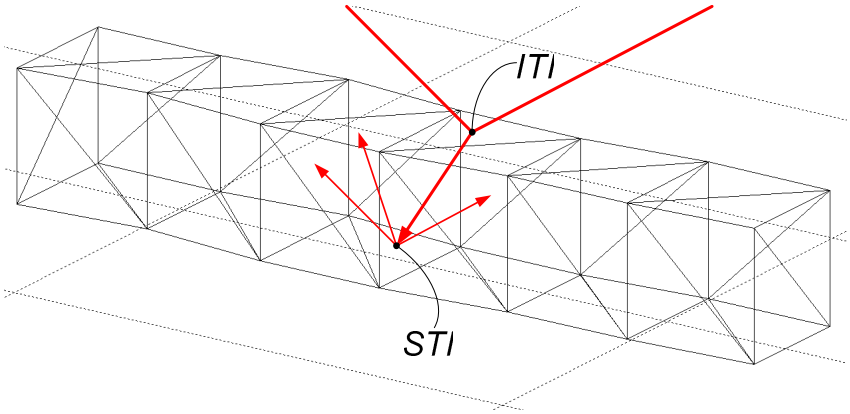

Figure 5.11 STI Occurrence

As a result, during FTI analysis, two questions must be answered in the affirmative to consider recording any power at the receiver array beyond ITI reflections: 1) Do any of the surrounding facets observe reflected energy internally from the STI? If so, which of these will refract a portion of the observed energy to the receiver array? These are identified as valid FTI facets. The receiver array is segmented into individual triangular

facets and once again, Glassner's techniques are implemented to determine the intersection between ray refracted from the FTI and the appropriate receiver in the grid. This is depicted in Figure 5.12.

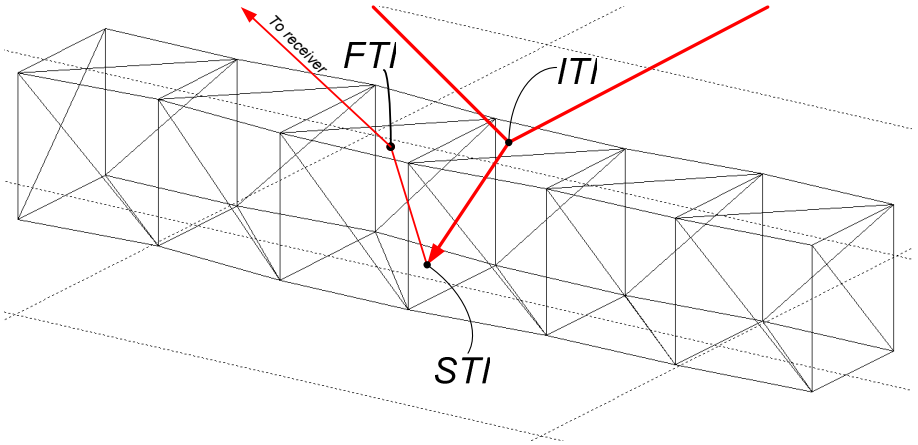

Figure 5.12 FTI facet refraction towards receiver

Throughout STI and FTI analysis, the attenuation of the ray as it propagates through the target and back to the receiver array is recorded. Both a power value associated with the attenuated ray and a phase value associated with the path of propagation are stored as a received signal by the simulator. Combined with the reflections from the ITI facets, this information is sent as a set of modulated chirp signals to the pre-image processor.

This format of analysis and sequence of evaluation provides a more geometrically accurate target model and furthers the development of a valid GPR simulation tool.

Chapter 6

Analysis and Results

The uniqueness of this target model as compared to previous models led to complications in pre-image processing and SAR processing, thus a more direct approach was taken to analyze the return data. While many of the principles related to SAR are inherent in the results displayed in Chapter 6, the pre-image processing and SAR processing methodology are not implemented. Instead, target modeling is accomplished by interpolating the known raw return power from the target and true target facet positions to produce visual estimate of the energy returned.

6.1 Experimental Setup

The results presented in this section were obtained based on the radar methodology and software discussed earlier. Modifications to the software have allowed results to be obtained more quickly than in previous versions. This is primarily attributed to the removal of the pre-image and SAR processing stages of the software. As in previous versions, experiments begin with a definition of the GPR scene. A host of parameters are specified, including target, transmitter, and receiver array locations. Also included are the ground and target medium characteristics (permittivity, permeability, conductivity), frequency of operation, and transmitted power. Once the scene is defined, the radar return is collected, sorted and a 3D image of interpolated power values is available along with a 2D X-Y plane slice of that image. The total power received by the reflecting target is included in the 3D image while the maximum power in the cross section of the interpolated image is displayed in the 2D image.

6.2 Layout of Results

The results presented in this chapter are segmented into two categories. The first category considers GPR simulations demonstrating the capabilities of the current model. The parametric nature of the software allowed this to be accomplished through variations in system frequency, target position, ground medium properties, target composition, and transmitter configuration. The second category of results investigates improvements in 3D target imaging as compared with the previous model with respect to orientation and receiver location during raw data collection. Assumed constants throughout the simulations included half specular, half isotropic target surface properties characterized by adjusting the roughness (*r*) and isotropy (*p*) BRDF factors accordingly. Other constants included the transmission of 10 W of power to more quickly calculate percentage of return power and a physical antenna size of 10 feet to accommodate the system resolution. An outline of the results section is found below:

1. Capabilities of current model
    a. Variable frequency at target location/orientation 1 (Symmetric)
    Constants: TX/ RX location, RX size, ground medium, target medium
    Purpose: Show attenuation at low-end, mid-point, and high-end frequencies
        i. 1 MHz
        ii. 5 MHz
        iii. 10 MHz
    b. Variable frequency at target location/orientation 2 (Asymmetric)
    Constants: TX/ RX location, RX size, ground medium, target medium
    Purpose: Show attenuation at low-end, mid-point, and high-end frequencies
        i. 1 MHz
        ii. 5 MHz
        iii. 10 MHz

c. Variable target depth location, orientation 2 (Symmetric)
Constants: TX/ RX location, RX size, ground medium, target medium, low-end frequency
Purpose: Show attenuation at low-end, mid-point, and high-end frequencies
   i. **20 feet**
   ii. **50 feet**
   iii. **100 feet**
   iv. **150 feet**
   v. **200 feet**

d. Variable ground medium
Constants: TX/ RX location, RX size, target medium, frequency
Purpose: Show variable differences in attenuation at low and high frequencies
   i. **Fine rocky soil (ε_r = 14, μ_r = 1, σ = 2 e-3 S/m)**
      1. 1 MHz, 10 MHz
   ii. **Arid dessert (ε_r = 3, μ_r = 1, σ = 5e-5 S/m)**
      1. 1 MHz, 10 MHz

e. Variable ground medium
Constants: TX/ RX location, RX size, ground medium, frequency
Purpose: Show variable differences in attenuation at low and high frequencies
   i. **Air filled (ε_r = 1, μ_r = 1, σ = 0 S/m)**
      1. 1 MHz, 10 MHz
   ii. **Perfect conductor, copper (ε_r = (0 – 1e-6, μ_r = 1, σ = 5.8e7 S/m)**
      1. 1 MHz, 10 MHz

f. Multiple TX locations
Constants: RX location, RX size, ground medium, target medium, frequency
Purpose: Show increase in return power at varied transmit locations, 10 Watts
   i. **Single transmitter**
   ii. **Dual transmitter**
   iii. **Quadrupled transmitter**

g. Extended RX grid
Constants: TX/RX location, ground medium, target medium, frequency
Purpose: Show increase in return power and image improvement using a larger receiver array
   i. **Single RX location**

h. Complex target
Constants: RX location, RX size, ground medium, target medium, frequency
Purpose: Show increase in return power at varied transmit locations, 10 Watts
   i. **Randomly-shaped target 1 return**

2. Improvements over previous model
    a. Old SAR image Vs. New Model image
    Constants: TX/RX location, RX size, ground medium, target medium, frequency
    Purpose: Show excess ambiguity versus clearer target depiction
        i. Target 1
        ii. Target 2
    b. Variable RX location
    Constants: TX location, RX size, ground medium, target medium, frequency
    Purpose: Show excess awkward ambiguity versus clearer target depiction
        i. RX location 1
        ii. RX location 2

6.3 Results of Simulated Experiments

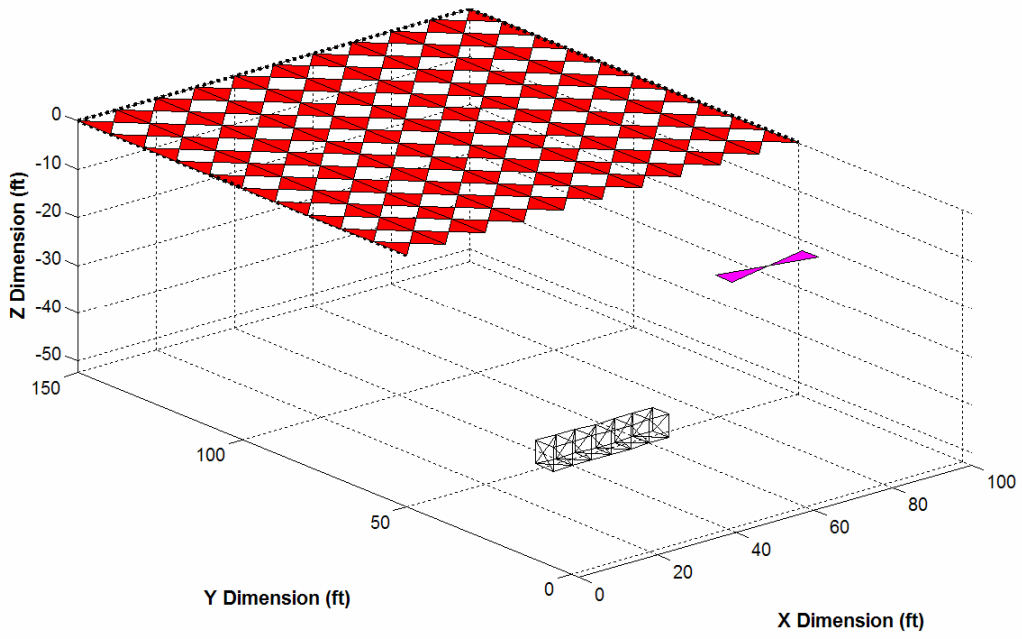

Figure 6.1 Air-filled target symmetric with respect to transmitter and receiver at 1 MHz

Transmitter:
Location: 50’ x 0’ x 0’
Power: 10 W
Frequency: 1 MHz

Receiver:
Location: 50’ x 100’ x 0’
Size: 100’ x 100’
Spacing: 10’ x 10’

Target:
Location: 50’ x 50’ x -50’
Size: ~30’ x 5’ x 5’
Air Filled
BRDF Roughness Factor: 0.5
BRDF Isotropy Factor: 0.5

Ground:
Permittivity: 14
Permeability: 1
Conductivity: 2 mS/m

In this scenario, Figure 6.1 depicts an air-filled target placed symmetrically between the transmitting and receiving antennas. The target is buried 50 ft. below the Earth's surface parallel to the X dimension in an assumed homogeneous medium with dielectric permittivity of 14, permeability of 1, and conductivity of 2 mS/m. This medium is characteristic of a fine rocky soil. The transmitting antenna transmits 10 W of power at a frequency of 1 MHz. Solid Works allowed the definition of 52 distinct target facets each with an approximate surface area of 1.125 m^2 (12.5 ft^2) and center separation of 1.5 m to satisfy the SAR system resolution requirement. MATLAB 3D interpolation function *griddata3* was used to map the integrated return power acquired for each target facet to its appropriate location in the GPR scene.

The 3D image produced in Figure 6.2 portrays the true target's size and orientation. The vertical offset in the 3D approximation is attributed to the lack of power return from the bottom of the target. Since all the return power consisted of ITI reflections, only energy from the surface of the target was available. MATLAB interpolation limits the target representation in the Z dimension. In the 2D image, shown in Figure 6.3, due to the location of the target, a majority of the energy reflected in the spectral direction is received by the center of the receiver array. Complementary to energy in the spectral direction, diffuse reflections are indicated by the lower intensity hue at each end of the image. The limitations in the interpolation scheme and scaling hinder the target dimension accuracy in the generated images. The total detectable power reflected by the target is calculated as 196.5078 mW (1.97%). At the low end of the range of frequencies considered in this simulation [1 MHz – 10 MHz], this is determined to be the greatest amount of power that can be received.

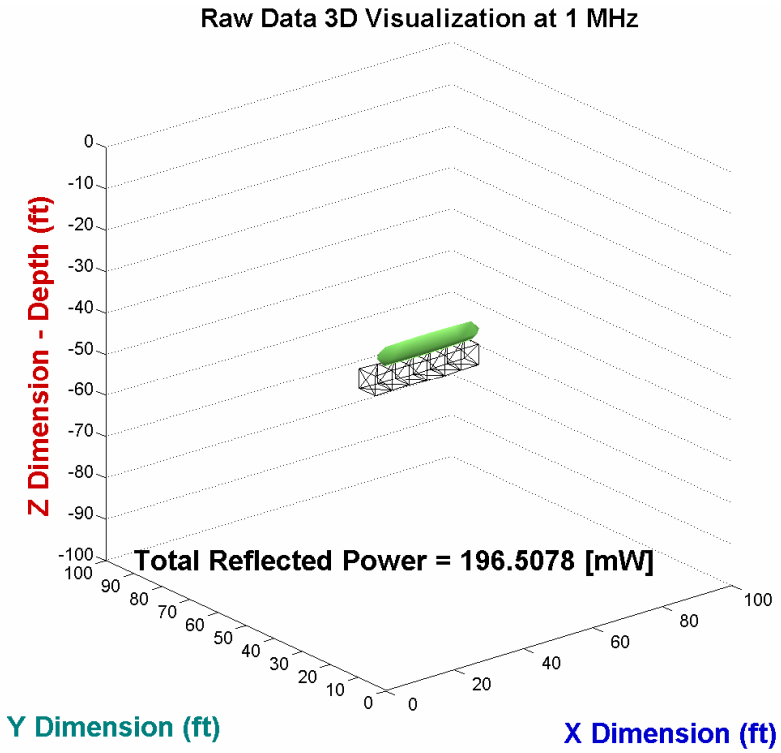

Figure 6.2 3D interpolation of radar return for air-filled target symmetric with respect to transmitter and receiver at 1 MHz

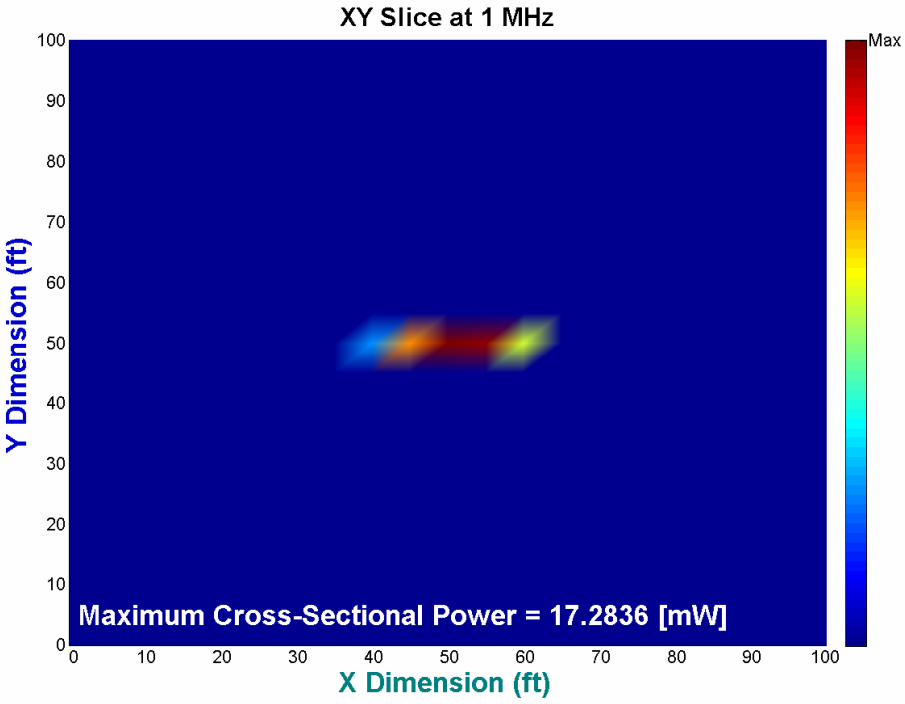

Figure 6.3 2D image of air-filled target symmetric with respect to transmitter and receiver at 1 MHz

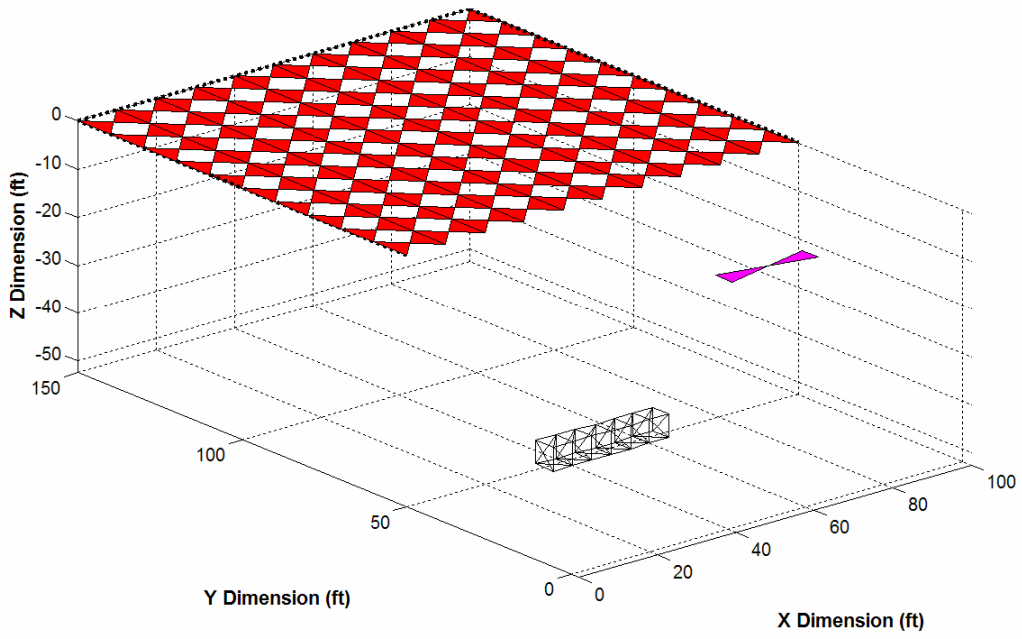

Figure 6.4 Air-filled target symmetric with respect to transmitter and receiver at 5 MHz

Transmitter:
Location: 50’ x 0’ x 0’
Power: 10 W
Frequency: 5 MHz

Receiver:
Location: 50’ x 100’ x 0’
Size: 100’ x 100’
Spacing: 10’ x 10’

Target:
Location: 50’ x 50’ x -50’
Size: ~30’ x 5’ x 5’
Air Filled
BRDF Roughness Factor: 0.5
BRDF Isotropy Factor: 0.5

Ground:
Permittivity: 14
Permeability: 1
Conductivity: 2 mS/m

In this scenario, Figure 6.4 depicts an air-filled target placed symmetrically between the transmitting and receiving antennas. The target is buried 50 ft. below the Earth's surface parallel to the X dimension in an assumed homogeneous medium with dielectric permittivity of 14, permeability of 1, and conductivity of 2 mS/m. This medium is characteristic of a fine rocky soil. The transmitting antenna transmits 10 W of power at a frequency of 5 MHz. Solid Works allowed the definition of 52 distinct target facets each with an approximate surface area of 1.125 m^2 (12.5 ft^2) and center separation of 1.5 m to satisfy the SAR system resolution requirement. MATLAB 3D interpolation function *griddata3* was used to map the integrated return power acquired for each target facet to its appropriate location in the GPR scene.

The 3D image produced in Figure 6.5 portrays the true target's size and orientation. The vertical offset in the 3D approximation is attributed to the lack of power return from the bottom of the target. Since all the return power consisted of ITI reflections, only energy from the surface of the target was available. MATLAB interpolation limits the target representation in the Z dimension. In the 2D image, shown in Figure 6.6, due to the location of the target, a majority of the energy reflected in the spectral direction is received by the center of the receiver array. Complementary to energy in the spectral direction, diffuse reflections are indicated by the lower intensity hue at each end of the image. The limitations in the interpolation scheme and scaling hinder the target dimension accuracy in the generated images. The total detectable power reflected by the target is calculated as 93.6334 mW (0.93%). At the midpoint of the range of frequencies considered in this simulation [1 MHz – 10 MHz], this is determined to be the average amount of power that can be received.

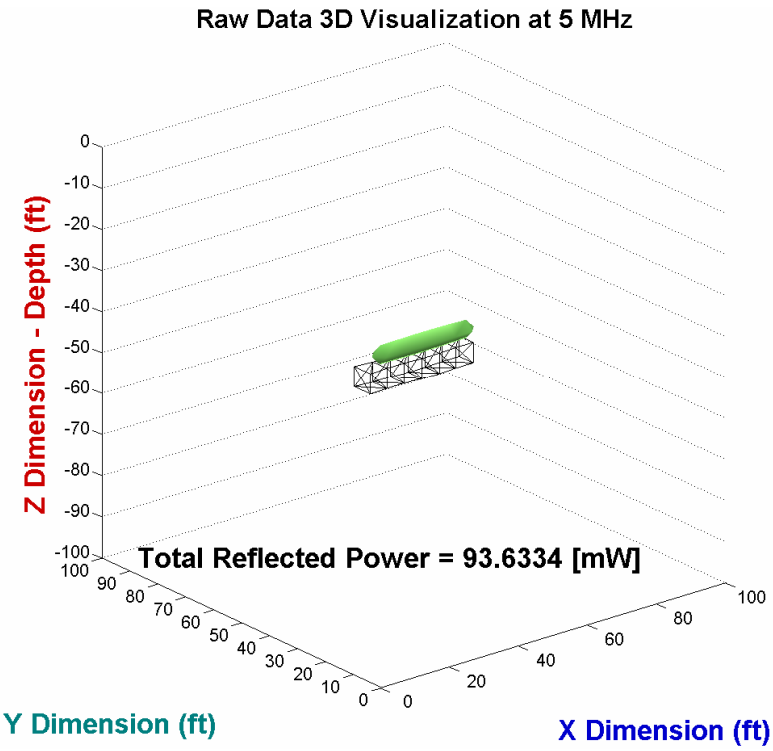

Figure 6.5 3D interpolation of radar return for air-filled target symmetric with respect to transmitter and receiver at 5 MHz

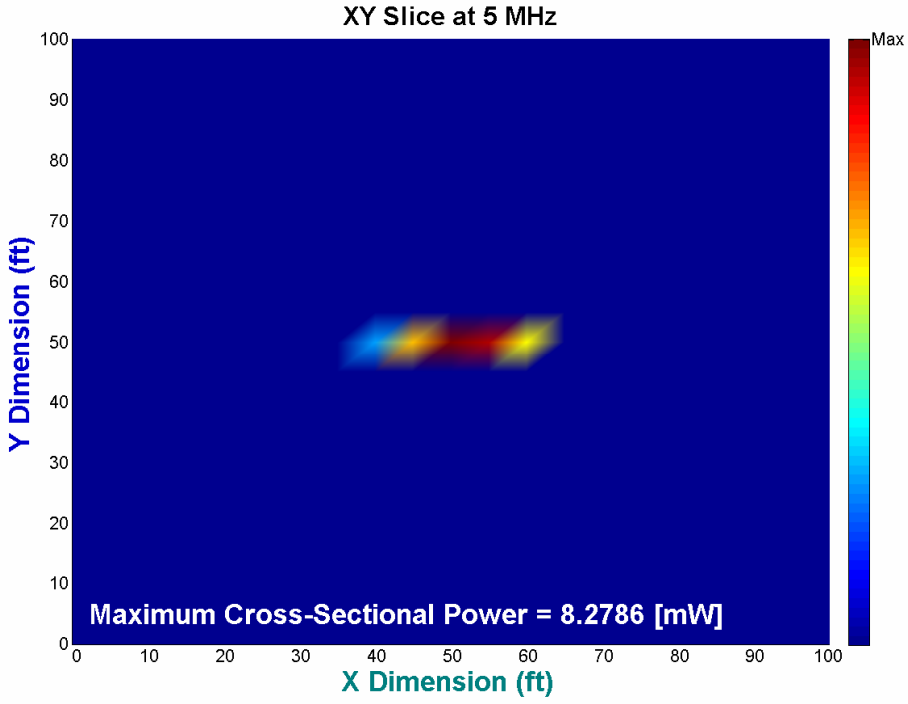

Figure 6.6 2D image of air-filled target symmetric with respect to transmitter and receiver at 5 MHz

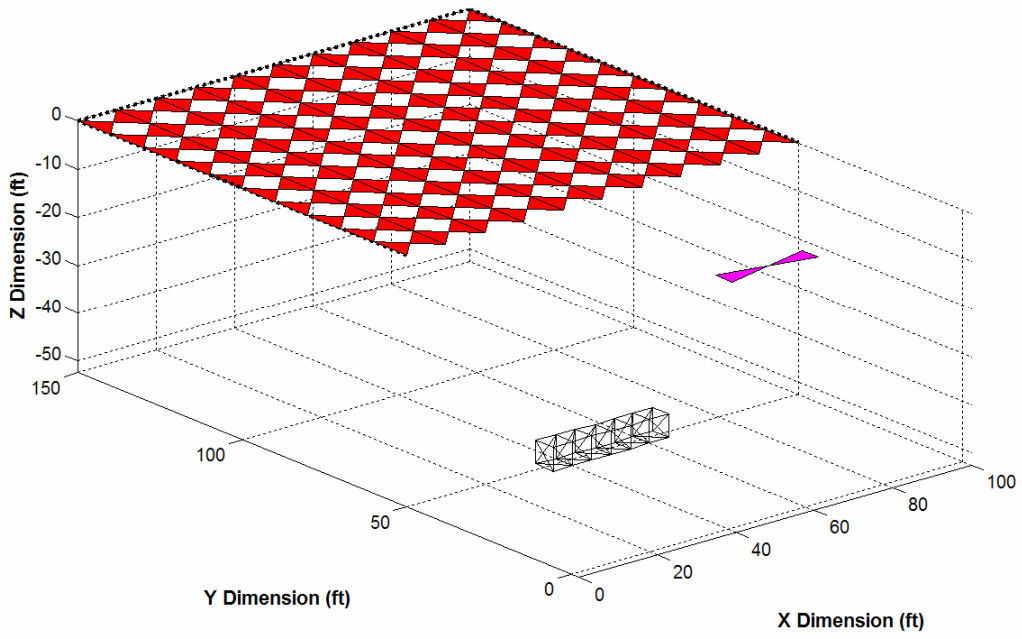

Figure 6.7 Air-filled target symmetric with respect to transmitter and receiver at 10 MHz

Transmitter:
Location: 50’ x 0’ x 0’
Power: 10 W
Frequency: 10 MHz

Receiver:
Location: 50’ x 100’ x 0’
Size: 100’ x 100’
Spacing: 10’ x 10’

Target:
Location: 50’ x 50’ x -50’
Size: ~30’ x 5’ x 5’
Air Filled
BRDF Roughness Factor: 0.5
BRDF Isotropy Factor: 0.5

Ground:
Permittivity: 14
Permeability: 1
Conductivity: 2 mS/m

In this scenario, Figure 6.7 depicts an air-filled target placed symmetrically between the transmitting and receiving antennas. The target is buried 50 ft. below the Earth's surface parallel to the X dimension in an assumed homogeneous medium with dielectric permittivity of 14, permeability of 1, and conductivity of 2 mS/m. This medium is characteristic of a fine rocky soil. The transmitting antenna transmits 10 W of power at a frequency of 10 MHz. Solid Works allowed the definition of 52 distinct target facets each with an approximate surface area of 1.125 m^2 (12.5 ft^2) and center separation of 1.5 m to satisfy the SAR system resolution requirement. MATLAB 3D interpolation function *griddata3* was used to map the integrated return power acquired for each target facet to its appropriate location in the GPR scene.

The 3D image produced in Figure 6.8 portrays the true target's size and orientation. The vertical offset in the 3D approximation is attributed to the lack of power return from the bottom of the target. Since all the return power consisted of ITI reflections, only energy from the surface of the target was available. MATLAB interpolation limits the target representation in the Z dimension. In the 2D image, shown in Figure 6.9, due to the location of the target, a majority of the energy reflected in the spectral direction is received by the center of the receiver array. Complementary to energy in the spectral direction, diffuse reflections are indicated by the lower intensity hue at each end of the image. The limitations in the interpolation scheme and scaling hinder the target dimension accuracy in the generated images. The total detectable power reflected by the target is calculated as 87.6246 mW (0.87%). At the high end of the range of frequencies considered in this simulation [1 MHz – 10 MHz], this is determined to be the least amount of power that can be received.

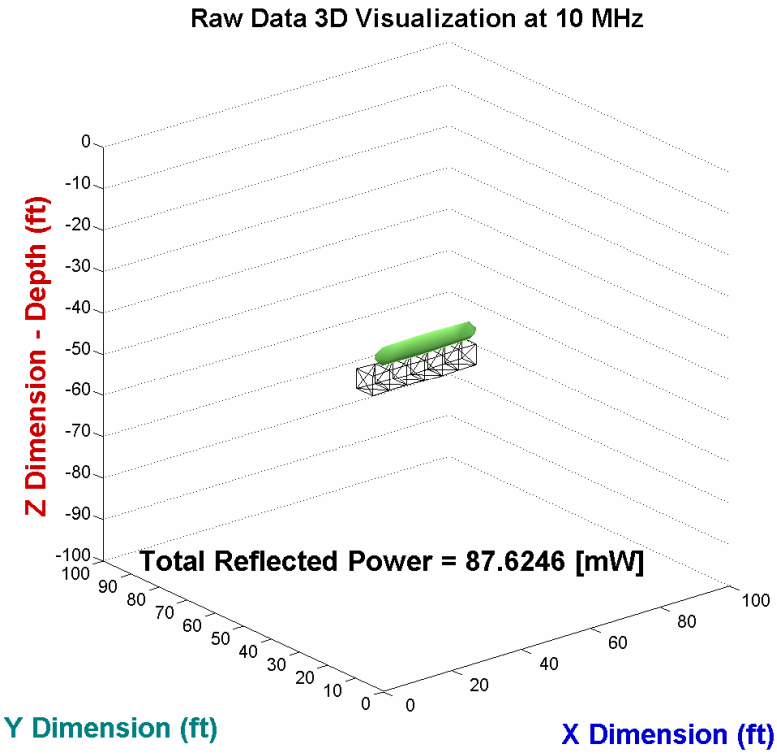

Figure 6.8 3D interpolation of radar return for air-filled target symmetric with respect to transmitter and receiver at 10 MHz

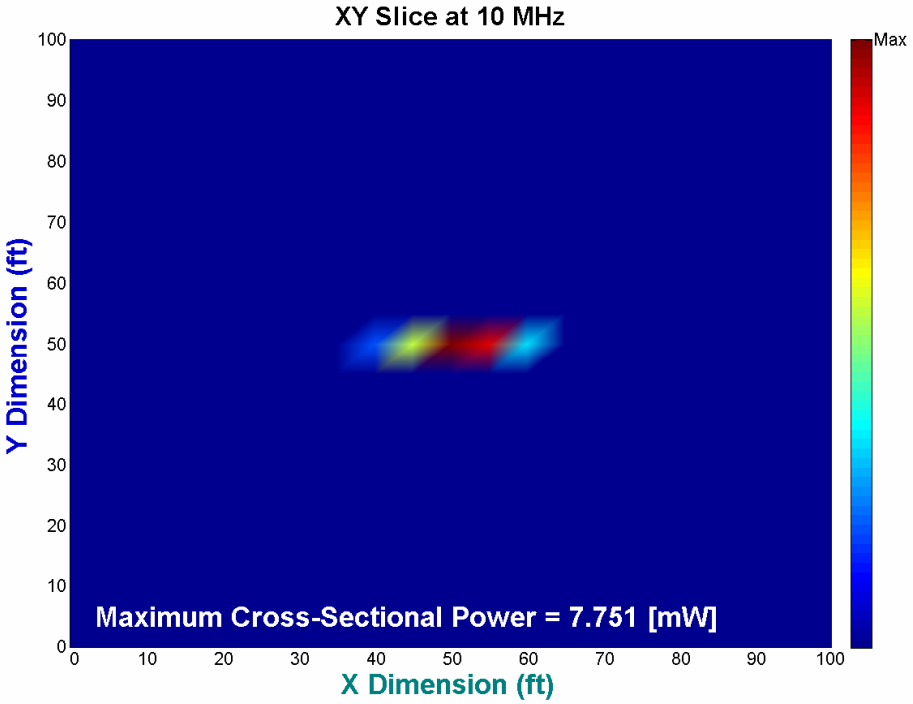

Figure 6.9 2D image of air-filled target symmetric with respect to transmitter and receiver at 10 MHz

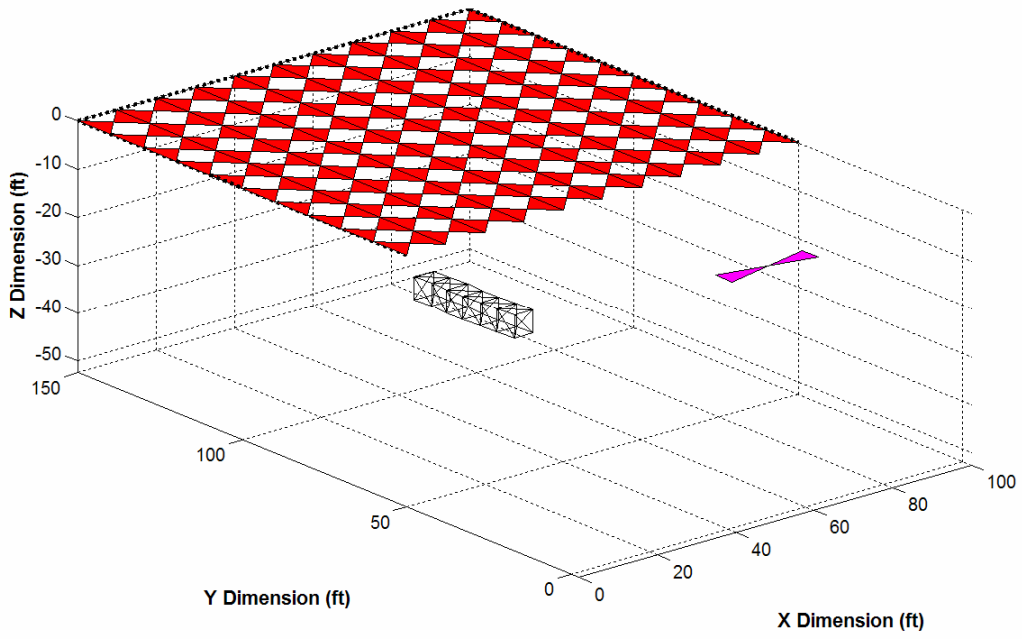

Figure 6.10 Air-filled target asymmetric with respect to transmitter and receiver at 1 MHz

Transmitter:
Location: 50’ x 0’ x 0’
Power: 10 W
Frequency: 1 MHz

Receiver:
Location: 50’ x 100’ x 0’
Size: 100’ x 100’
Spacing: 10’ x 10’

Target:
Location: 80’ x 125’ x -50’
Size: 5’ x ~30’ x 5’
Air Filled
BRDF Roughness Factor: 0.5
BRDF Isotropy Factor: 0.5

Ground:
Permittivity: 14
Permeability: 1
Conductivity: 2 mS/m

In this scenario, Figure 6.10 depicts an air-filled target placed asymmetrically with respect to the transmitting and receiving antennas. The target is buried 50 ft. below the Earth's surface parallel to the Y dimension in an assumed homogeneous medium with dielectric permittivity of 14, permeability of 1, and conductivity of 2 mS/m. This medium is characteristic of a fine rocky soil. The transmitting antenna transmits 10 W of power at a frequency of 1 MHz. Solid Works allowed the definition of 52 distinct target facets each with an approximate surface area of 1.125 m^2 (12.5 ft^2) and center separation of 1.5 m to satisfy the SAR system resolution requirement. MATLAB 3D interpolation function *griddata3* was used to map the integrated return power acquired for each target facet to its appropriate location in the GPR scene.

The 3D image produced in Figure 6.11 portrays the true target's size and orientation. The intersection between the 3D approximation and the true target is attributed to recorded power return from target facets other than the surface. Since return power consisted of ITI, STI, and FTI reflections, energy from different vantage points was available during the MATLAB interpolation. In the 2D image, shown in Figure 6.12, due to the location and orientation of the target, a greater intensity of return power is seen at the portion of the target closest to the transmitting antenna than at the opposing end. Nearly all of the power in the spectral direction is lost, however, the intensities in the image are represented by the diffuse reflections. The limitations in the interpolation scheme and scaling hinder the target dimension accuracy in the generated images. The total detectable power reflected by the target is calculated as 31.7865 mW (0.31%). At the low end of the range of frequencies considered in this simulation [1 MHz – 10 MHz], this is determined to be the greatest amount of power that can be received.

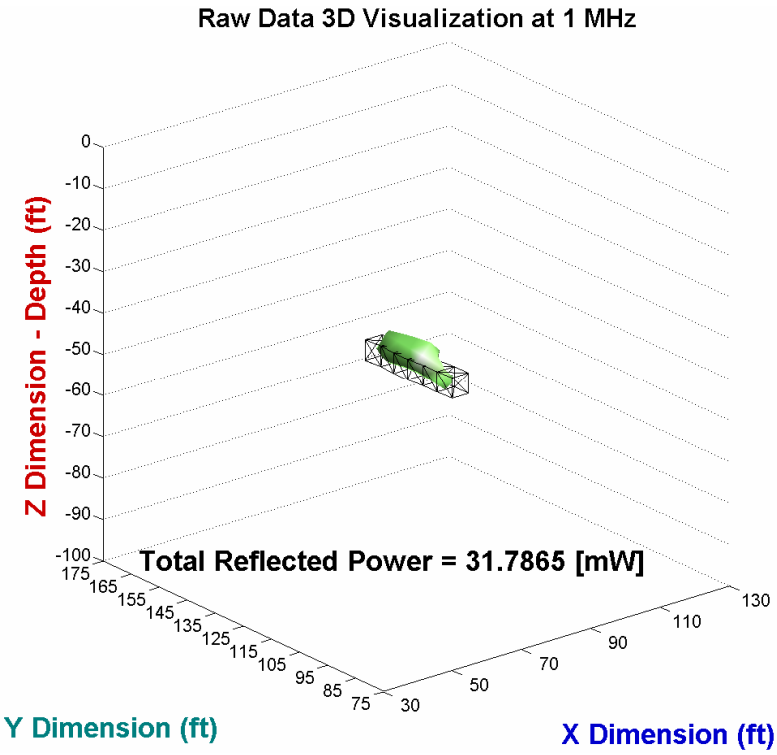

Figure 6.11 3D interpolation of radar return for air-filled target asymmetric with respect to transmitter and receiver at 1 MHz

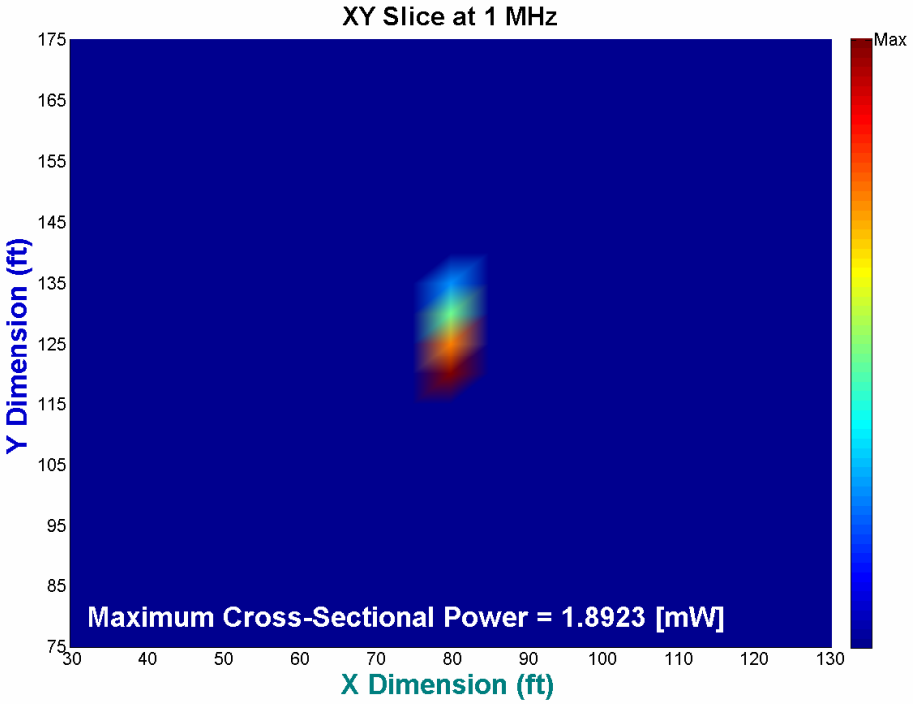

Figure 6.12 2D image of air-filled target asymmetric with respect to transmitter and receiver at 1 MHz

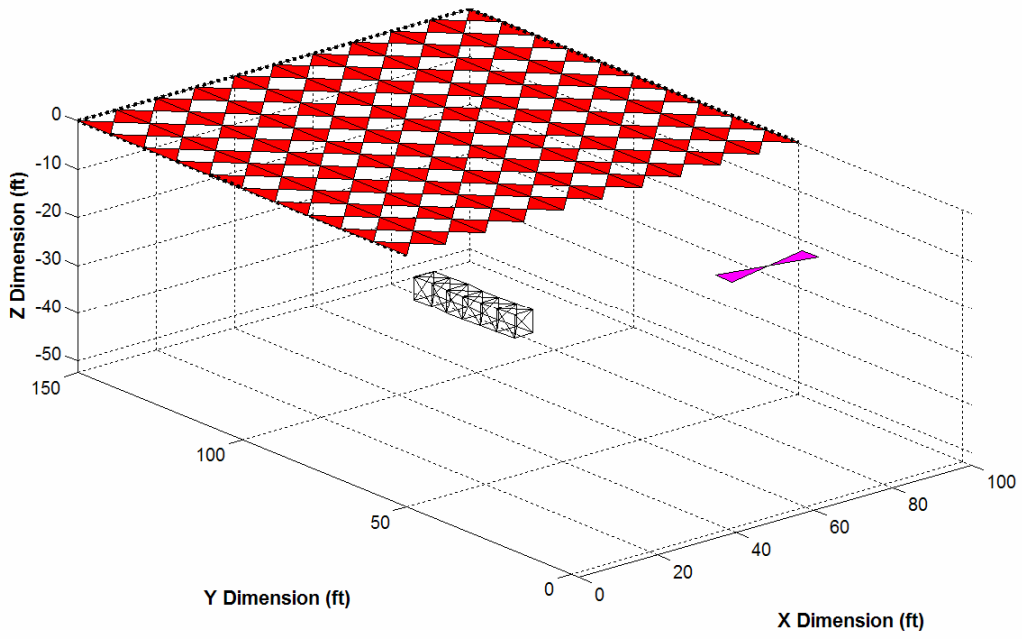

Figure 6.13 Air-filled target asymmetric with respect to transmitter and receiver at 5 MHz

Transmitter:
Location: 50’ x 0’ x 0’
Power: 10 W
Frequency: 5 MHz

Receiver:
Location: 50’ x 100’ x 0’
Size: 100’ x 100’
Spacing: 10’ x 10’

Target:
Location: 80’ x 125’ x -50’
Size: 5’ x ~30’ x 5’
Air Filled
BRDF Roughness Factor: 0.5
BRDF Isotropy Factor: 0.5

Ground:
Permittivity: 14
Permeability: 1
Conductivity: 2 mS/m

In this scenario, Figure 6.13 depicts an air-filled target placed asymmetrically with respect to the transmitting and receiving antennas. The target is buried 50 ft. below the Earth's surface parallel to the Y dimension in an assumed homogeneous medium with dielectric permittivity of 14, permeability of 1, and conductivity of 2 mS/m. This medium is characteristic of a fine rocky soil. The transmitting antenna transmits 10 W of power at a frequency of 5 MHz. Solid Works allowed the definition of 52 distinct target facets each with an approximate surface area of 1.125 m^2 (12.5 ft^2) and center separation of 1.5 m to satisfy the SAR system resolution requirement. MATLAB 3D interpolation function *griddata3* was used to map the integrated return power acquired for each target facet to its appropriate location in the GPR scene.

The 3D image in Figure 6.14 portrays the true target's size and orientation. Since return power consisted of ITI, STI, and FTI reflections, energy from different vantage points was available during the MATLAB interpolation. The lack of representation towards the back end of the target is attributed to low power return relative to the rest of the integrated power at the front end. In the 2D image, shown in Figure 6.15, due to the location and orientation of the target, a greater intensity of return power is seen at the portion of the target closest to the transmitting antenna than at the opposing end. Nearly all of the power in the spectral direction is lost, however, the intensities in the image are represented by the diffuse reflections. The limitations in the interpolation scheme and scaling hinder the target dimension accuracy in the generated images. The total detectable power reflected by the target is calculated as 11.0444 mW (0.11%). At the midpoint of the range of frequencies considered in this simulation [1 MHz – 10 MHz], this is determined to be the average amount of power that can be received.

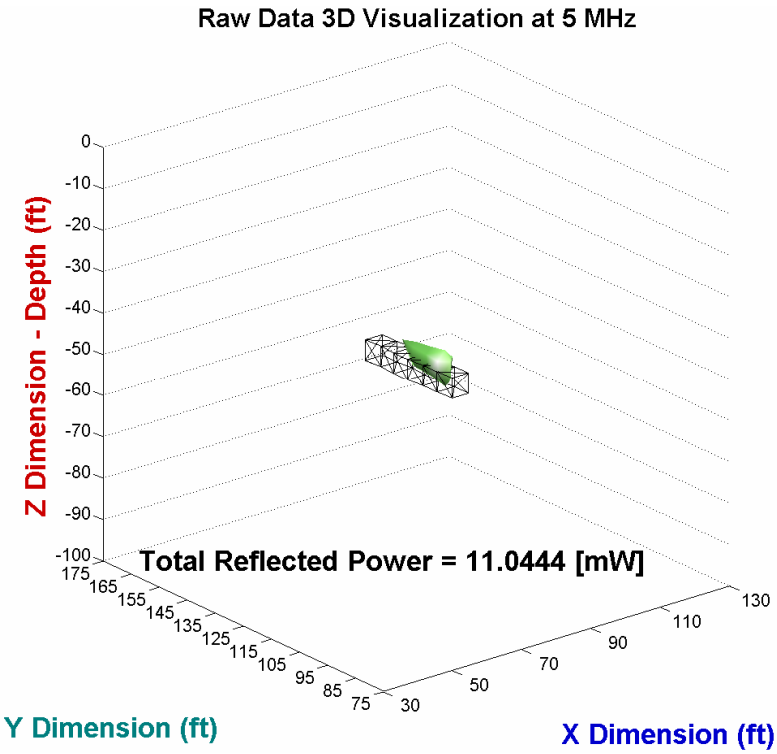

Figure 6.14 3D interpolation of radar return for air-filled target asymmetric with respect to transmitter and receiver at 5 MHz

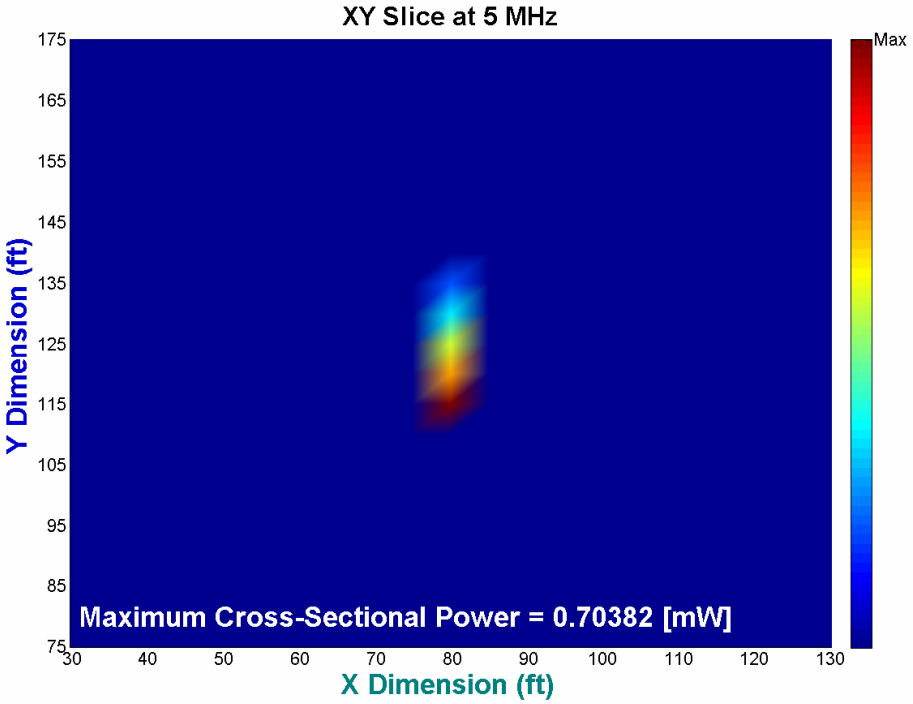

Figure 6.15 2D image of air-filled target asymmetric with respect to transmitter and receiver at 5 MHz

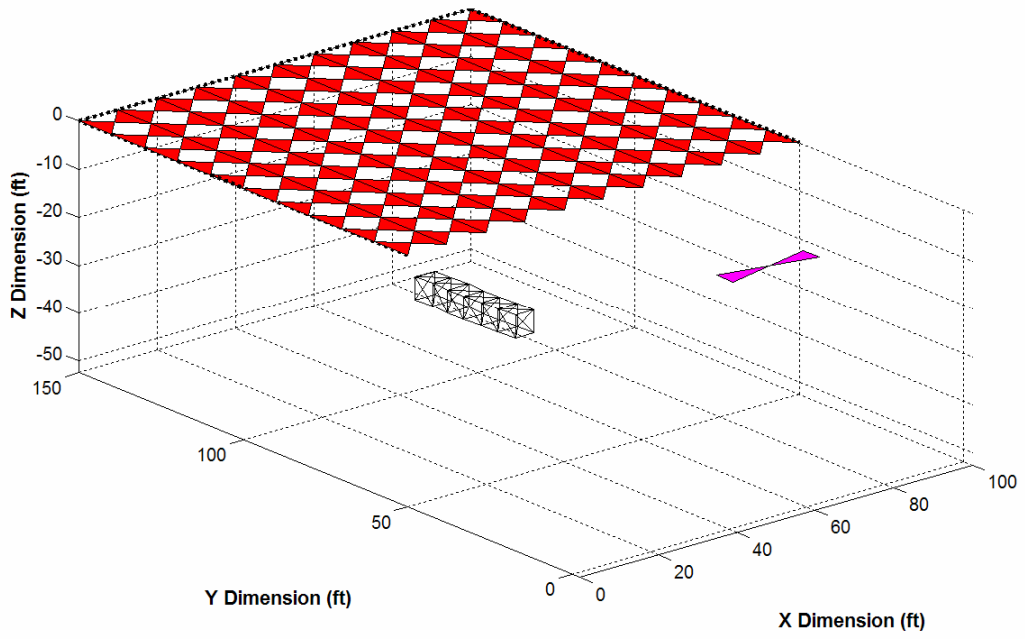

Figure 6.16 Air-filled target asymmetric with respect to transmitter and receiver at 10 MHz

Transmitter:
Location: 50’ x 0’ x 0’
Power: 10 W
Frequency: 10 MHz

Receiver:
Location: 50’ x 100’ x 0’
Size: 100’ x 100’
Spacing: 10’ x 10’

Target:
Location: 80’ x 125’ x -50’
Size: 5’ x ~30’ x 5’
Air Filled
BRDF Roughness Factor: 0.5
BRDF Isotropy Factor: 0.5

Ground:
Permittivity: 14
Permeability: 1
Conductivity: 2 mS/m

In this scenario, Figure 6.16 depicts an air-filled target placed asymmetrically with respect to the transmitting and receiving antennas. The target is buried 50 ft. below the Earth's surface parallel to the Y dimension in an assumed homogeneous medium with dielectric permittivity of 14, permeability of 1, and conductivity of 2 mS/m. This medium is characteristic of a fine rocky soil. The transmitting antenna transmits 10 W of power at a frequency of 10 MHz. Solid Works allowed the definition of 52 distinct target facets each with an approximate surface area of 1.125 m^2 (12.5 ft^2) and center separation of 1.5 m to satisfy the SAR system resolution requirement. MATLAB 3D interpolation function *griddata3* was used to map the integrated return power acquired for each target facet to its appropriate location in the GPR scene.

The 3D image in Figure 6.17 portrays the true target's size and orientation. Since return power consisted of ITI, STI, and FTI reflections, energy from different vantage points was available during the MATLAB interpolation. The lack of representation towards the back end of the target is attributed to low power return relative to the rest of the integrated power at the front end. In the 2D image, shown in Figure 6.18, due to the location and orientation of the target, a greater intensity of return power is seen at the portion of the target closest to the transmitting antenna than at the opposing end. Nearly all of the power in the spectral direction is lost, however, the intensities in the image are represented by the diffuse reflections. The limitations in the interpolation scheme and scaling hinder the target dimension accuracy in the generated images. The total detectable power reflected by the target is calculated as 10.046 mW (0.1%). At the high end of the range of frequencies considered in this simulation [1 MHz – 10 MHz], this is determined to be the least amount of power that can be received.

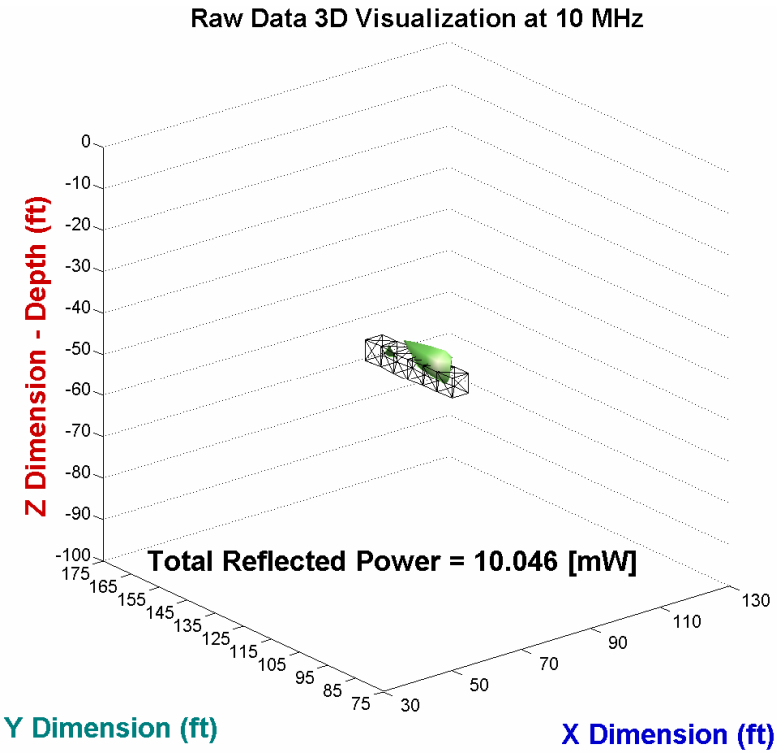

Figure 6.17 3D interpolation of radar return for air-filled target asymmetric with respect to transmitter and receiver at 10 MHz

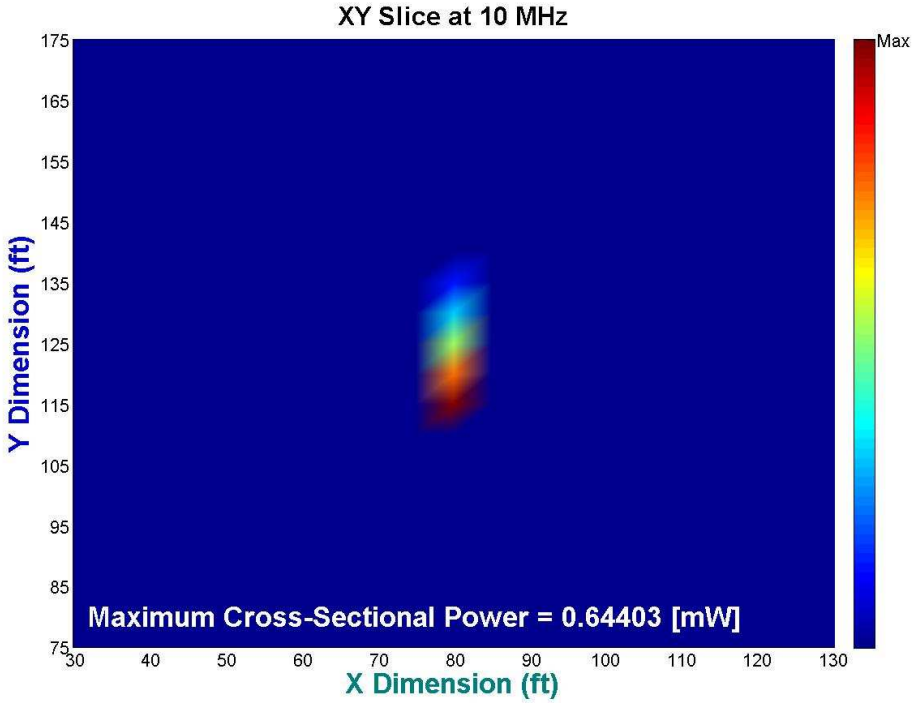

Figure 6.18 2D image of air-filled target asymmetric with respect to transmitter and receiver at 10 MHz

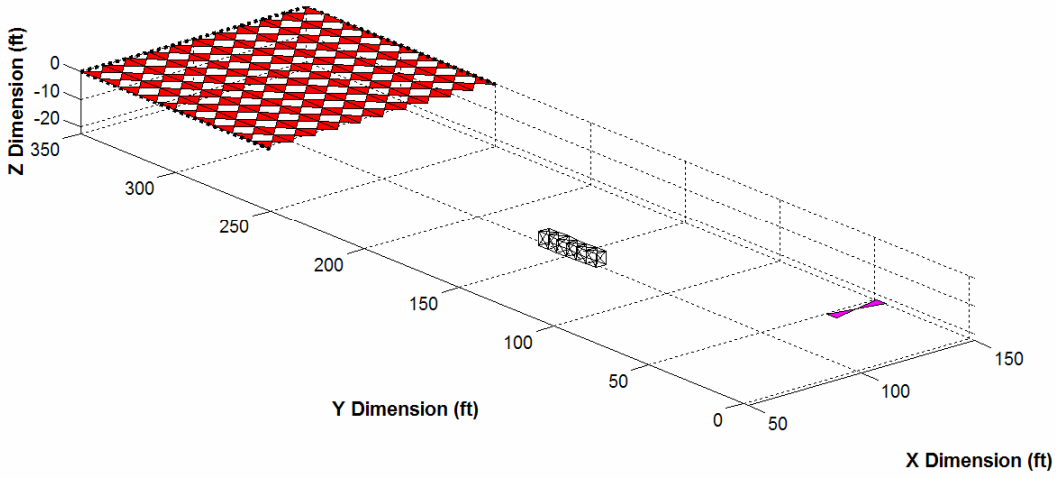

Figure 6.19 Air-filled target symmetric with respect to transmitter and receiver at a depth of 20 ft.

Transmitter:
Location: 100’ x 0’ x 0’
Power: 10 W
Frequency: 1 MHz

Receiver:
Location: 100’ x 300’ x 0’
Size: 100’ x 100’
Spacing: 10’ x 10’

Target:
Location: 100’ x 150’ x -20’
Size: 5’ x ~30’ x 5’
Air Filled
BRDF Roughness Factor: 0.5
BRDF Isotropy Factor: 0.5

Ground:
Permittivity: 14
Permeability: 1
Conductivity: 2 mS/m

In this scenario, Figure 6.19 depicts an air-filled target placed symmetrically between the transmitting and receiving antennas. The target is buried 20 ft. below the Earth's surface parallel to the Y dimension in an assumed homogeneous medium with dielectric permittivity of 14, permeability of 1, and conductivity of 2 mS/m. This medium is characteristic of a fine rocky soil. The transmitting antenna transmits 10 W of power at a frequency of 1 MHz. Solid Works allowed the definition of 52 distinct target facets each with an approximate surface area of 1.125 m^2 (12.5 ft^2) and center separation of 1.5 m to satisfy the SAR system resolution requirement. MATLAB 3D interpolation function *griddata3* was used to map the integrated return power acquired for each target facet to its appropriate location in the GPR scene.

The 3D image produced in Figure 6.20 portrays the true target's size and orientation. The vertical offset in the 3D approximation is attributed to the lack of power return from the bottom of the target. Since all the return power consisted of ITI reflections, only energy from the surface of the target was available. MATLAB interpolation limits the target representation in the Z dimension. In the 2D image, shown in Figure 6.21, due to the location of the target, a majority of the energy reflected in the spectral direction from the target end closest to the transmitter is received by the center of the receiver array. All remaining spectral reflections from the remainder of the target are lost. Diffuse reflections are indicated by the lower intensity hue at the back end of the image. The total detectable power reflected by the target is calculated as 32.4328 mW (0.32%). Considering attenuation from transmitter to target to receiver, this is determined to be the greatest amount of power that can be received at this depth.

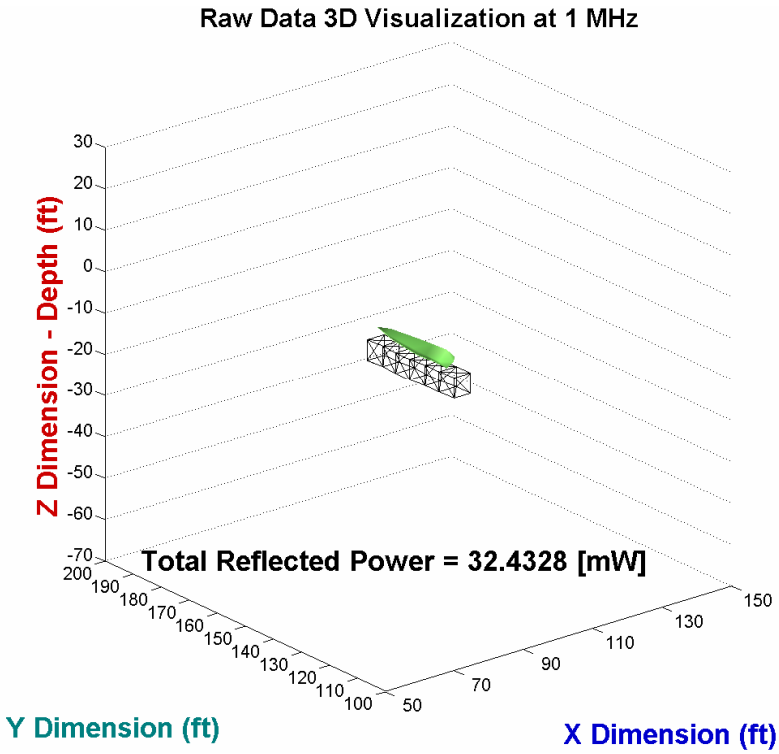

Figure 6.20 3D interpolation of radar return for air-filled target symmetric with respect to transmitter and receiver at a depth of 20 ft.

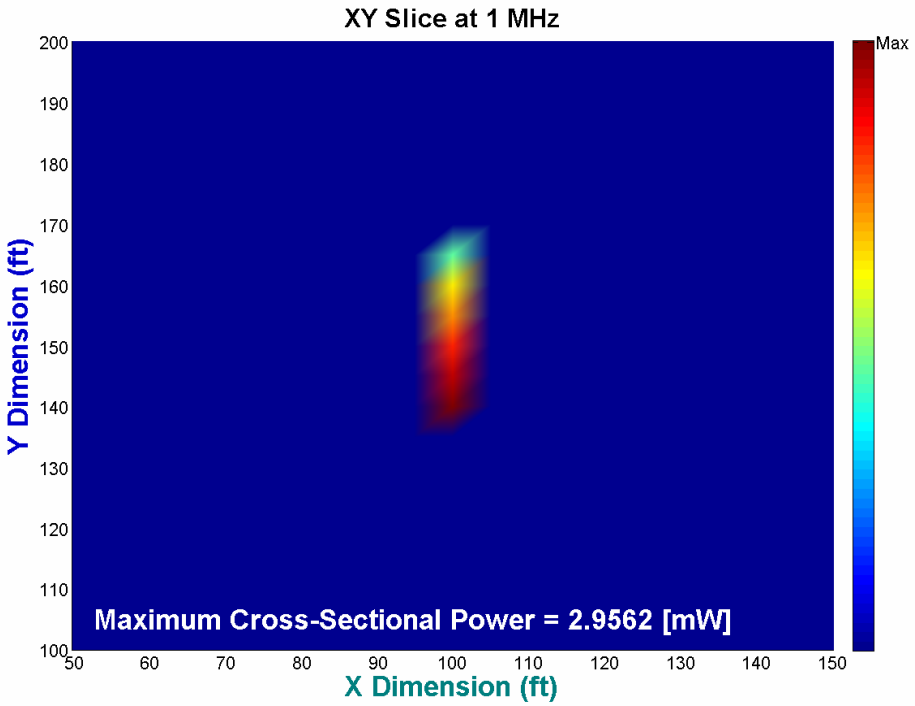

Figure 6.21 2D image of air-filled target symmetric with respect to transmitter and receiver at a depth of 20 ft.

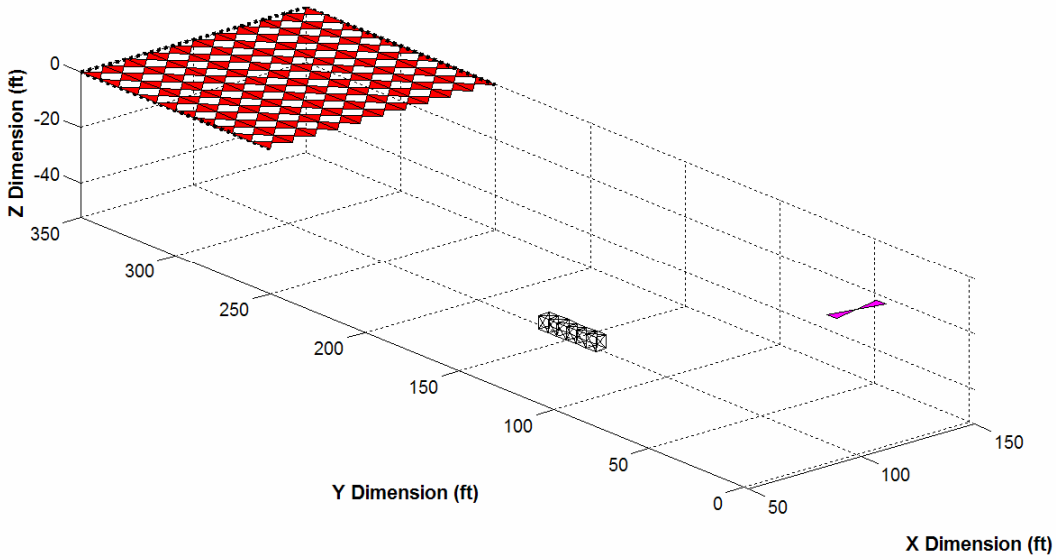

Figure 6.22 Air-filled target symmetric with respect to transmitter and receiver at a depth of 50 ft.

Transmitter:
Location: 100’ x 0’ x 0’
Power: 10 W
Frequency: 1 MHz

Receiver:
Location: 100’ x 300’ x 0’
Size: 100’ x 100’
Spacing: 10’ x 10’

Target:
Location: 100’ x 150’ x -50’
Size: 5’ x ~30’ x 5’
Air Filled
BRDF Roughness Factor: 0.5
BRDF Isotropy Factor: 0.5

Ground:
Permittivity: 14
Permeability: 1
Conductivity: 2 mS/m

In this scenario, Figure 6.22 depicts an air-filled target placed symmetrically between the transmitting and receiving antennas. The target is buried 50 ft. below the Earth's surface parallel to the Y dimension in an assumed homogeneous medium with dielectric permittivity of 14, permeability of 1, and conductivity of 2 mS/m. This medium is characteristic of a fine rocky soil. The transmitting antenna transmits 10 W of power at a frequency of 1 MHz. Solid Works allowed the definition of 52 distinct target facets each with an approximate surface area of 1.125 m^2 (12.5 ft^2) and center separation of 1.5 m to satisfy the SAR system resolution requirement. MATLAB 3D interpolation function *griddata3* was used to map the integrated return power acquired for each target facet to its appropriate location in the GPR scene.

The 3D image produced in Figure 6.23 portrays the true target's size and orientation. The intersection between the 3D approximation and the true target is attributed to return power from ITI, STI, and FTI reflections. This provides multiple vantage points beyond the surface of the target used by the MATLAB interpolation feature. In the 2D image, shown in Figure 6.24, due to the location of the target, a majority of the energy reflected in the spectral direction from the target end closest to the transmitter is received by the center of the receiver array. All remaining spectral reflections from the remainder of the target are lost. Diffuse reflections are indicated by the lower intensity hue at the back end of the image. The total detectable power reflected by the target is calculated as 9.5364 mW (0.09%). As the depth of the target increases, attenuation from transmitter to target to receiver increases accordingly and exponentially affects the received power.

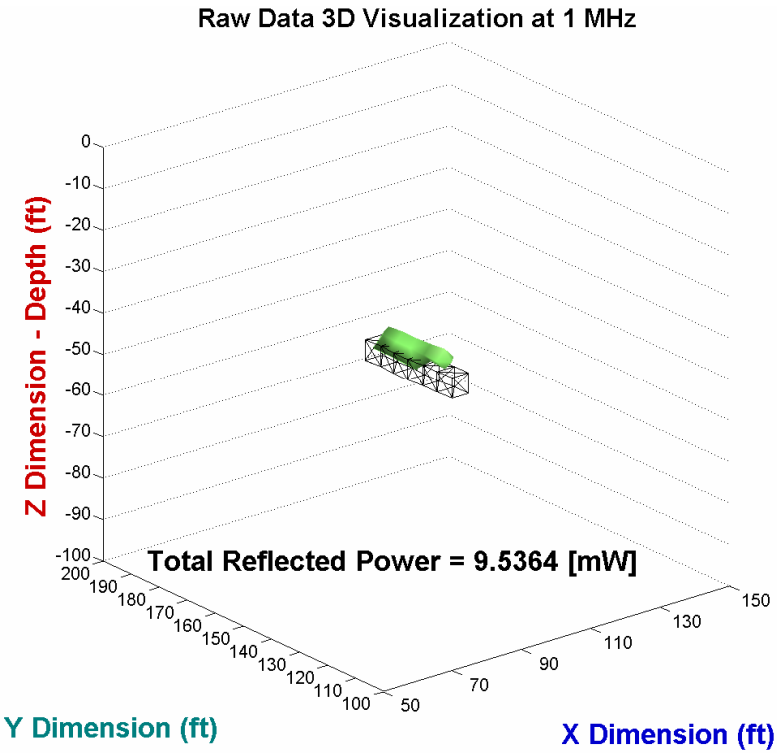

Figure 6.23 3D interpolation of radar return for air-filled target symmetric with respect to transmitter and receiver at a depth of 50 ft.

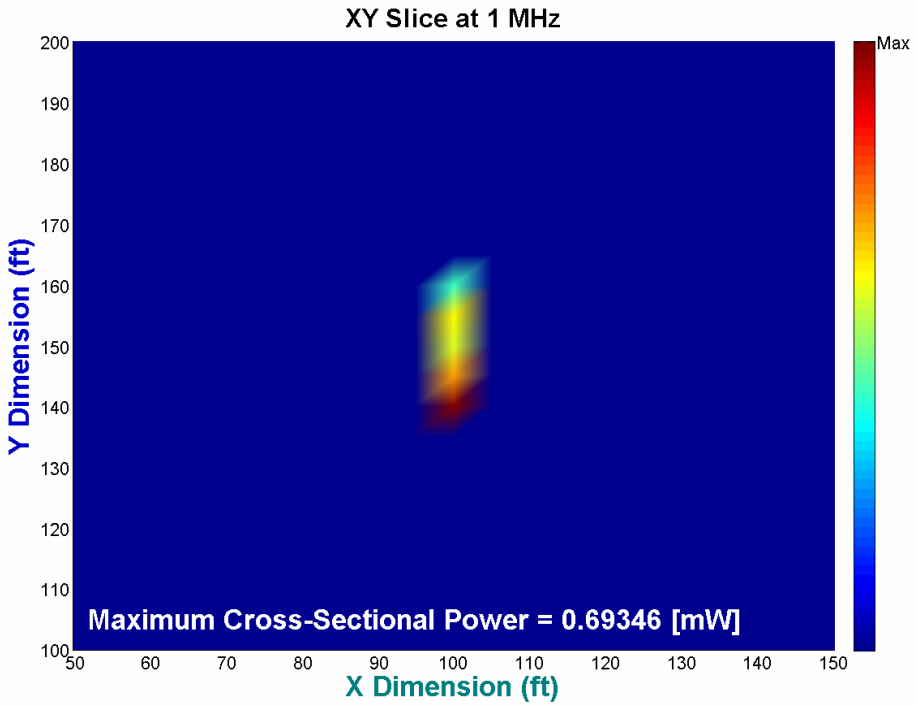

Figure 6.24 2D image of air-filled target symmetric with respect to transmitter and receiver at a depth of 50 ft.

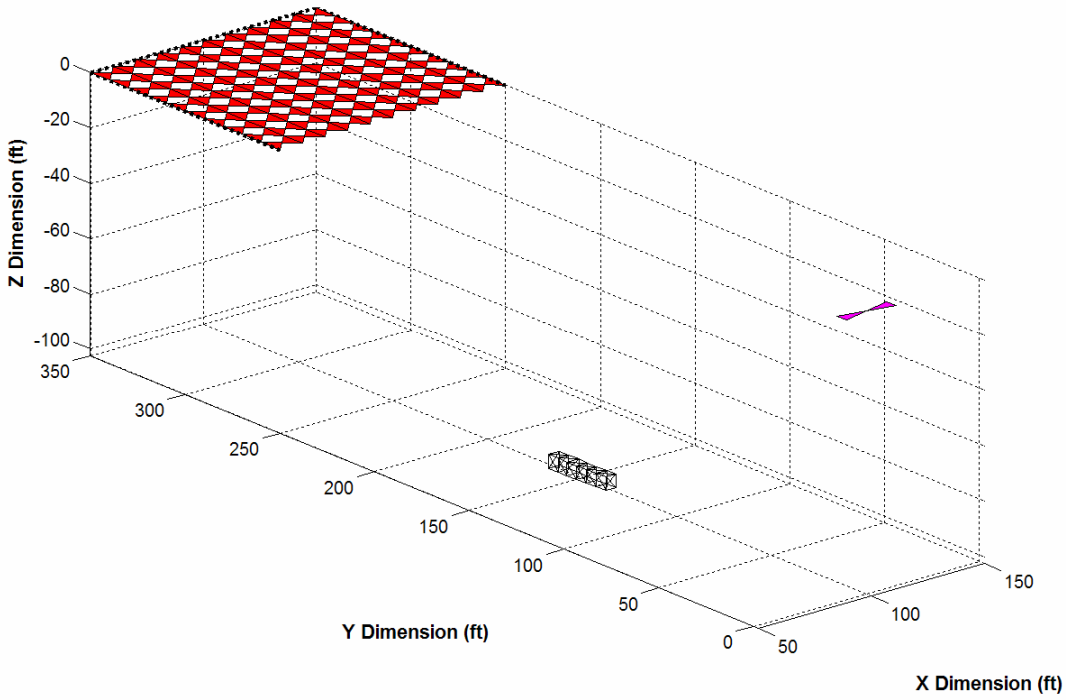

Figure 6.25 Air-filled target symmetric with respect to transmitter and receiver at a depth of 100 ft.

Transmitter:

Location: 100’ x 0’ x 0’
Power: 10 W
Frequency: 1 MHz

Receiver:

Location: 100’ x 300’ x 0’
Size: 100’ x 100’
Spacing: 10’ x 10’

Target:

Location: 100’ x 150’ x -100’
Size: 5’ x ~30’ x 5’
Air Filled
BRDF Roughness Factor: 0.5
BRDF Isotropy Factor: 0.5

Ground:

Permittivity: 14
Permeability: 1
Conductivity: 2 mS/m

In this scenario, Figure 6.25 depicts an air-filled target placed symmetrically between the transmitting and receiving antennas. The target is buried 100 ft. below the Earth's surface parallel to the Y dimension in an assumed homogeneous medium with dielectric permittivity of 14, permeability of 1, and conductivity of 2 mS/m. This medium is characteristic of a fine rocky soil. The transmitting antenna transmits 10 W of power at a frequency of 1 MHz. Solid Works allowed the definition of 52 distinct target facets each with an approximate surface area of 1.125 m^2 (12.5 ft^2) and center separation of 1.5 m to satisfy the SAR system resolution requirement. MATLAB 3D interpolation function *griddata3* was used to map the integrated return power acquired for each target facet to its appropriate location in the GPR scene.

The 3D image produced in Figure 6.26 portrays the true target's size and orientation. The vertical offset in the 3D approximation is attributed to the lack of power return from the bottom of the target. Since all the return power consisted of ITI reflections, only energy from the surface of the target was available. MATLAB interpolation limits the target representation in the Z dimension. In the 2D image, shown in Figure 6.27, due to the location of the target, a majority of the energy reflected in the spectral direction from the target end closest to the transmitter is received by the center of the receiver array. All remaining spectral reflections from the remainder of the target are lost. Diffuse reflections are indicated by the lower intensity hue at the back end of the image. The total detectable power reflected by the target is calculated as 1.4497 mW (0.014%). As the depth of the target increases, attenuation from transmitter to target to receiver increases accordingly and exponentially affects the received power.

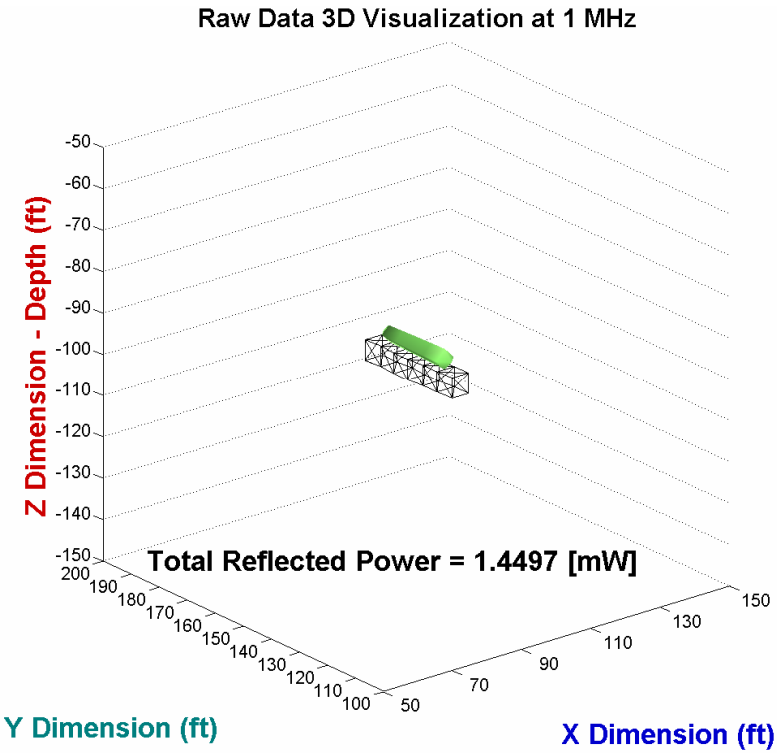

Figure 6.26 3D interpolation of radar return for air-filled target symmetric with respect to transmitter and receiver at a depth of 100 ft.

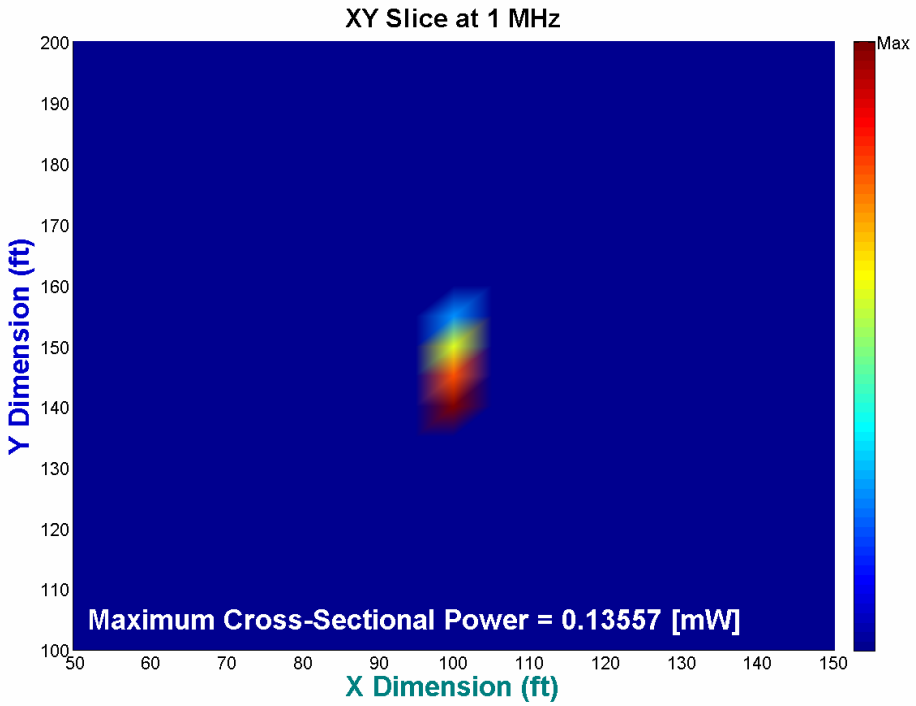

Figure 6.27 2D image of air-filled target symmetric with respect to transmitter and receiver at a depth of 100 ft.

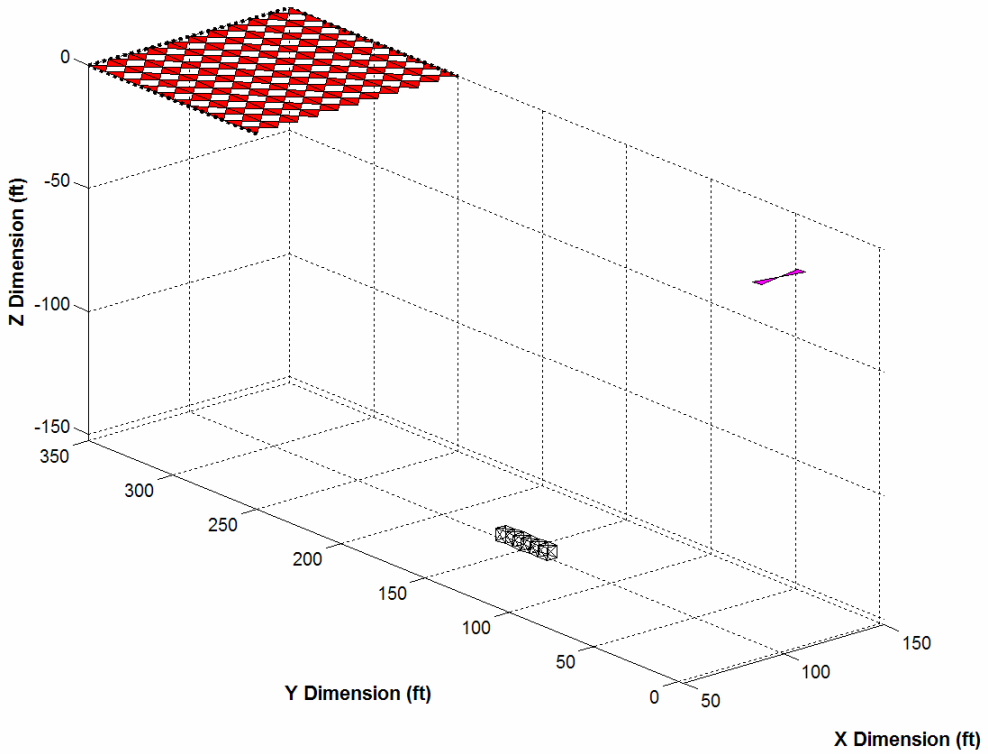

Figure 6.28 Air-filled target symmetric with respect to transmitter and receiver at a depth of 150 ft.

Transmitter:
Location: 100’ x 0’ x 0’
Power: 10 W
Frequency: 1 MHz

Receiver:
Location: 100’ x 300’ x 0’
Size: 100’ x 100’
Spacing: 10’ x 10’

Target:
Location: 100’ x 150’ x -150’
Size: 5’ x ~30’ x 5’
Air Filled
BRDF Roughness Factor: 0.5
BRDF Isotropy Factor: 0.5

Ground:
Permittivity: 14
Permeability: 1
Conductivity: 2 mS/m

In this scenario, Figure 6.28 depicts an air-filled target placed symmetrically between the transmitting and receiving antennas. The target is buried 150 ft. below the Earth's surface parallel to the Y dimension in an assumed homogeneous medium with dielectric permittivity of 14, permeability of 1, and conductivity of 2 mS/m. This medium is characteristic of a fine rocky soil. The transmitting antenna transmits 10 W of power at a frequency of 1 MHz. Solid Works allowed the definition of 52 distinct target facets each with an approximate surface area of 1.125 m^2 (12.5 ft^2) and center separation of 1.5 m to satisfy the SAR system resolution requirement. MATLAB 3D interpolation function *griddata3* was used to map the integrated return power acquired for each target facet to its appropriate location in the GPR scene.

The 3D image produced in Figure 6.29 portrays the true target's size and orientation. The vertical offset in the 3D approximation is attributed to the lack of power return from the bottom of the target. Since all the return power consisted of ITI reflections, only energy from the surface of the target was available. MATLAB interpolation limits the target representation in the Z dimension. In the 2D image, shown in Figure 6.30, due to the location of the target, a majority of the energy reflected in the spectral direction from the target end closest to the transmitter is received by the center of the receiver array. In both images, the minimal return along the Y dimension of the target is caused by insufficient power return during MATLAB interpolation. The total detectable power reflected by the target is calculated as 0.30235 mW (0.003%). As the depth of the target increases, attenuation from transmitter to target to receiver increases accordingly and exponentially affects the received power.

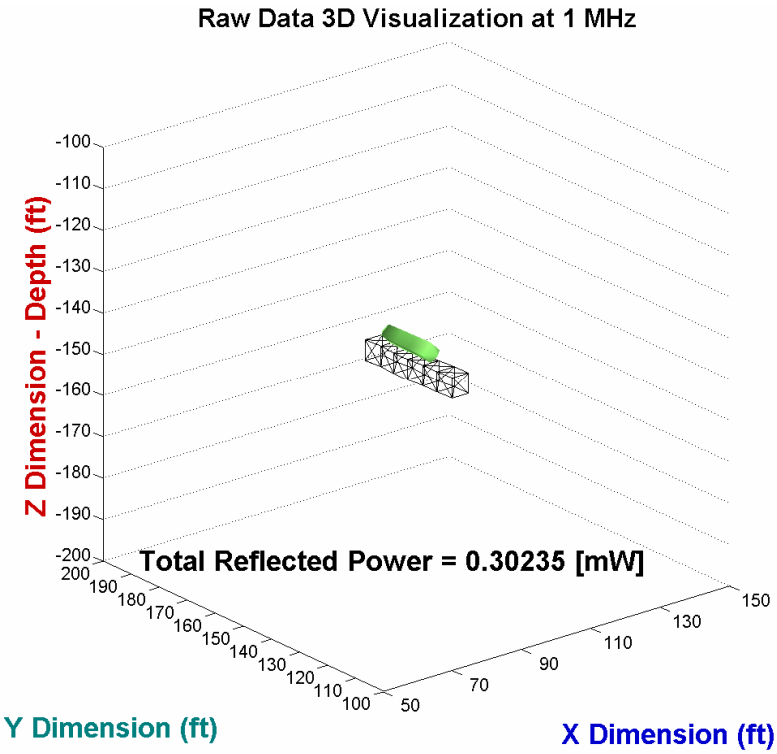

Figure 6.29 3D interpolation of radar return for air-filled target symmetric with respect to transmitter and receiver at a depth of 150 ft.

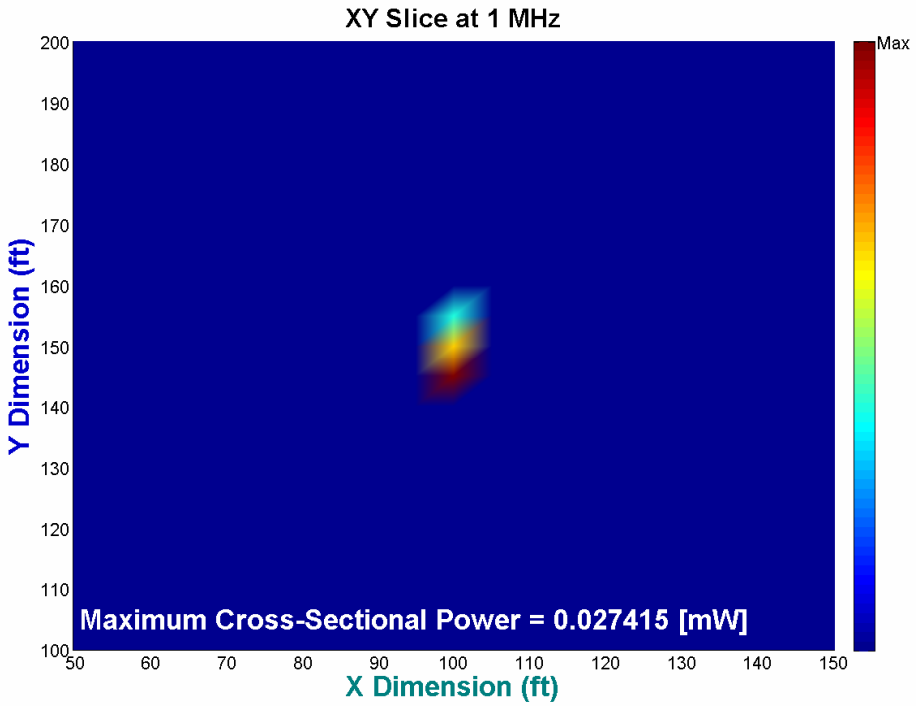

Figure 6.30 2D image of air-filled target symmetric with respect to transmitter and receiver at a depth of 150 ft.

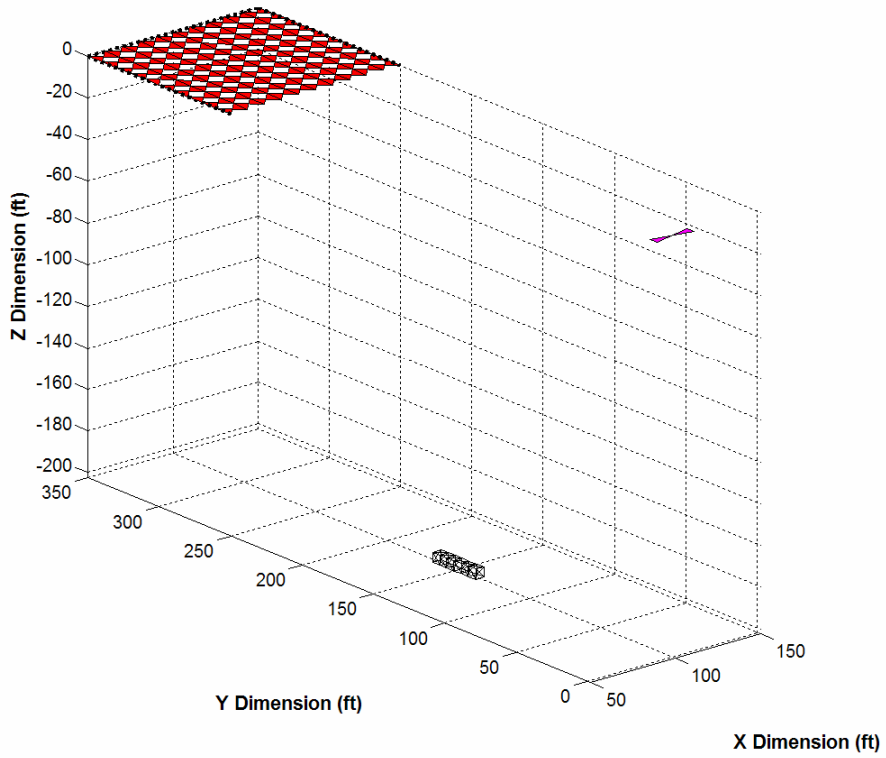

Figure 6.31 Air-filled target symmetric with respect to transmitter and receiver at a depth of 200 ft.

Transmitter:
Location: 100’ x 0’ x 0’
Power: 10 W
Frequency: 1 MHz

Receiver:
Location: 100’ x 300’ x 0’
Size: 100’ x 100’
Spacing: 10’ x 10’

Target:
Location: 100’ x 150’ x -200’
Size: 5’ x ~30’ x 5’
Air Filled
BRDF Roughness Factor: 0.5
BRDF Isotropy Factor: 0.5

Ground:
Permittivity: 14
Permeability: 1
Conductivity: 2 mS/m

In this scenario, Figure 6.31 depicts an air-filled target placed symmetrically between the transmitting and receiving antennas. The target is buried 200 ft. below the Earth's surface parallel to the Y dimension in an assumed homogeneous medium with dielectric permittivity of 14, permeability of 1, and conductivity of 2 mS/m. This medium is characteristic of a fine rocky soil. The transmitting antenna transmits 10 W of power at a frequency of 1 MHz. Solid Works allowed the definition of 52 distinct target facets each with an approximate surface area of 1.125 m^2 (12.5 ft^2) and center separation of 1.5 m to satisfy the SAR system resolution requirement. MATLAB 3D interpolation function *griddata3* was used to map the integrated return power acquired for each target facet to its appropriate location in the GPR scene.

The 3D image produced in Figure 6.32 portrays the true target's size and orientation. The vertical offset in the 3D approximation is attributed to the lack of power return from the bottom of the target. Since all the return power consisted of ITI reflections, only energy from the surface of the target was available. MATLAB interpolation limits the target representation in the Z dimension. In the 2D image, shown in Figure 6.33, due to the location of the target, a majority of the energy reflected in the spectral direction from the target end closest to the transmitter is received by the center of the receiver array. All remaining spectral reflections from the remainder of the target are lost. Diffuse reflections are indicated by the lower intensity hue at the back end of the image. The total detectable power reflected by the target is calculated 59.014 μW (0.0006%). As the depth of the target increases, attenuation from transmitter to target to receiver increases accordingly and exponentially affects the received power.

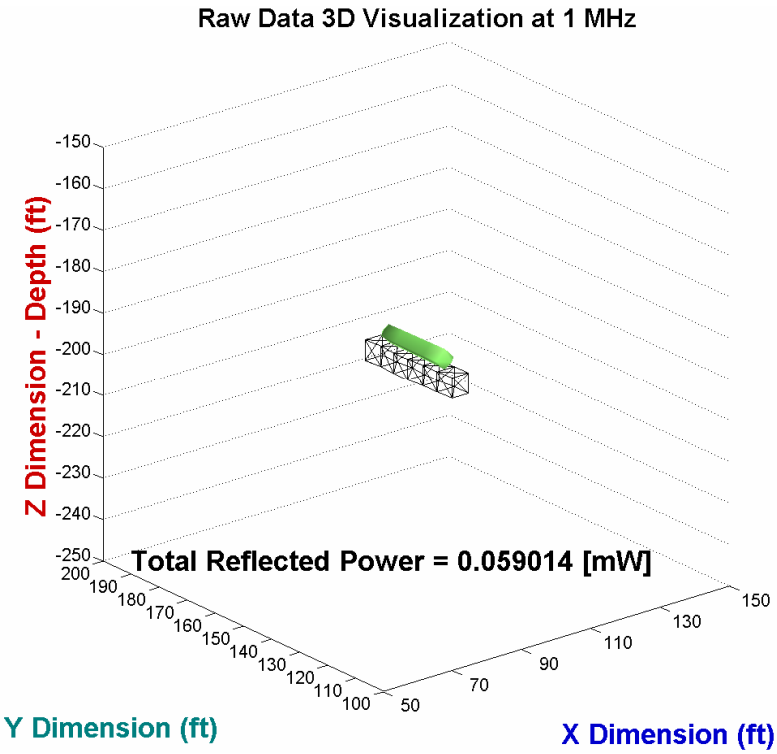

Figure 6.32 3D interpolation of radar return for air-filled target symmetric with respect to transmitter and receiver at a depth of 200 ft.

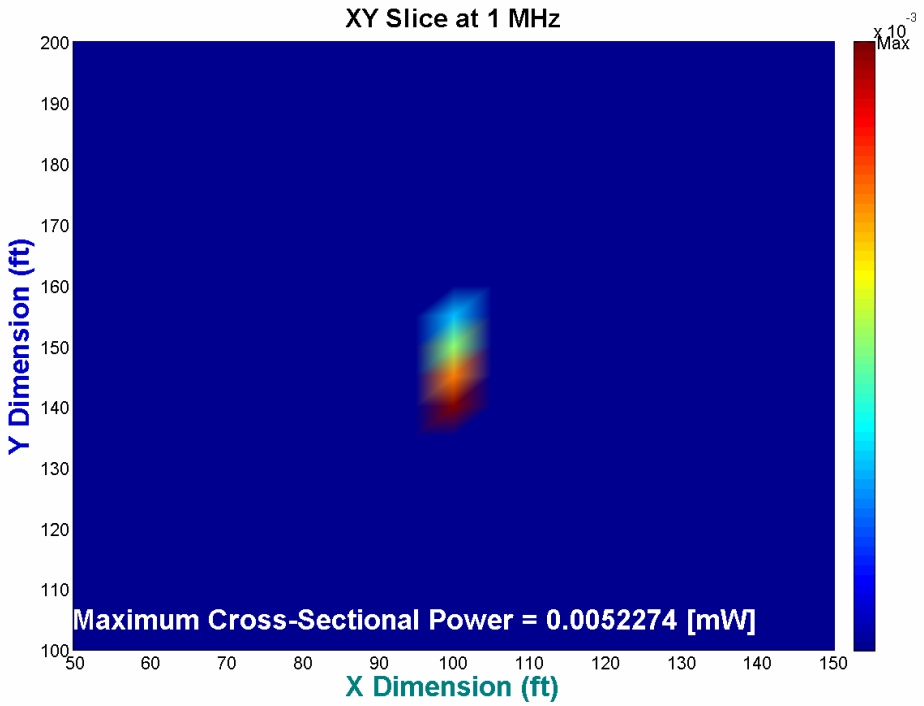

Figure 6.33 2D image of air-filled target symmetric with respect to transmitter and receiver at a depth of 200 ft.

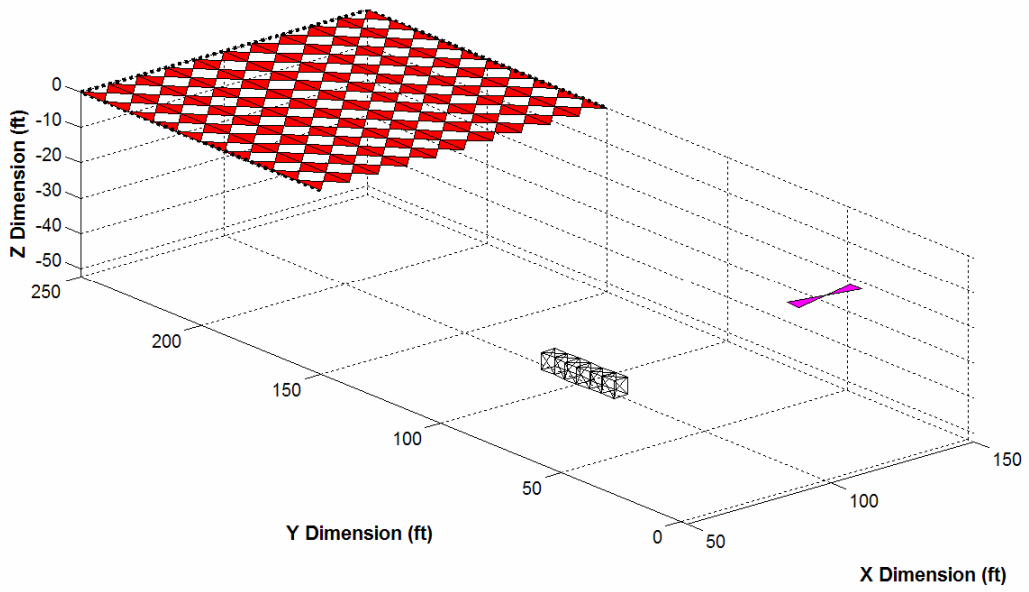

Figure 6.34 Air-filled target symmetric embedded in fine rocky soil

Transmitter:
Location: 100’ x 0’ x 0’
Power: 10 W
Frequency: 1MHz, 10 MHz

Receiver:
Location: 100’ x 200’ x 0’
Size: 100’ x 100’
Spacing: 10’ x 10’

Target:
Location: 100’ x 100’ x -50’
Size: 5’ x ~30’ x 5’
Air Filled
BRDF Roughness Factor: 0.5
BRDF Isotropy Factor: 0.5

Ground:
Permittivity: 14
Permeability: 1
Conductivity: 2 mS/m

In this scenario, Figure 6.34 depicts an air-filled target placed symmetrically between the transmitting and receiving antennas. The target is buried 50 ft. below the Earth's surface parallel to the Y dimension in an assumed homogeneous medium with dielectric permittivity of 14, permeability of 1, and conductivity of 2 mS/m. This medium is characteristic of a fine rocky soil. The transmitting antenna transmits 10 W of power at a frequency of 1 MHz and 10 MHz. Solid Works allowed the definition of 52 distinct target facets each with an approximate surface area of 1.125 m^2 (12.5 ft^2) and center separation of 1.5 m to satisfy the SAR system resolution requirement. MATLAB 3D interpolation function *griddata3* was used to map the integrated return power acquired for each target facet to its appropriate location in the GPR scene.

The 3D image produced in Figure 6.35 portrays the true target's size and orientation. The vertical offset in the 3D approximation is attributed to the lack of power return from the bottom of the target. Since all the return power consisted of ITI reflections, only energy from the surface of the target was available. MATLAB interpolation limits the target representation in the Z dimension. In the 2D image, shown in Figure 6.36, due to the location of the target, a majority of the energy reflected in the spectral direction from the target end closest to the transmitter is received by the center of the receiver array. All remaining spectral reflections from the remainder of the target are lost. Diffuse reflections are indicated by the lower intensity hue at the back end of the image. Based on the soil composition, specifically the conductivity of the soil, the effect of increasing the transmit frequency is a 70.96% decrease in received power.

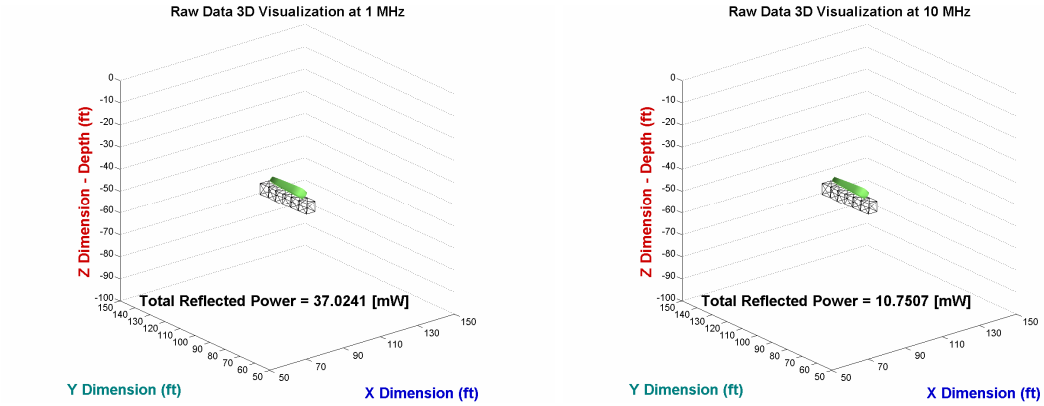

Figure 6.35 3D interpolation of radar return for air-filled target embedded in fine rocky soil at 1 MHz and 10 MHz

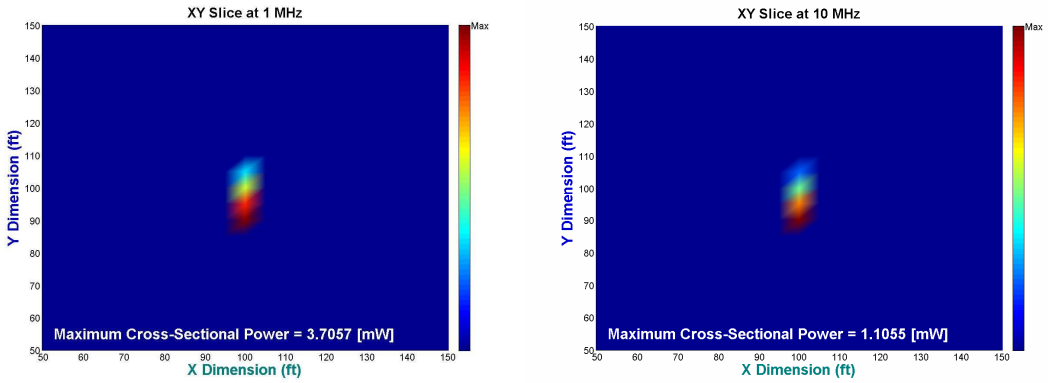

Figure 6.36 2D image of air-filled target embedded in fine rocky soil at 1 MHz and 10 MHz

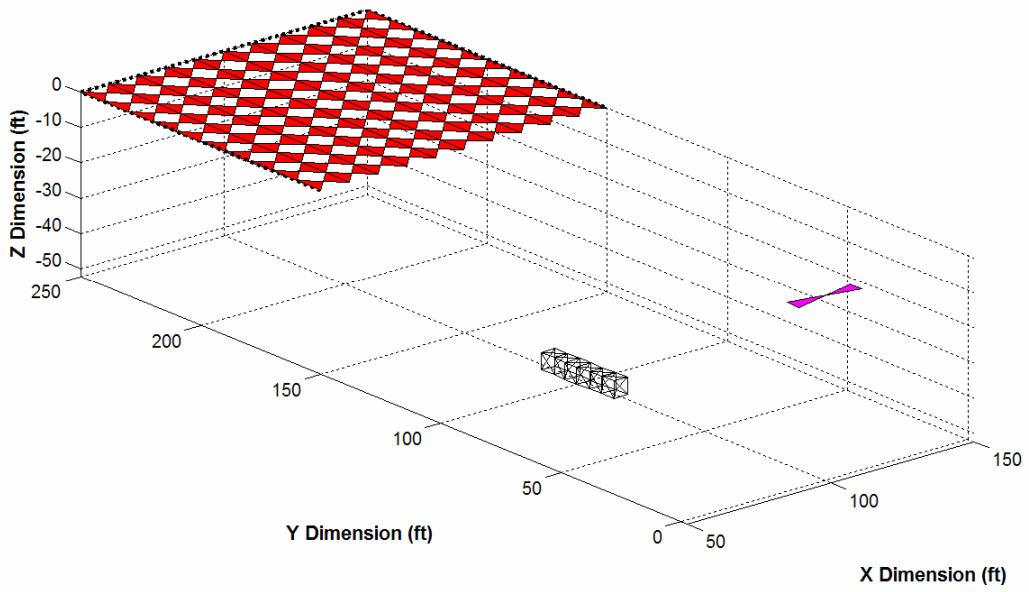

Figure 6.37 Air-filled target embedded in arid dessert sand

Transmitter:
Location: 100’ x 0’ x 0’
Power: 10 W
Frequency: 1MHz, 10 MHz

Receiver:
Location: 100’ x 200’ x 0’
Size: 100’ x 100’
Spacing: 10’ x 10’

Target:
Location: 100’ x 100’ x -50’
Size: 5’ x ~30’ x 5’
Air Filled
BRDF Roughness Factor: 0.5
BRDF Isotropy Factor: 0.5

Ground:
Permittivity: 3
Permeability: 1
Conductivity: 50 μS/m

In this scenario, Figure 6.37 depicts an air-filled target placed symmetrically between the transmitting and receiving antennas. The target is buried 50 ft. below the Earth's surface parallel to the Y dimension in an assumed homogeneous medium with dielectric permittivity of 3, permeability of 1, and conductivity of 50 μS/m. This medium is characteristic of a fine rocky soil. The transmitting antenna transmits 10 W of power at a frequency of 1 MHz and 10 MHz. Solid Works allowed the definition of 52 distinct target facets each with an approximate surface area of 1.125 m^2 (12.5 ft^2) and center separation of 1.5 m to satisfy the SAR system resolution requirement. MATLAB 3D interpolation function *griddata3* was used to map the integrated return power acquired for each target facet to its appropriate location in the GPR scene.

The 3D image produced in Figure 6.38 portrays the true target's size and orientation. The vertical offset in the 3D approximation is attributed to the lack of power return from the bottom of the target. Since all the return power consisted of ITI reflections, only energy from the surface of the target was available. MATLAB interpolation limits the target representation in the Z dimension. In the 2D image, shown in Figure 6.39, due to the location of the target, a majority of the energy reflected in the spectral direction from the target end closest to the transmitter is received by the center of the receiver array. All remaining spectral reflections from the remainder of the target are lost. Diffuse reflections are indicated by the lower intensity hue at the back end of the image. Based on the soil composition, specifically the conductivity of the soil, the effect of increasing the transmit frequency is a 0.28% decrease in received power.

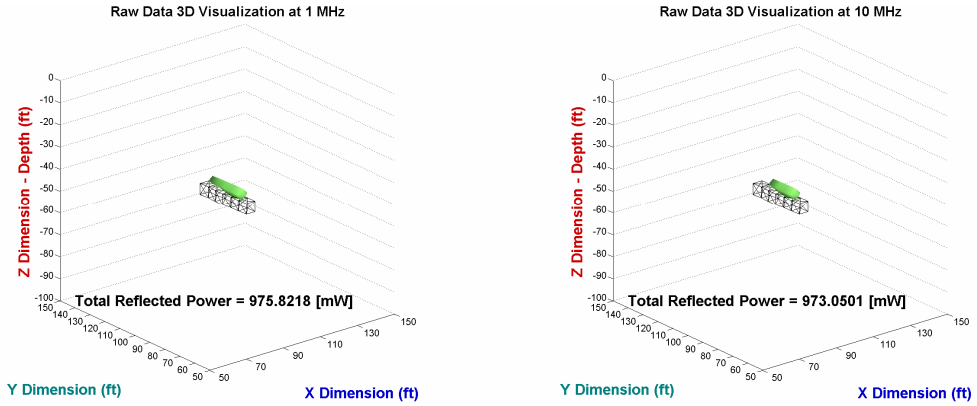

Figure 6.38 3D interpolation of radar return for air-filled target embedded in arid dessert sand at 1 MHz and 10 MHz

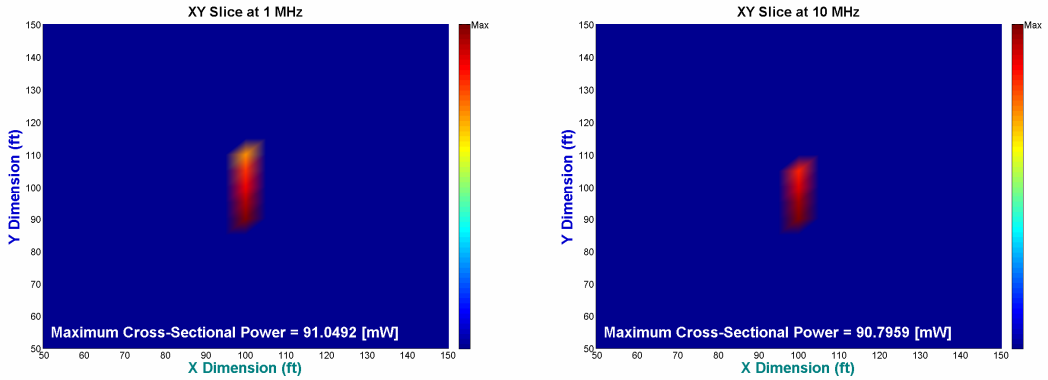

Figure 6.39 2D image of air-filled target embedded in arid dessert sand at 1 MHz and 10 MHz

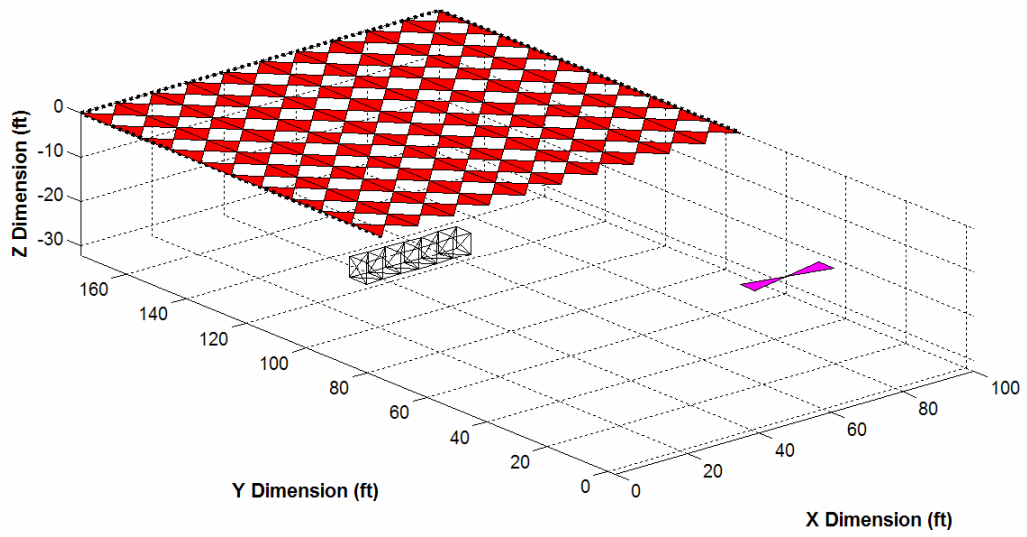

Figure 6.40 Air-filled target buried beneath receiver at a depth of 30 ft.

Transmitter:
Location: 50’ x 0’ x 0’
Power: 10 W
Frequency: 1MHz, 10 MHz

Receiver:
Location: 50’ x 125’ x 0’
Size: 100’ x 100’
Spacing: 10’ x 10’

Target:
Location: 50’ x 75’ x -30’
Size: 5’ x ~30’ x 5’
Air Filled
BRDF Roughness Factor: 0.5
BRDF Isotropy Factor: 0.5

Ground:
Permittivity: 14
Permeability: 1
Conductivity: 2 mS/m

In this scenario, Figure 6.40 depicts an air-filled target placed directly beneath the receiving antennas. The target is buried 30 ft. below the Earth's surface parallel to the X dimension in an assumed homogeneous medium with dielectric permittivity of 14, permeability of 1, and conductivity of 2 mS/m. This medium is characteristic of a fine rocky soil. The transmitting antenna transmits 10 W of power at a frequency of 1 MHz. Solid Works allowed the definition of 52 distinct target facets each with an approximate surface area of 1.125 m^2 (12.5 ft^2) and center separation of 1.5 m to satisfy the SAR system resolution requirement. MATLAB 3D interpolation function *griddata3* was used to map the integrated return power acquired for each target facet to its appropriate location in the GPR scene.

The 3D image produced in Figure 6.41 portrays the true target's size and orientation. While the true target was strategically placed to guarantee the occurrence of ITI, STI, and FTI reflections, the vertical offset present in the 3D approximation is attributed to the low power return from the bottom of the target. Although additional target facet locations were recorded as returning power, the strength of this power, relative to that returned from the surface of the target limited MATLAB interpolation of target representation in the Z dimension. In the 2D image, shown in Figure 6.42, due to the location of the target, a majority of the energy reflected in the spectral direction is lost. Diffuse reflections are indicated by the evenly distributed intensity across the image from left to right.

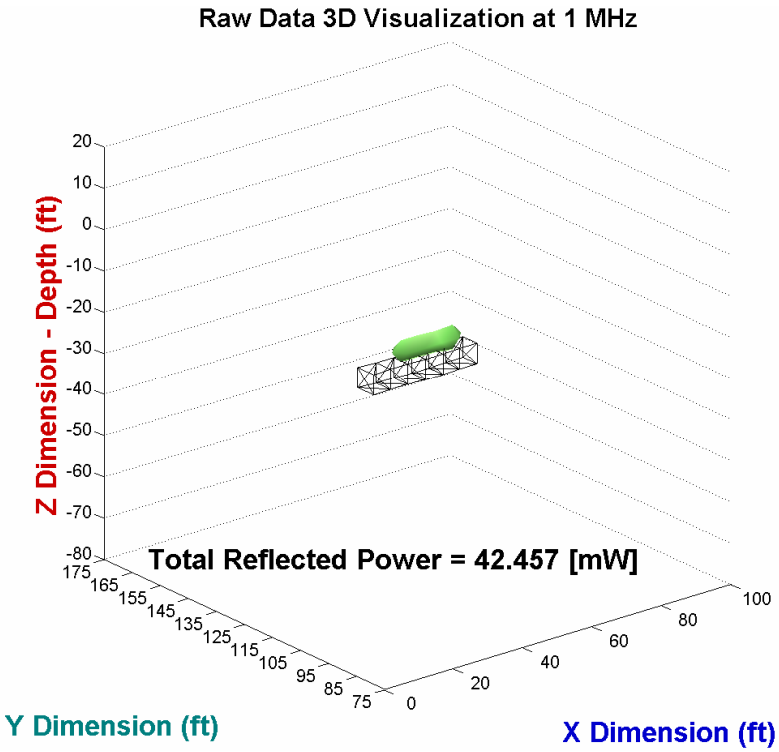

Figure 6.41 3D interpolation of radar return for air-filled target at 1 MHz

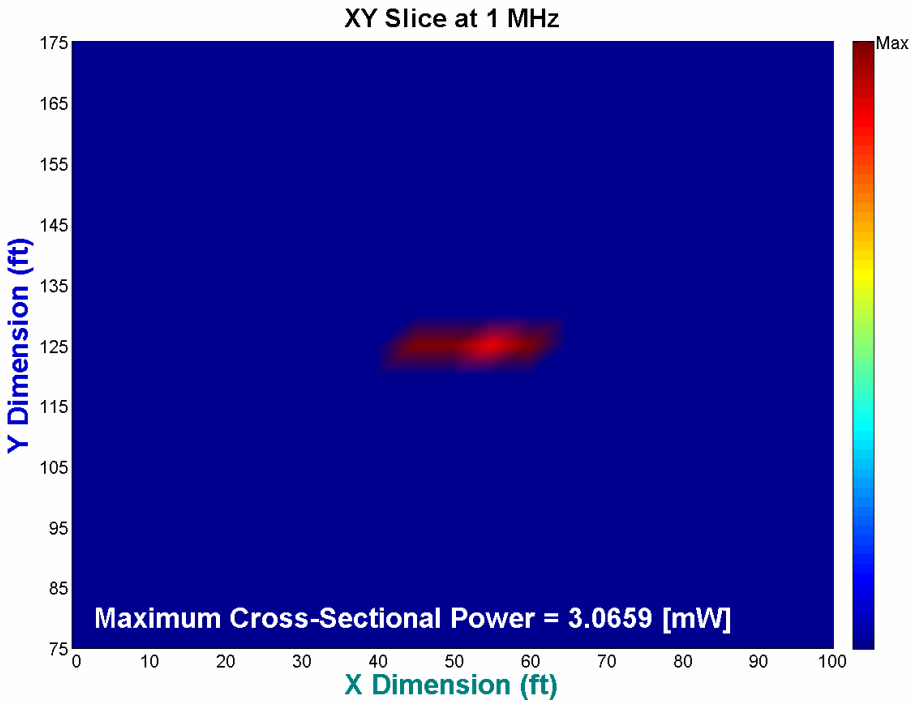

Figure 6.42 2D image of air-filled target at 1 MHz

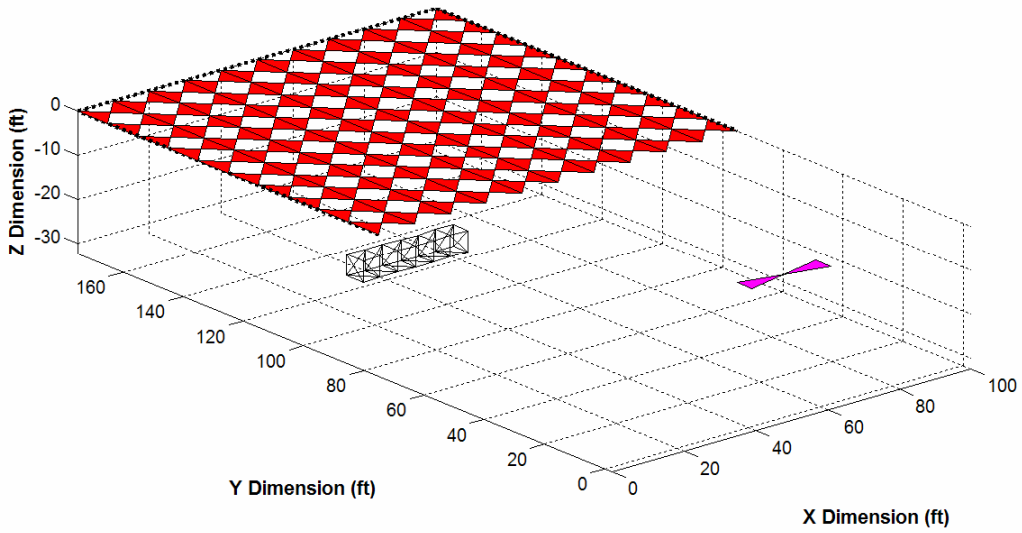

Figure 6.43 Perfectly conducting target at a depth of 30 ft.

Transmitter:
Location: 50’ x 0’ x 0’
Power: 10 W
Frequency: 1MHz

Receiver:
Location: 50’ x 125’ x 0’
Size: 100’ x 100’
Spacing: 10’ x 10’

Target:
Location: 50’ x 75’ x -30’
Size: 5’ x ~30’ x 5’
Perfect Conductor
BRDF Roughness Factor: 0.5
BRDF Isotropy Factor: 0.5

Ground:
Permittivity: 14
Permeability: 1
Conductivity: 2 mS/m

In this scenario, Figure 6.43 depicts a perfectly conducting target placed directly beneath the receiving antennas. The target is buried 30 ft. below the Earth's surface parallel to the X dimension in an assumed homogeneous medium with dielectric permittivity of 14, permeability of 1, and conductivity of 2 mS/m. This medium is characteristic of a fine rocky soil. The transmitting antenna transmits 10 W of power at a frequency of 1 MHz Solid Works allowed the definition of 52 distinct target facets each with an approximate surface area of 1.125 m^2 (12.5 ft^2) and center separation of 1.5 m to satisfy the SAR system resolution requirement. MATLAB 3D interpolation function *griddata3* was used to map the integrated return power acquired for each target facet to its appropriate location in the GPR scene.

The 3D image produced in Figure 6.44 portrays the true target's size and orientation. While the true target was strategically placed to guarantee the occurrence of ITI, STI, and FTI reflections, the vertical offset present in the 3D approximation is attributed to the low power return from the bottom of the target. Although additional target facet locations were recorded to return power, the strength of this power, relative to that returned from the surface of the target limited MATLAB interpolation of target representation in the Z dimension. In the 2D image, shown in Figure 6.45, due to the location of the target, a majority of the energy reflected in the spectral direction is lost. Diffuse reflections are indicated by the evenly distributed intensity across the image from left to right.

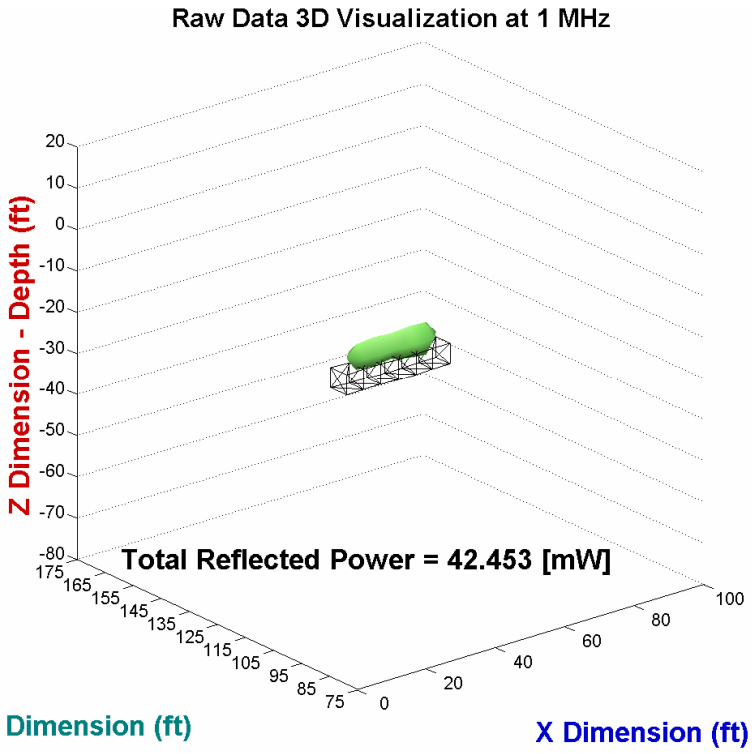

Figure 6.44 3D interpolation of radar return for a perfectly conducting target at 1 MHz

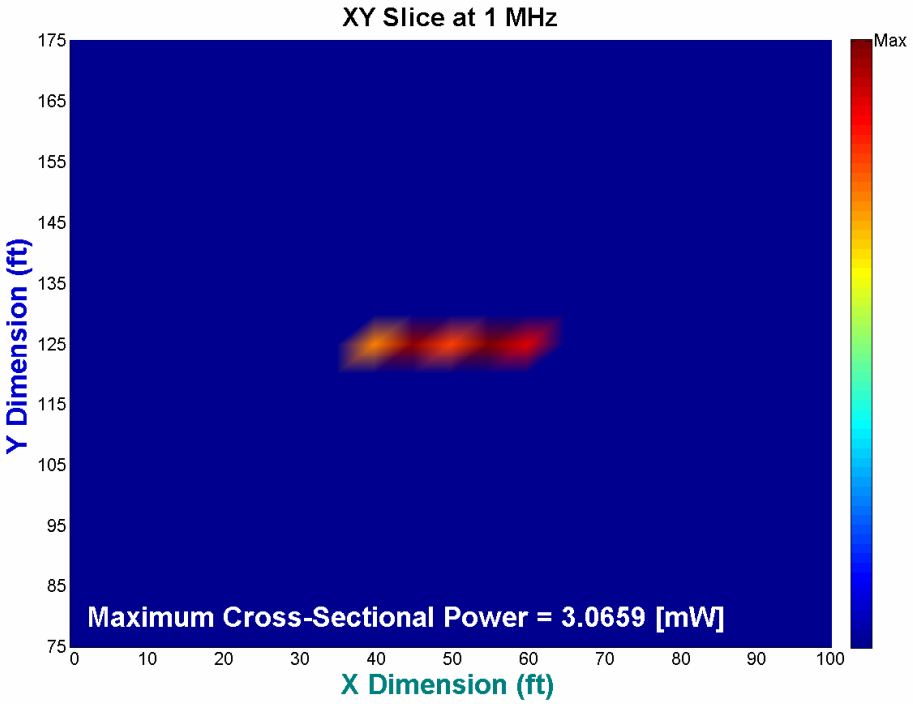

Figure 6.45 2D image of a perfectly conducting target at 1 MHz

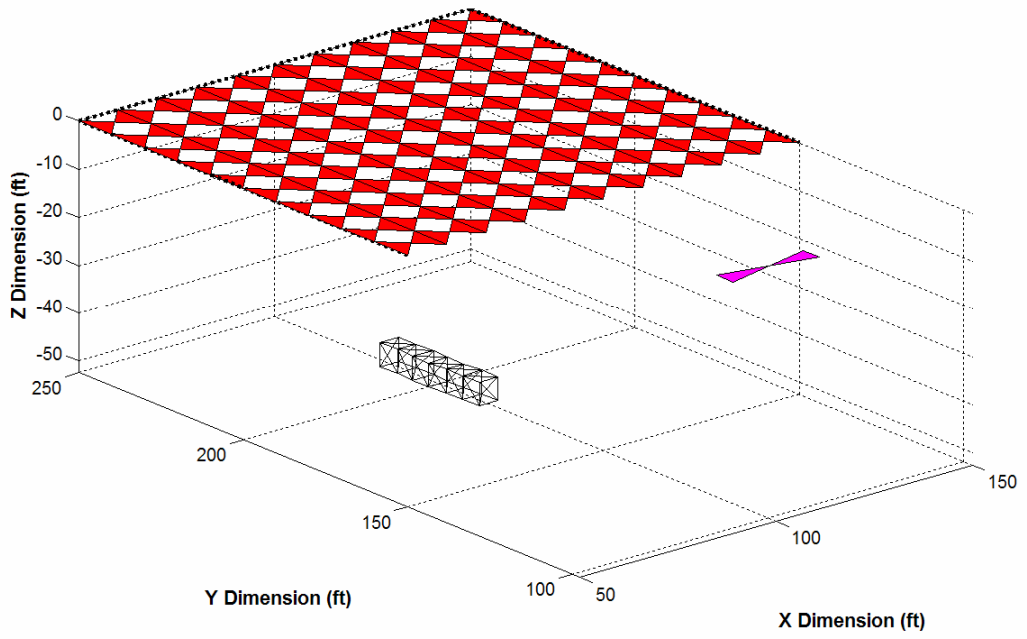

Figure 6.46 Air filled target at a depth of 50 ft. using single transmitter configuration

Transmitter 1:
Location: 100’ x 0’ x 0’
Power: 10 W
Frequency: 1MHz

Receiver:
Location: 100’ x 200’ x 0’
Size: 100’ x 100’
Spacing: 10’ x 10’

Target:
Location: 100’ x 200’ x -50’
Size: 5’ x ~30’ x 5’
Air Filled
BRDF Roughness Factor: 0.5
BRDF Isotropy Factor: 0.5

Ground:
Permittivity: 14
Permeability: 1
Conductivity: 2 mS/m

In this scenario, Figure 6.46 depicts an air filled target placed directly beneath the receiving antennas using a single transmitter. The target is buried 50 ft. below the Earth's surface parallel to the Y dimension in an assumed homogeneous medium with dielectric permittivity of 14, permeability of 1, and conductivity of 2 mS/m. This medium is characteristic of a fine rocky soil. The transmitting antenna transmits 10 W of power at a frequency of 1 MHz Solid Works allowed the definition of 52 distinct target facets each with an approximate surface area of 1.125 m^2 (12.5 ft^2) and center separation of 1.5 m to satisfy the SAR system resolution requirement. MATLAB 3D interpolation function *griddata3* was used to map the integrated return power acquired for each target facet to its appropriate location in the GPR scene.

The 3D image produced in Figure 6.47 portrays the true target's size and orientation. While the true target was strategically placed to guarantee the occurrence of ITI, STI, and FTI reflections, the vertical offset present in the 3D approximation is attributed to the low power return from the bottom of the target . Although additional target facet locations were recorded to return power, the strength of this power, relative to that returned from the surface of the target limited MATLAB interpolation of target representation in the Z dimension. Additionally, there is a diminishing tail effect also cause by weak reflections from the portion of the target located furthest from the transmitter. In the 2D image, shown in Figure 6.48, due to the location of the target, a majority of the energy reflected in the spectral direction is lost. Diffuse reflections are indicated by the diminishing intensity across the image from front to back.

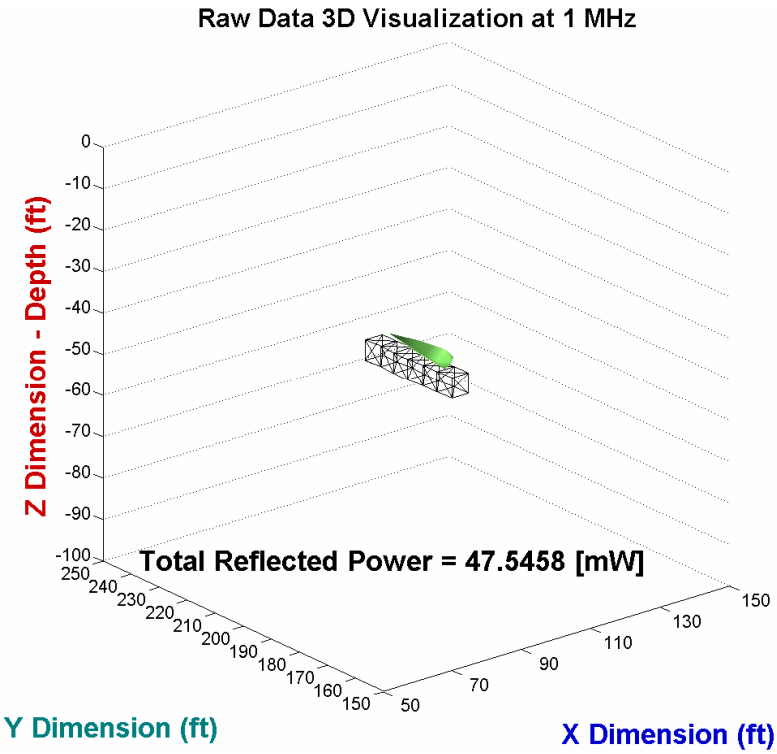

Figure 6.47 3D interpolation of radar return for air-filled target and single transmitter configuration

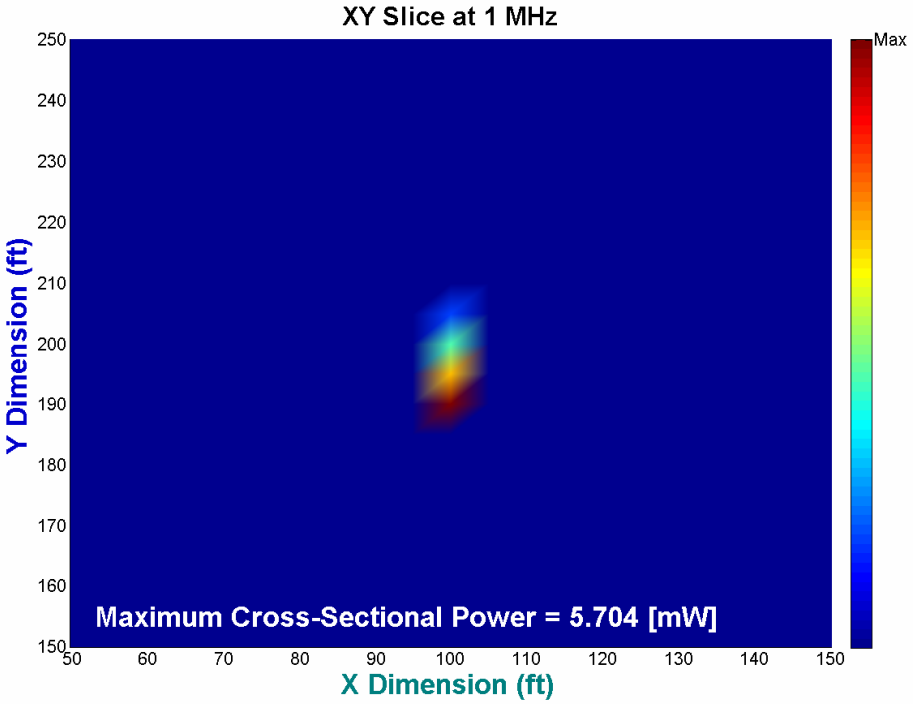

Figure 6.48 2D image of air-filled target and single transmitter configuration

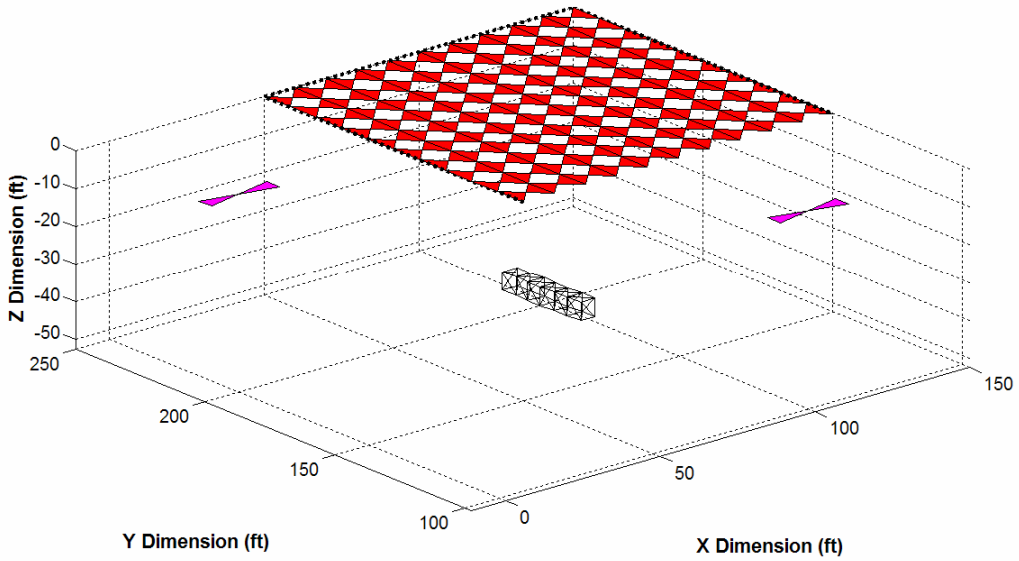

Figure 6.49 Air filled target at a depth of 50 ft. using double transmitter configuration

Transmitter 1:
Location: 100’ x 0’ x 0’
Power: 10 W
Frequency: 1 MHz

Transmitter 2:
Location: 0’ x 200’ x 0’
Power: 10 W
Frequency: 1 MHz

Target:
Location: 100’ x 200’ x -50’
Size: 5’ x ~30’ x 5’
Air Filled
BRDF Roughness Factor: 0.5
BRDF Isotropy Factor: 0.5

Receiver:
Location: 100’ x 200’ x 0’
Size: 100’ x 100’
Spacing: 10’ x 10’

Ground:
Permittivity: 14
Permeability: 1
Conductivity: 2 mS/m

In this scenario, Figure 6.49 depicts an air filled target placed directly beneath the receiving antennas using a double transmitter configuration. The target is buried 50 ft. below the Earth's surface parallel to the Y dimension in an assumed homogeneous medium with dielectric permittivity of 14, permeability of 1, and conductivity of 2 mS/m. This medium is characteristic of a fine rocky soil. The transmitting antenna transmits 10 W of power at a frequency of 1 MHz Solid Works allowed the definition of 52 distinct target facets each with an approximate surface area of 1.125 m^2 (12.5 ft^2) and center separation of 1.5 m to satisfy the SAR system resolution requirement. MATLAB 3D interpolation function *griddata3* was used to map the integrated return power acquired for each target facet to its appropriate location in the GPR scene.

The 3D image produced in Figure 6.50 portrays the true target's size and orientation. The 3D approximation more closely resembles the true target due to the second transmitter providing an additional vantage point in the GPR scene. Additionally, there is a 122% increase in reflected power from the target. MATLAB interpolation of target representation in the Z dimension remains limited. In the 2D image, shown in Figure 6.51, due to the multiple transmitter locations, while a majority of the energy reflected in the spectral direction is lost, there is a more even distribution of diffuse reflections, indicated by the evenly distributed intensity across the image from front to back.

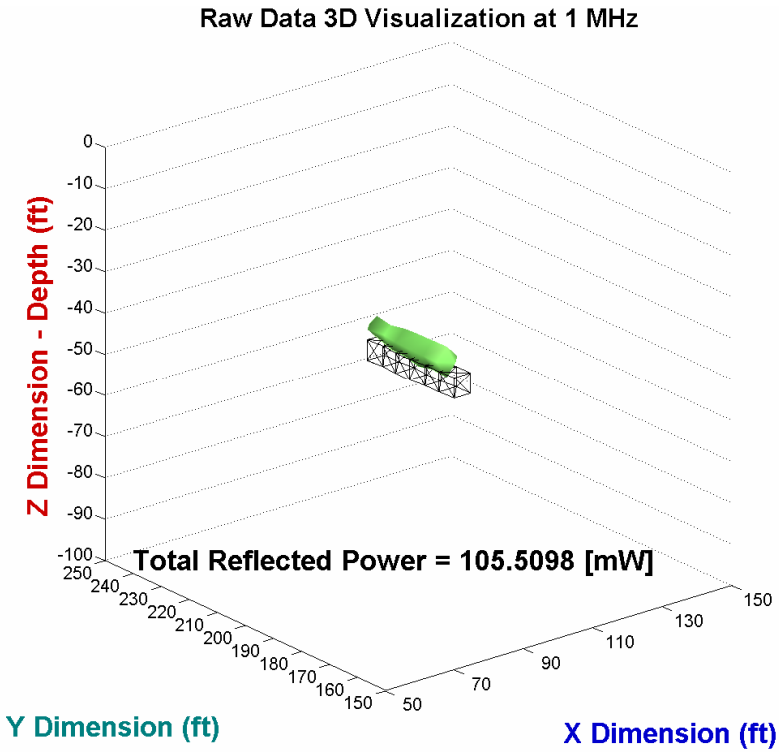

Figure 6.50 3D interpolation of radar return for air-filled target and double transmitter configuration

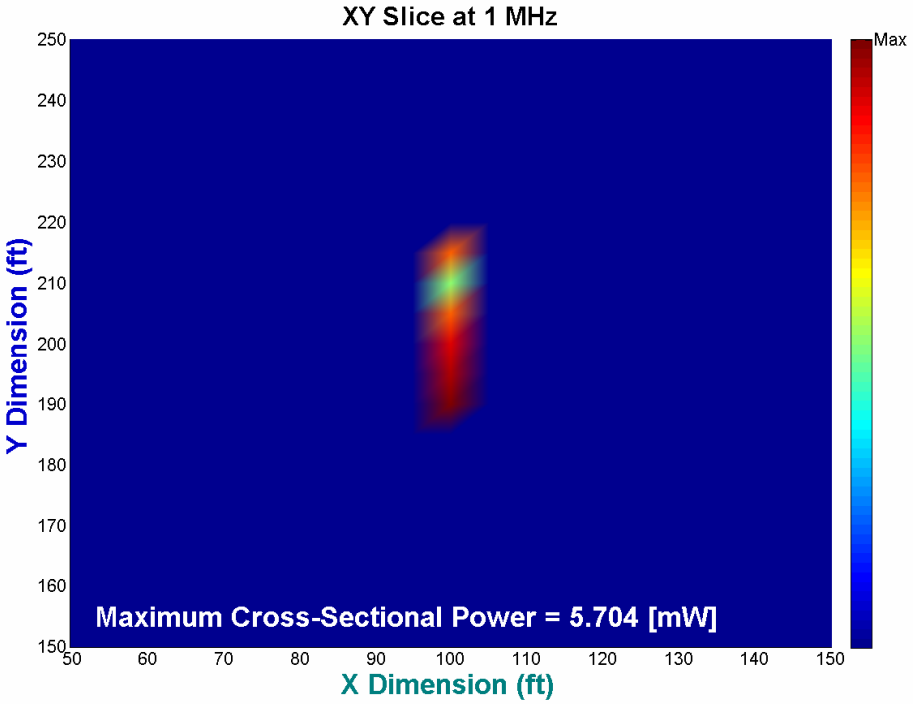

Figure 6.51 2D image of air-filled target and double transmitter configuration

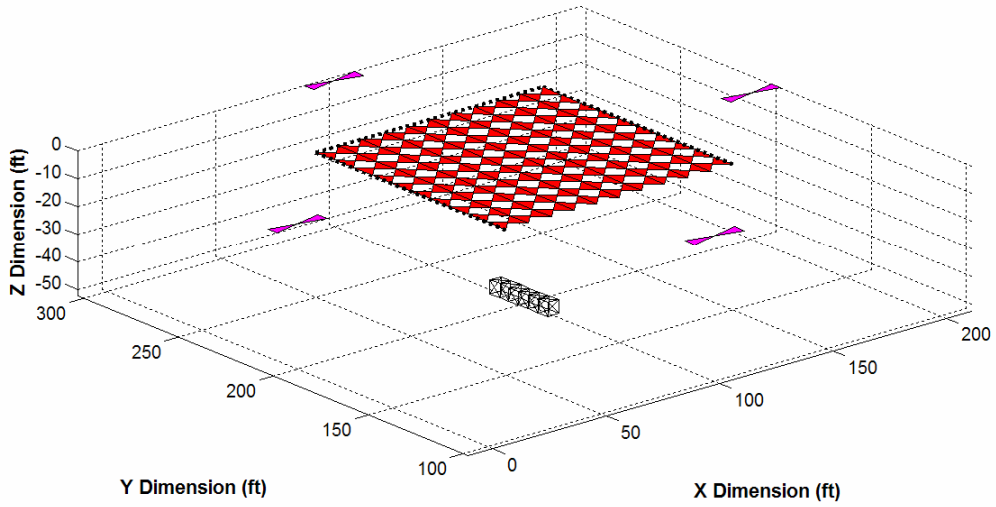

Figure 6.52 Air filled target at a depth of 50 ft. using quadruple transmitter configuration

Transmitter 1:
Location: 100’ x 0’ x 0’
Power: 10 W
Frequency: 1 MHz

Transmitter 2:
Location: 0’ x 200’ x 0’
Power: 10 W
Frequency: 1 MHz

Transmitter 3:
Location: 100’ x 300’ x 0’
Power: 10 W
Frequency: 1 MHz

Transmitter 4:
Location: 200’ x 200’ x 0’
Power: 10 W
Frequency: 1 MHz

Receiver:
Location: 100’ x 200’ x 0’
Size: 100’ x 100’
Spacing: 10’ x 10’

Ground:
Permittivity: 14
Permeability: 1
Conductivity: 2 mS/m

Target:
Location: 100’ x 200’ x -50’
Size: 5’ x ~30’ x 5’
Air Filled
BRDF Roughness Factor: 0.5
BRDF Isotropy Factor: 0.5

In this scenario, Figure 6.52 depicts an air filled target placed directly beneath the receiving antennas using a quadruple transmitter configuration. The target is buried 50 ft. below the Earth's surface parallel to the Y dimension in an assumed homogeneous medium with dielectric permittivity of 14, permeability of 1, and conductivity of 2 mS/m. This medium is characteristic of a fine rocky soil. The transmitting antenna transmits 10 W of power at a frequency of 1 MHz Solid Works allowed the definition of 52 distinct target facets each with an approximate surface area of 1.125 m^2 (12.5 ft^2) and center separation of 1.5 m to satisfy the SAR system resolution requirement. MATLAB 3D interpolation function *griddata3* was used to map the integrated return power acquired for each target facet to its appropriate location in the GPR scene.

The 3D image produced in Figure 6.53 portrays the true target's size and orientation. The 3D approximation more closely resembles the true target due to the additional transmitters providing three extra vantage points in the GPR scene. Additionally, there is a 343% increase in reflected power from the target. MATLAB interpolation of target representation in the Z dimension remains limited. In the 2D image, shown in Figure 6.54, due to the multiple transmitter locations, while a majority of the energy reflected in the spectral direction is lost, there is a varied distribution of diffuse reflections, indicated by the different intensity hues across the image from front to back.

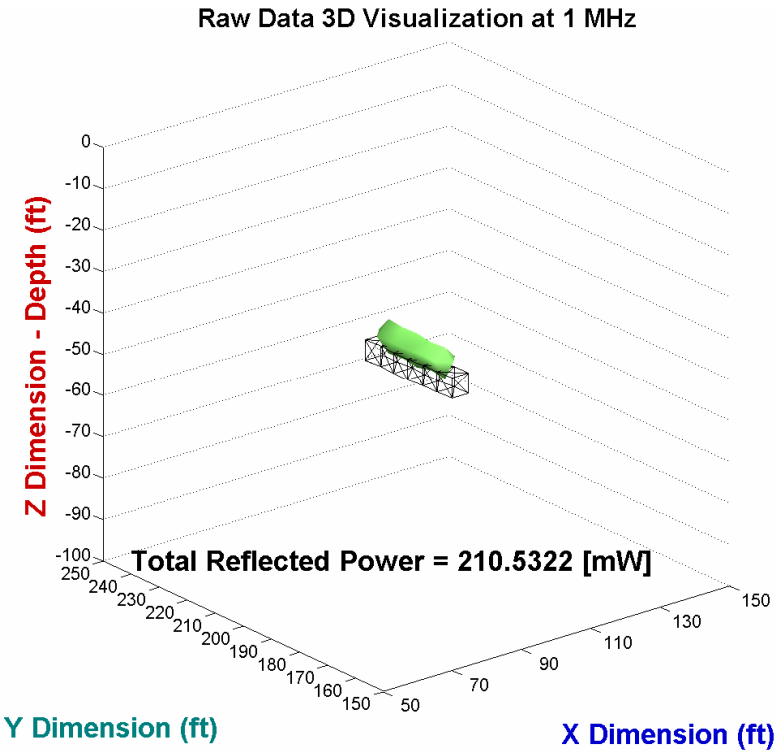

Figure 6.53 3D interpolation of radar return for air-filled target and quadruple transmitter configuration

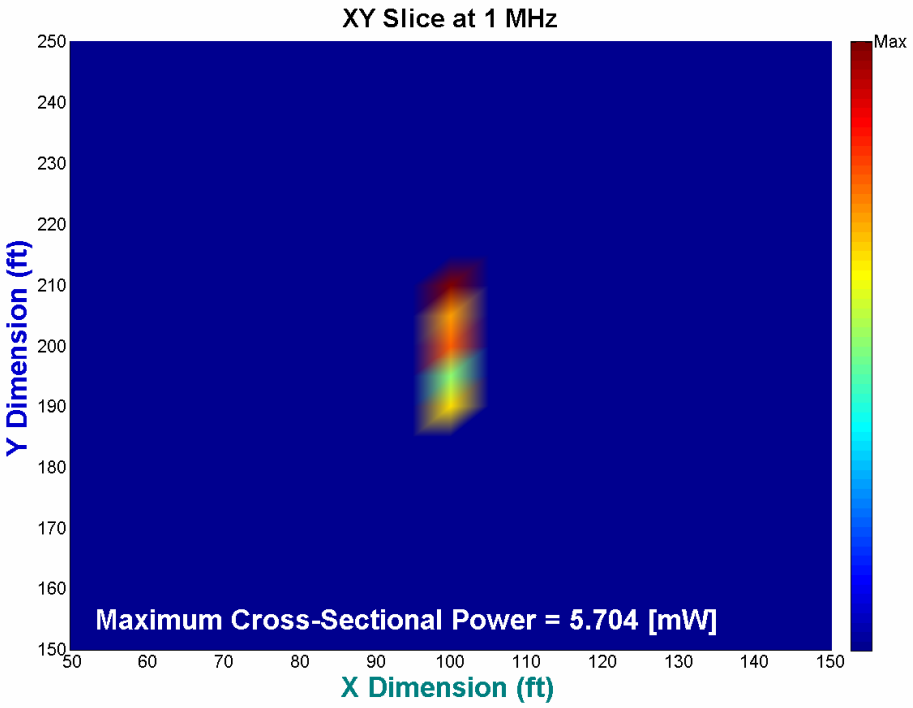

Figure 6.54 2D image of air-filled target and quadruple transmitter configuration

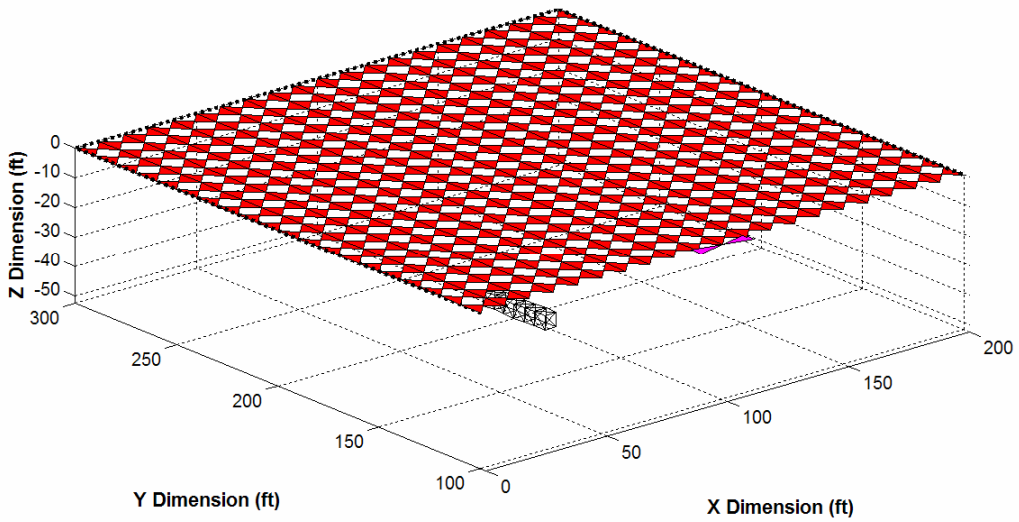

Figure 6.55 Air-filled target buried directly between large receiver array.

Transmitter:
Location: 100’ x 100’ x 0’
Power: 10 W
Frequency: 1 MHz

Receiver:
Location: 100’ x 200’ x 0’
Size: 200’ x 200’
Spacing: 10’ x 10’

Target:
Location: 100’ x 200’ x -150’
Size: 5’ x ~30’ x 5’
Air Filled
BRDF Roughness Factor: 0.5
BRDF Isotropy Factor: 0.5

Ground:
Permittivity: 14
Permeability: 1
Conductivity: 2 mS/m

In this scenario, Figure 6.55 depicts an air filled target placed directly beneath an enlarged receiving array of antennas. The unique configuration allows the reception of power from an increased number of vantage points including the transmitter location. The target is buried 50 ft. below the Earth's surface parallel to the Y dimension in an assumed homogeneous medium with dielectric permittivity of 14, permeability of 1, and conductivity of 2 mS/m. This medium is characteristic of a fine rocky soil. The transmitting antenna transmits 10 W of power at a frequency of 1 MHz Solid Works allowed the definition of 52 distinct target facets each with an approximate surface area of 1.125 m^2 (12.5 ft^2) and center separation of 1.5 m to satisfy the SAR system resolution requirement. MATLAB 3D interpolation function *griddata3* was used to map the integrated return power acquired for each target facet to its appropriate location in the GPR scene.

The 3D image produced in Figure 6.56 portrays the true target's size and orientation. The 3D approximation fails to span the length of the true target in the Y dimension. MATLAB interpolation of target representation in the Z dimension remains limited. The total amount of power detected by the enlarged array is increased by 186% from the original receiver array size (100' x 100'). In the 2D image, shown in Figure 6.57, there is a diminishing distribution of diffuse reflections, indicated by the lessening intensity hues across the image from front to back.

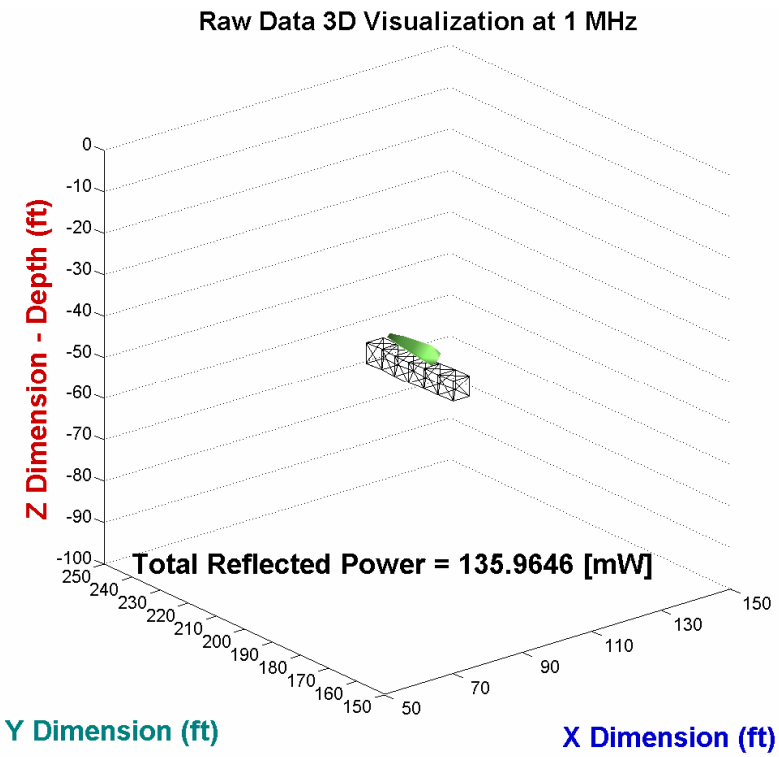

Figure 6.56 3D interpolation of radar return for air-filled target and large receiver array

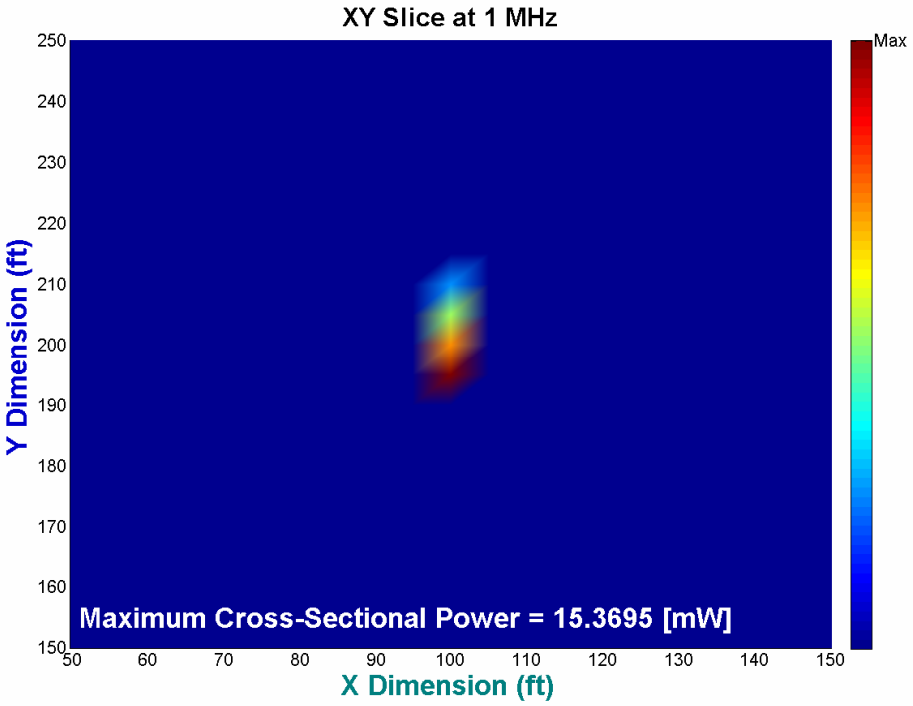

Figure 6.57 2D image of air-filled target and large receiver array

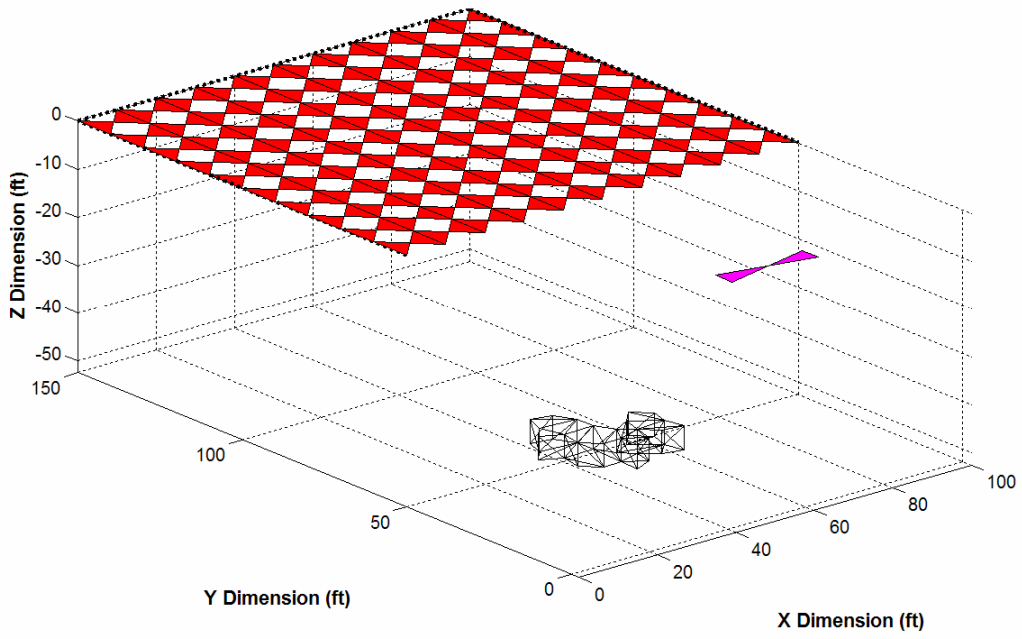

Figure 6.58 Air-filled, awkwardly shaped target buried at a depth of 50 ft.

Transmitter:
Location: 50’ x 0’ x 0’
Power: 10 W
Frequency: 1 MHz

Receiver:
Location: 50’ x 100’ x 0’
Size: 100’ x 100’
Spacing: 10’ x 10’

Target:
Location: 50’ x 50’ x -50’
Size: See Appendix A
Air Filled
BRDF Roughness Factor: 0.5
BRDF Isotropy Factor: 0.5

Ground:
Permittivity: 14
Permeability: 1
Conductivity: 2 mS/m

In this scenario, Figure 6.58 depicts an air-filled, awkwardly-shaped target placed symmetrically between the transmitting and receiving antennas. The target is buried 50 ft. below the Earth's surface in an assumed homogeneous medium with dielectric permittivity of 14, permeability of 1, and conductivity of 2 mS/m. This medium is characteristic of a fine rocky soil. The transmitting antenna transmits 10 W of power at a frequency of 1 MHz. Solid Works allowed the definition of 76 distinct target facets each with an approximate surface area of 1.125 m^2 (12.5 ft^2) and center separation of 1.5 m to satisfy the SAR system resolution requirement. MATLAB 3D interpolation function *griddata3* was used to map the integrated return power acquired for each target facet to its appropriate location in the GPR scene.

The 3D image produced in Figure 6.59 faintly resembles the true target's size and orientation. Here, only ITI reflections occur which result in the vertical offset present in the 3D approximation. MATLAB interpolation of target representation in the Z dimension is also limited. In the 2D image, shown in Figure 6.60, due to the target's unique shape and location, a majority of the energy reflected in the spectral direction is received. Diffuse reflections are indicated by the light orange hue located at the back end of the target. The simulation recorded a total power return of 313.78 mW due to the increased number of facets used to describe the spatially large target. The cross-sectional energy is also significantly increased due to the larger target.

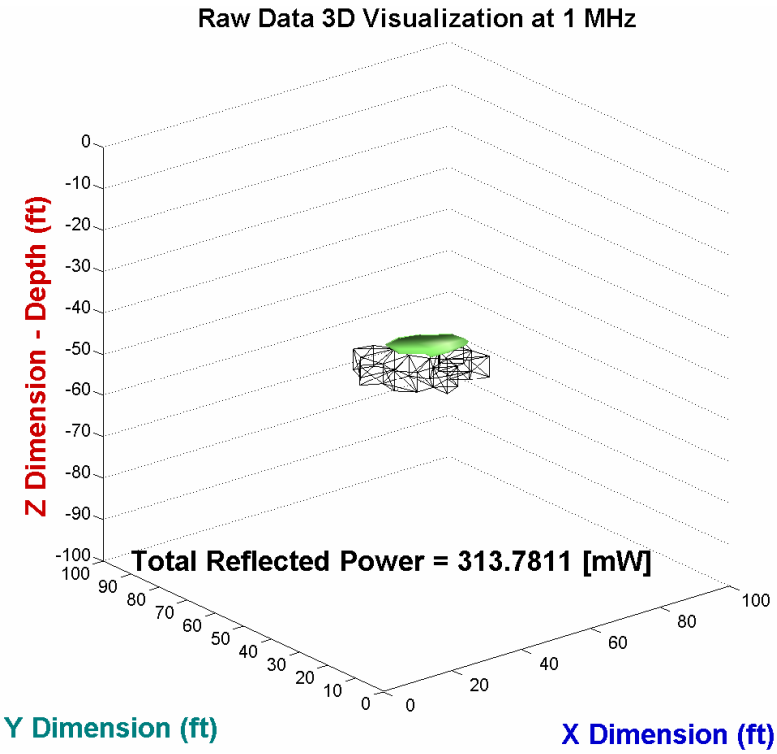

Figure 6.59 3D interpolation of radar return for air-filled awkward target

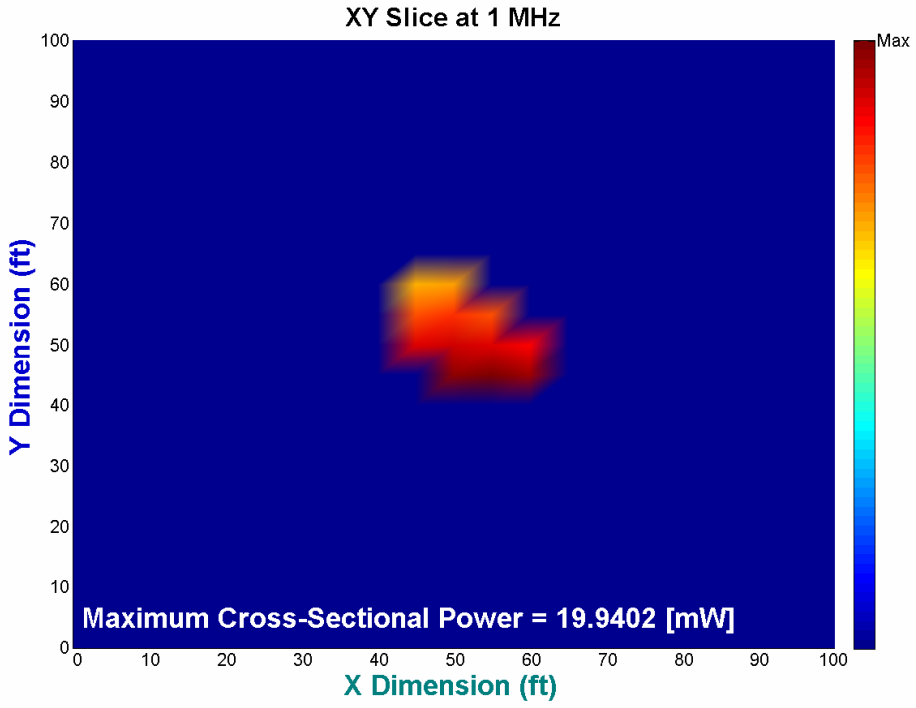

Figure 6.60 2D image of air-filled, awkward target

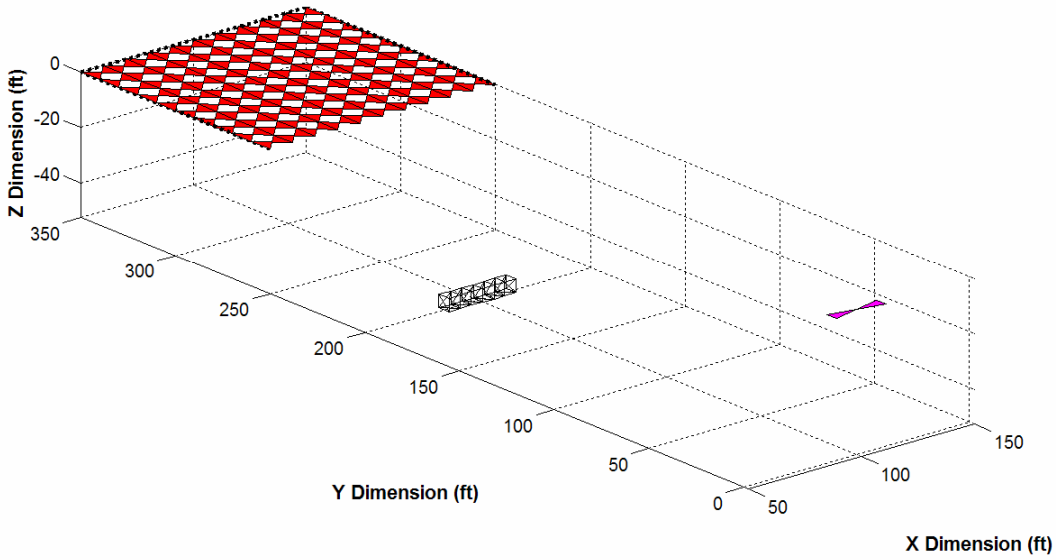

Figure 6.61 Air-filled target buried at a depth of 50 ft.

Transmitter:
Location: 100’ x 0’ x 0’
Power: 10 W
Frequency: 1 MHz

Receiver:
Location: 100’ x 300’ x 0’
Size: 100’ x 100’
Spacing: 10’ x 10’

Target:
Location: 100’ x 200’ x -50’
Size: ~30’ x 5’ x 5’
Air Filled
BRDF Roughness Factor: 0.5
BRDF Isotropy Factor: 0.5

Ground:
Permittivity: 14
Permeability: 1
Conductivity: 2 mS/m

In this scenario, Figure 6.61 depicts an air-filled target placed symmetrically between the transmitting and receiving antennas. The target is buried 50 ft. below the Earth's surface parallel to the X dimension in an assumed homogeneous medium with dielectric permittivity of 14, permeability of 1, and conductivity of 2 mS/m. This medium is characteristic of a fine rocky soil. The transmitting antenna transmits 10 W of power at a frequency of 1 MHz. Solid Works allowed the definition of 52 distinct target facets each with an approximate surface area of 1.125 m^2 (12.5 ft^2) and center separation of 1.5 m to satisfy the SAR system resolution requirement. MATLAB 3D interpolation function *griddata3* was used to map the integrated return power acquired for each target facet to its appropriate location in the GPR scene.

The 3D image produced in Figure 6.62 represents an interpolated set of SAR data produced by the SAR image processor used in the previous target model. The true target is embedded within this image and is surrounded by excess elliptical ambiguity. There is no reflected power information available in this image. The 3D image, shown in Figure 6.63, is produced by the new target model. Due to the target's location, a majority of the energy reflected in the spectral direction is received. Additionally, only ITI reflections occur which result in the vertical offset present in the 3D approximation as well as the failure to represent the target along the X dimension. This is traced back to limitations in the MATLAB interpolation scheme. The new target recorded a total power return of 0.44647 mW. Between these two figures, both images correctly depict the true target and its correct orientation.

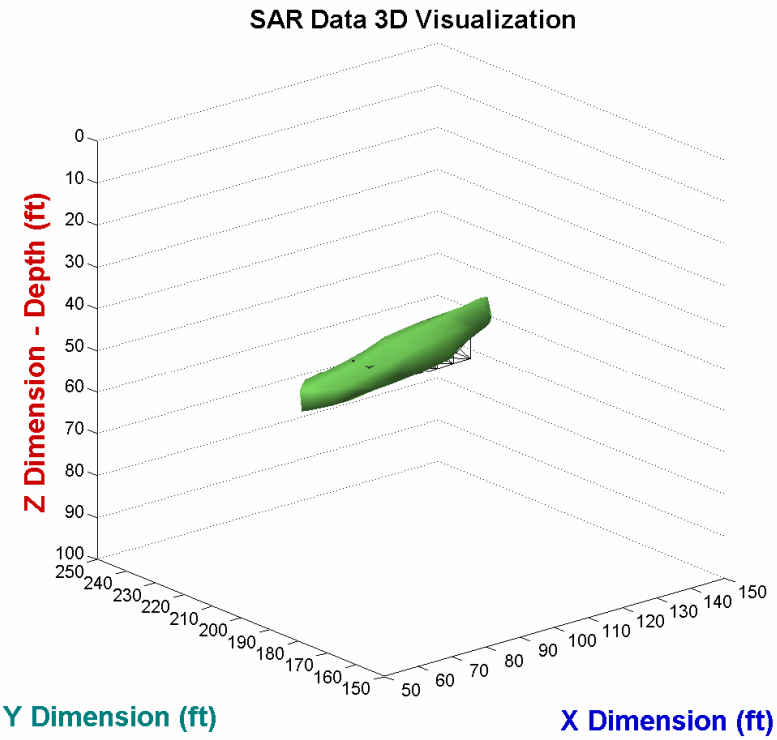

Figure 6.62 3D SAR image produced by previous model

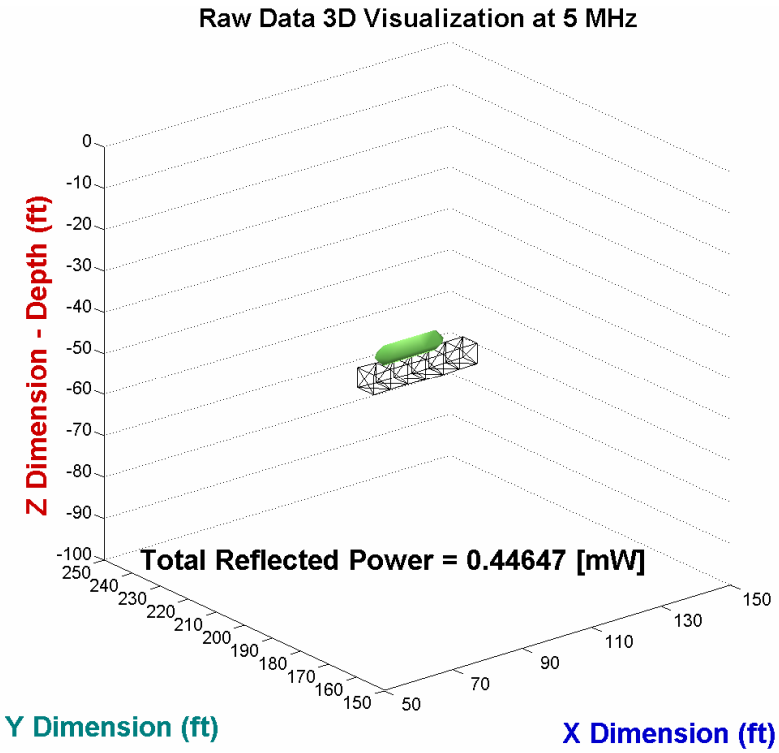

Figure 6.63 3D interpolation of radar return produced by current model

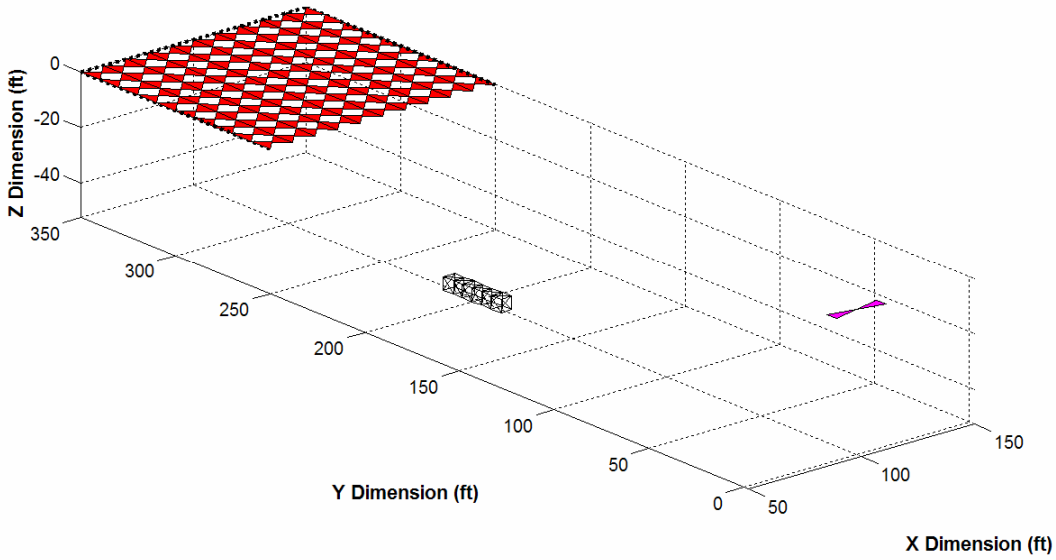

Figure 6.64 Air-filled target buried at a depth of 50 ft.

Transmitter:
Location: 100’ x 0’ x 0’
Power: 10 W
Frequency: 5 MHz

Receiver:
Location: 100’ x 300’ x 0’
Size: 100’ x 100’
Spacing: 10’ x 10’

Target:
Location: 100’ x 200’ x -50’
Size: 5’ x ~30’ x 5’
Air Filled
BRDF Roughness Factor: 0.5
BRDF Isotropy Factor: 0.5

Ground:
Permittivity: 14
Permeability: 1
Conductivity: 2 mS/m

In this scenario, Figure 6.64 depicts an air-filled target placed symmetrically between the transmitting and receiving antennas. The target is buried 50 ft. below the Earth's surface parallel to the Y dimension in an assumed homogeneous medium with dielectric permittivity of 14, permeability of 1, and conductivity of 2 mS/m. This medium is characteristic of a fine rocky soil. The transmitting antenna transmits 10 W of power at a frequency of 5 MHz. Solid Works allowed the definition of 52 distinct target facets each with an approximate surface area of 1.125 m^2 (12.5 ft^2) and center separation of 1.5 m to satisfy the SAR system resolution requirement. MATLAB 3D interpolation function *griddata3* was used to map the integrated return power acquired for each target facet to its appropriate location in the GPR scene.

The 3D image produced in Figure 6.65 represents an interpolated set of SAR data produced by the SAR image processor used in the previous target model. The true target is embedded within this image and is surrounded by excess elliptical ambiguity. There is no reflected power information available in this image. The orientation of the image is also incorrect, highlighting the limitations of the SAR image processor. The 3D image, shown in Figure 6.66, is produced by the new target model and depicts the true target in its correct orientation. Due to the target's location, a majority of the energy reflected in the spectral direction is received. Additionally, the intersection between the 3D approximation and the true target is attributed to return power from ITI, STI, and FTI reflections. This provides multiple vantage points beyond the surface of the target used by the MATLAB interpolation feature despite failing to represent the target along the Y dimension. This is traced back to limitations in the MATLAB interpolation scheme. The new target recorded a total power return of 0.75421 mW.

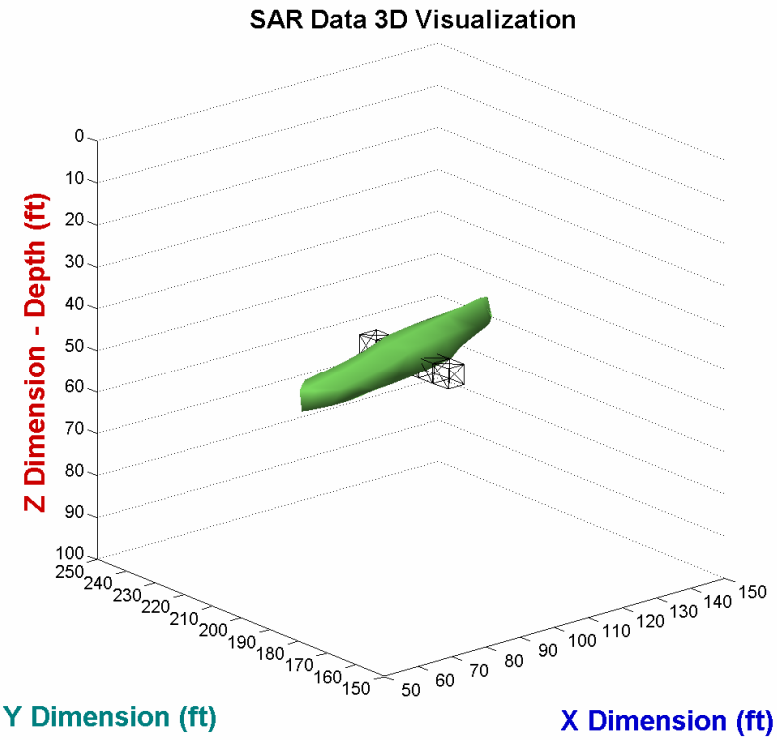

Figure 6.65 3D SAR image produced by previous model, incorrect orientation

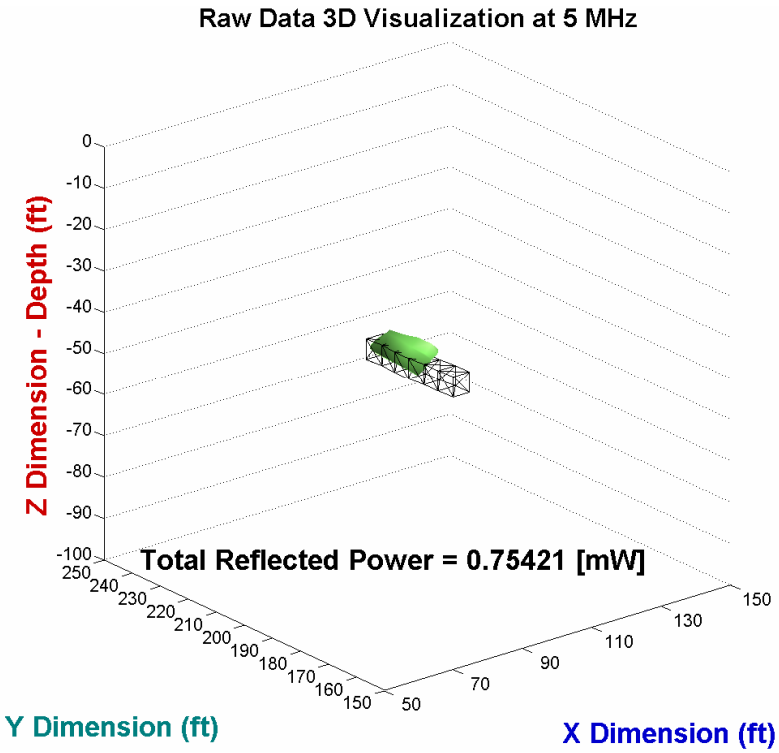

Figure 6.66 3D interpolation of radar return produced by current model, correct orientation

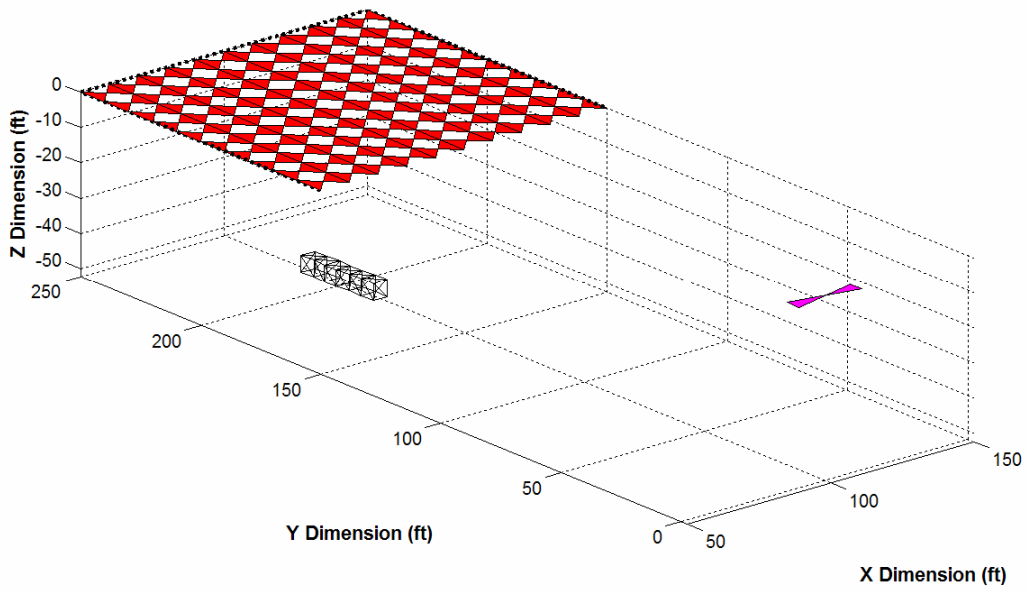

Figure 6.67 Air-filled target buried at a depth of 50 ft.

Transmitter:
Location: 100’ x 0’ x 0’
Power: 10 W
Frequency: 5 MHz

Receiver:
Location: 100’ x 200’ x 0’
Size: 100’ x 100’
Spacing: 10’ x 10’

Target:
Location: 100’ x 200’ x -50’
Size: 5’ x ~30’ x 5’
Air Filled
BRDF Roughness Factor: 0.5
BRDF Isotropy Factor: 0.5

Ground:
Permittivity: 14
Permeability: 1
Conductivity: 2 mS/m

In this scenario, Figure 6.67 depicts an air-filled target placed directly beneath the receiving antennas. The target is buried 50 ft. below the Earth's surface parallel to the Y dimension in an assumed homogeneous medium with dielectric permittivity of 14, permeability of 1, and conductivity of 2 mS/m. This medium is characteristic of a fine rocky soil. The transmitting antenna transmits 10 W of power at a frequency of 5 MHz. Solid Works allowed the definition of 52 distinct target facets each with an approximate surface area of 1.125 m^2 (12.5 ft^2) and center separation of 1.5 m to satisfy the SAR system resolution requirement. MATLAB 3D interpolation function *griddata3* was used to map the integrated return power acquired for each target facet to its appropriate location in the GPR scene.

The 3D image produced in Figure 6.68 represents an interpolated set of SAR data produced by the SAR image processor used in the previous target model. The true target is embedded within this image and is surrounded by excess elliptical ambiguity. There is no reflected power information available in this image. The orientation and shape of the image is also incorrect, highlighting the limitations of the SAR image processor. The 3D image, shown in Figure 6.69, is produced by the new target model and more closely depicts the true target in its correct orientation. Due to the target's location, a majority of the energy reflected in the spectral direction is lost. Additionally, the intersection between the 3D approximation and the true target is attributed to return power from ITI, STI, and FTI reflections. This provides multiple vantage points beyond the surface of the target used by the MATLAB interpolation feature despite failing to represent the target along the Y dimension. This is traced back to limitations in the MATLAB interpolation scheme. The new target recorded a total power return of 1.5021 mW.

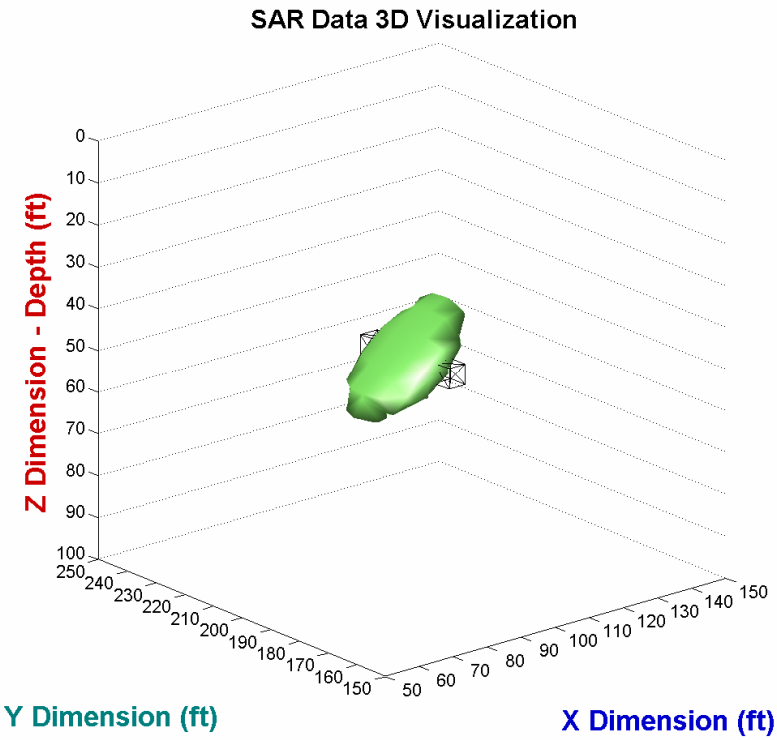

Figure 6.68 3D SAR image produced, unrepresentative and incorrect orientation

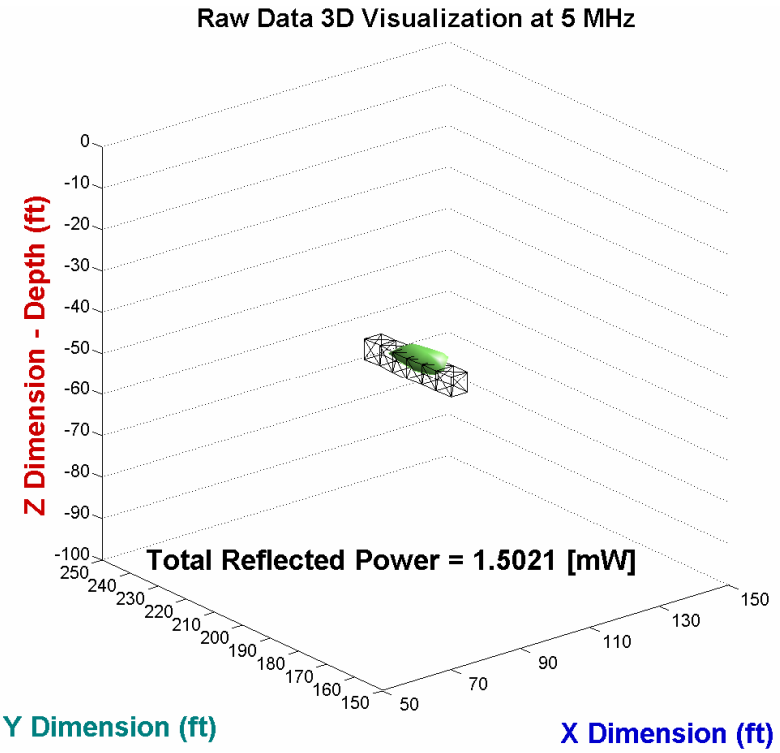

Figure 6.69 3D interpolation of radar return, current model, correct representation and orientation

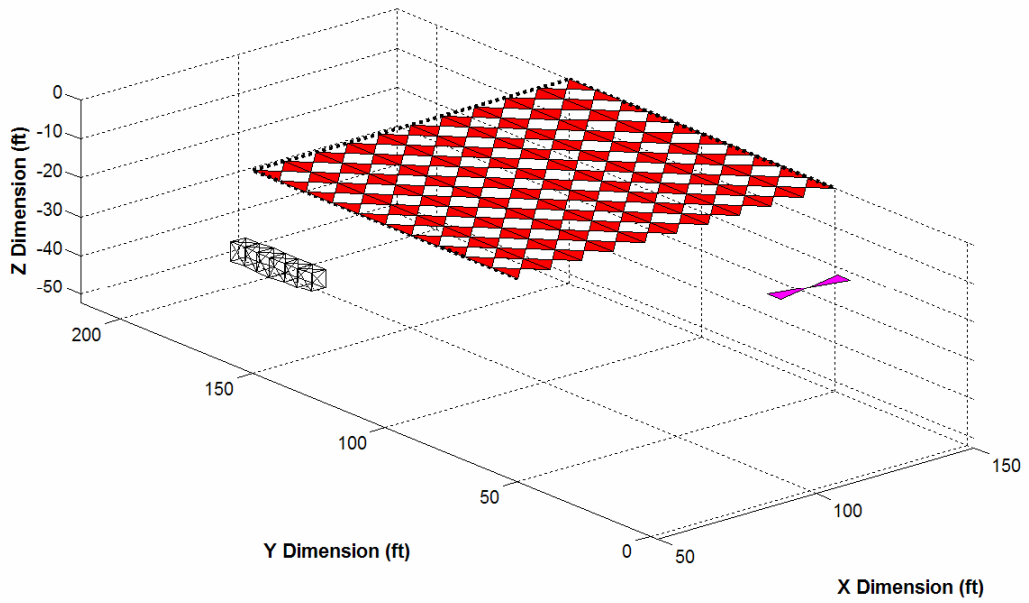

Figure 6.70 Air-filled target buried at a depth of 50 ft.

Transmitter:
Location: 100’ x 0’ x 0’
Power: 10 W
Frequency: 5 MHz

Receiver:
Location: 100’ x 100’ x 0’
Size: 100’ x 100’
Spacing: 10’ x 10’

Target:
Location: 100’ x 200’ x -50’
Size: 5’ x ~30’ x 5’
Air Filled
BRDF Roughness Factor: 0.5
BRDF Isotropy Factor: 0.5

Ground:
Permittivity: 14
Permeability: 1
Conductivity: 2 mS/m

In this scenario, Figure 6.70 depicts an air-filled target placed beyond both the transmitting and receiving antennas. The target is buried 50 ft. below the Earth's surface parallel to the Y dimension in an assumed homogeneous medium with dielectric permittivity of 14, permeability of 1, and conductivity of 2 mS/m. This medium is characteristic of a fine rocky soil. The transmitting antenna transmits 10 W of power at a frequency of 5 MHz. Solid Works allowed the definition of 52 distinct target facets each with an approximate surface area of 1.125 m^2 (12.5 ft^2) and center separation of 1.5 m to satisfy the SAR system resolution requirement. MATLAB 3D interpolation function *griddata3* was used to map the integrated return power acquired for each target facet to its appropriate location in the GPR scene.

The 3D image produced in Figure 6.71 represents an interpolated set of SAR data produced by the SAR image processor used in the previous target model. The true target is embedded within this image and is surrounded by excess elliptical ambiguity. There is no reflected power information available in this image. The orientation and shape of the image is also incorrect, highlighting the limitations of the SAR image processor. The 3D image, shown in Figure 6.72, is produced by the new target model and more closely depicts the true target in its correct orientation. Due to the target's location, a majority of the energy reflected in the spectral direction is lost. Additionally, the intersection between the 3D approximation and the true target is attributed to return power from ITI, STI, and FTI reflections. This provides multiple vantage points beyond the surface of the target used by the MATLAB interpolation feature despite failing to represent the target along the Y dimension. This is traced back to limitations in the MATLAB interpolation scheme. The new target recorded a total power return of 0.5576 mW.

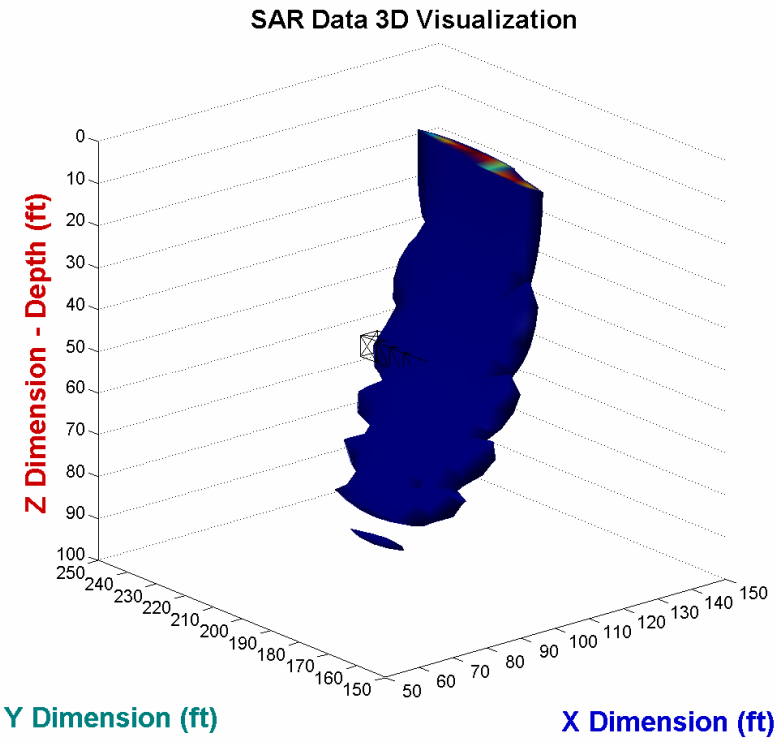

Figure 6.71 3D SAR image, previous model, unrepresentative and incorrect orientation

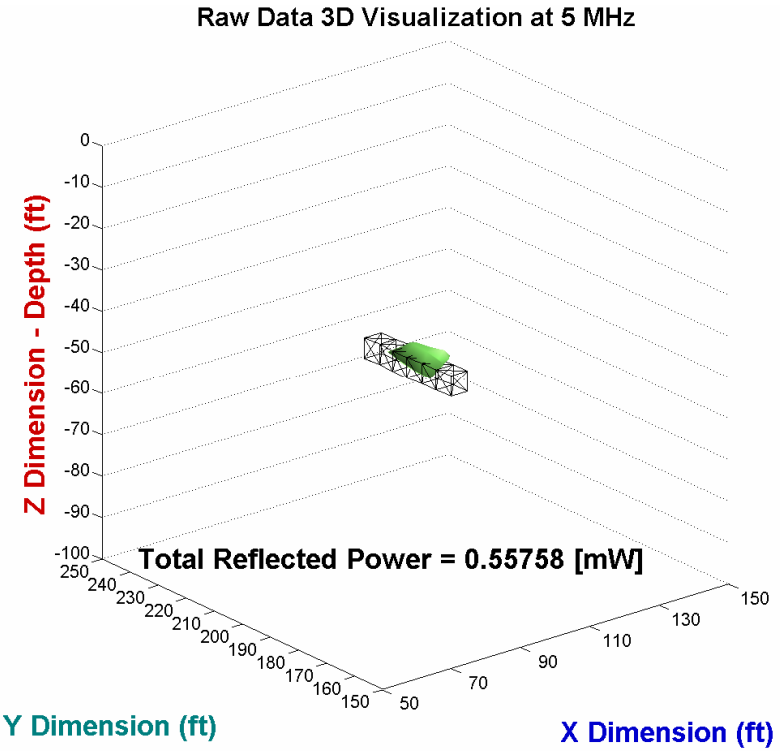

Figure 6.72 3D interpolation of radar return, current model, correct representation and orientation

6.4 Analysis of Results

Improvements made to the GPR target model and its newest features were thoroughly tested in the previous results section. In addition to improvements over the previous model, inherent limitations in the current model were also discovered.

The system frequency range chosen for these simulations [1 – 10 MHz] demonstrated the fidelity of the new target model and its ability to record signal attenuation as a function of frequency. This range can be adjusted to include both higher and lower frequency bands. While frequencies other than HF/VHF are inappropriate for this specific GPR system and its current design, the target model maintains modularity with respect to this feature. Other contributors to the signal attenuation were the target's spatial distance from the transmitter and individual receivers, indicated by the range of return power values. This was successfully shown in the first six sets of results in section 6.3 for two different target locations. As expected, the total return power at the receiver array exponentially decreased as the system frequency increased linearly. Here, as well as throughout the remaining simulations, limitations in the 3D interpolation of return power led to aberrations in representations of the true target. Although the exact locations of return power values were made available to the MATLAB interpolation feature, best approximations prevented the precise re-construction of the true target.

Signal attenuation was also examined by steadily increasing the target depth from 20 to 200 feet while maintaining the same lateral position below the Earth's surface. Keeping the frequency constant allowed a similar exponential attenuation trend to be recorded and is prevalent in the power value displayed for each depth tested.

To affirm that the changes in the target model did not eliminate its fidelity with respect to simulating different homogeneous ground mediums, two different GPR scenes were investigated. The first medium considered was a fine rocky soil with high conductivity and dielectric permittivity. As with most of the results in this chapter, there was a noticeable difference in return power (>70%) when transmitting at the low end frequency [1 MHz] versus signal transmission at the upper end [10 MHz]. As expected, when considering a soil type with a considerably lower conductivity [arid dessert, 50 μS/m], the difference in return power is less than 1 mW. This confirms the target model's ability to accurately represent and record the subterranean physical phenomena for different ground medium properties.

In addition to flexibility in simulating different ground medium, the fidelity of the target model was tested against another model parameter, the target type. Both an air-filled target and a perfect conductor were considered for two separate cases. In each GPR scene, based on its geometry, all three types of energy interactions were exhibited (ITI, STI, and FTI). As expected, the total power determined for the air filled target showed a 4 μW greater return than for the perfectly conducting target. This indicated that, beyond the power received from the surface of each target, the perfectly conducting target nearly expunged any power refracted through its surface. This is in contrast to the air filled target which exhibited a minimal but significant power return due to power refracted beyond its surface.

As a way of investigating the versatility of the target model, experiments were conducted to demonstrate the model fidelity with respect to including multiple transmitter locations. By placing multiple transmitters in the GPR scene, more information about the

shape and size of the target can be obtained since different vantage points allow multiple angles of transmission and reception. In addition to target image improvement, these experiments revealed an expected increase in return power as the amount of total transmitted power increased. This further validates the correct implementation of the target model. Of particular interest is the GPR scene where four transmitters are included in the simulation. No spectral energy is recorded due to the target's location. Instead, the cross-sectional image displays the varied dispersal of energy across the surface of the target indicating the nature of diffuse energy reflections due to transmissions from the four encompassing directions.

To confirm that a larger receiver array will improve the reception of randomly refracted energy, this GPR scenario was considered. The size of the receiver array was doubled and while the interpolated image showed little variation as compared with that obtained for the original 100' x 100' receiver array, the amount of received power increased as expected. This is an added feature of fidelity making the target model more marketable as an effective tool for simulating multiple parameters.

As discussed earlier in Chapter 5, this target model allows the simulation of spatially complex targets. This is provided that the predefined SAR resolution is adhered to with respect to the target facet size. For this system, the antenna size used throughout all experiments was 10', thus a resolution of 5' ($D_{Antenna\ Length}/2$) determined the physical distance between target facets. An arbitrary shape was created in addition to the crimped tunnel used throughout the majority of these simulations. Detailed measurements of this randomly generated shape can be found in Appendix A. The generated image vaguely depicts the awkwardness of the target shape. The significant increase in return power is

attributed to the presence of additional triangular facets (76 total facets) describing the target. The cross-sectional image also illustrates the presence of both specular and diffuse energy reflections. From this information, the model remains consistent in its ability to analyze power return from targets regardless of their shape or size and remains a function of the individually defined target facets.

When considering the remaining results presented in the previous section, each scenario is a measurement of improvement over the previous target model. Availability of power information, target orientation, and accuracy of target representation were investigated through four distinct experiments.

For the first of these simulations, due to the elliptical ambiguity prevalent in results produced by the SAR image processor, the true target is surrounded by excess return. Additionally, the normalization in the pre-image processing stage masks all power return information. In comparison, the new target model provides this power return value in addition to a 3D representation of the target. While the interpolated image does not encompass the entire true target, its location and orientation are correctly represented.

The following simulation highlights the limitation of the previous target model in its ability to correctly distinguish between different target orientations. An extensive study of the previous model's interpolated SAR data was conducted. It was determined that, although two completely different sets of data were produced for a target oriented in two distinct orientations (parallel to the X dimension and parallel to the Y dimension), MATLAB's interpolation of each set of data resulted in the same orientation. This problem was more clearly illustrated when plotted against the true target. The SAR image displayed an orientation which was nearly perpendicular to that of the true target. These

results incited the need for an alternative method of target imaging. The current target model satisfies this need and shows a correctly oriented target image in contrast to the incorrect results from the previous model.

The remaining results demonstrate how variations in the receiver location using the previous target model and the current model drastically differ. Primarily with respect to the accuracy in spatially representing the true target, the current model exhibits a significant improvement in fidelity over the previous model. In the first of these final two GPR scenes, when the receiver array is located directly above the true target, the resulting SAR image produced vaguely depicts the shape of the true target. Its awkward shape and angle highlight the limitations inherent in the SAR image processor and its ability to process unambiguous data. In contrast, there is greater agreement between the true target and the image generated by the current model. Additionally, the return power reflected by the target is available to the end-user.

The final image considers a GPR scene where the receiver array is located more closely to the transmitter. This location allows the collection of any diffuse energy reflections directed back towards the transmitter. The resulting SAR image is nearly indistinguishable and fails to even remotely represent the true target. Consistency is prevalent in the current model by correctly representing a diminished power return based on the receiver location and its inability to detect a significant portion of specular and diffuse reflections.

Chapter 7

Discussion and Conclusions

A majority of work accomplished in this study highlights a restructuring of geometric target analysis. This analysis was necessary to simulate the complicated subsurface energy interactions in the GPR scene. With it, comes the ability to simulate spatially complicated extended targets as well as versatile hardware configurations. In addition to controlling antenna directivity through individual ray manipulation and orientation, many of the desired features of a comprehensive GPR target model have been successfully implemented.

7.1 GPR Simulation

By temporarily removing the Pre-Image and SAR processing stages from the current target model, the elliptical ambiguity created by the previous model no longer limits the correct user output. To date, this target model can provide an end user with accurate return power information along with a noiseless visual representation of an energy-reflecting target beneath the earth's surface. The parameters in the software remain user friendly and accessible through a graphical user interface (GUI). Once additional fidelity is incorporated, a marketable software package will be ready for those interested in GPR applications.

7.2 Future Work

Several steps are expected to be taken in order to further improve the current model as well as ameliorate existing faults. With respect to ensuing improvements, the inclusion of WIPL-D software will further improve the fidelity of the target model. This

will enable detailed electromagnetic analysis of the GPR scene to take place relative to variable antenna radiation patterns and custom directivity.

Due to the highly parametric nature of the current target model, exercising variations in these parameters will provide greater insight into the model's limitations. Evaluating the results of different GPR scenarios as a function of these parameters will assist in emphasizing the most promising conditions for field testing. AFRL is currently planning to implement airborne scenarios which will require the same versatility in simulation that this target model offers. Since airborne receiver grid is not an easily accomplished task, having the ability to receive reflected power from multiple scattered locations is a desired simulation parameter. Considering buried transmitters is another additive benefit that this model can easily implement.

The results presented in this work assume a homogeneous medium through which a signal propagates. In a real world scenario, the earth is layered and all energy interactions in a high fidelity target model should account for multiple ground mediums. This will significantly affect the velocity of the transmitted signal and therefore augment the complexity of ray analysis. With this in mind, it is expected that additional frameworks beyond ITI-STI-FTI analysis will need to be added to the current model.

To address the lacking detail in the 3D images presented in Chapter 6, improvements should include producing a more accurate set of data points for MATLAB to use in the interpolation process. The scattered data points currently available prevent a consistent 3D image from being rendered scene to scene.

With all these considerations, a valid target model will improve insight into the design of an efficient signal and SAR image processor that can effectively interpret the

type of raw data collected by the model. Once this takes place, more realistic GPR scenarios can be considered where noise becomes an added parameter. These improvements have an extended lifetime and given the proper attention can significantly impact the design and development of GPR hardware systems.

Bibliography and Citation Index

[1] James W. Jeter, *A Three-Dimensional Ray Tracing Simulation of A Synthetic Aperture Ground Penetrating Radar System*, Rochester Institute of Technology, August 2002.

[2] Toru Sato, Toshio Wakayama, and Kazuhisa Takemura, "An Imaging Algorithm of Objects Embedded in a Lossy Dispersive Medium for Subsurface Radar Data Processing", IEEE Transactions on Geoscience and Remote Sensing, Vol. 38, No. 1, January 2000.

[3] Jun Cai and George A. McMechan, "Ray-Based Synthesis of Bistatic Ground-Penetrating Radar Profiles", Geophysics, Vol. 60, No. 1, January-February 1995.

[4] Dean Goodman, "Ground-Penetrating Radar Simulation in Engineering and Archeology", Geophysics, Vol. 59, No. 2, February 1994.

[5] Merrill I. Skolnik, *Introduction to Radar Systems, Third Edition*, McGraw Hill, New York, 2001.

[6] A. G. Yarovoy and L. P. Ligthart, "Ultra-Wideband Antennas for Ground Penetrating Radar", Proc. International Symposium on Antennas for Radar Earth Observation, Symposium, Delft University of Technology, The Netherlands, 2000.

[7] R. V. de Jongh, A. G. Yarovoy, L. P. Ligthart, I. V. Kaploun, and A. D. Schukin, "Design and analysis of new GPR antenna concepts", Proc. GPR '98, 7th International Conference on Ground Penetrating Radar, Vol. I, Lawrence, Kansas, USA, 1998.

[8] A. A. Lestari, A. G. Yarovoy, and L. P. Ligthart, "An efficient ultra-wideband bow-tie antenna", Proc. Of the 31st European Microwave Conference, London, UK, 2001.

[9] A. A. Lestari, A. G. Yarovoy, and L. P. Ligthart, "Adaptive Antenna for Ground Penetrating Radar", Proc. GPR 2000, SPIE vol. 4084, 8th International Conference on Ground Penetrating Radar, Gold Coast, Australia, 2000, pp. 366-371.

[10] A. A. Lestari, A. G. Yarovoy, and L. P. Ligthart, "Adaptive Capabilities of a wire bow-tie antenna for ground penetrating radar", AP-S 2001 Digest, IEEE International Antennas and Propagation Symposium, vol. 2, Boston, MA, USA, 2001, pp. 564-567.

[11] Robert M. Kapfer, *An Advanced Specular and Diffuse Bidirectional Reflectance Distribution Function Target Model for a Synthetic Aperture Ground Penetrating Radar*, Rochester Institute of Technology, January 2005.

[12] Robert L. Cook, and Kenneth E. Torrance, "A Reflectance Model for Computer Graphics", Computer Graphics, Vol. 15, No. 3, August 1981.

[13] David K. Cheng, Field and Wave Electromagnetics, Second Edition, Addison-Wesley Publishing Company, New York, NY, 1992.

[14] Robert M. Kapfer, "Path Attenuation in Ground Penetrating Radar System", Rochester Institute of Technology, Rochester, NY, August 2003.

[15] Constantien A. Balanis, *Antenna Theory 2nd Edition*, New York: John Wiley & Sons, Inc, 1997.

[16] Andrew S. Glassner, *Introduction to Ray Tracing*, Academic Press Inc., San Diego, California, 1989.

[17] Petr Beckmann, “Shadowing of Random Rough Surfaces”, IEEE Transactions on Antennas and Propagation, May 1965, pages 384-388.
[18] Petr Beckmann, “Scattering by Non-Gaussian Surfaces”, IEEE Transactions on Antennas and Propagation, Vol. AP-21, No. 2, March 1973.
[19] K. E. Torrance and E. M. Sparrow, “Theory for Off-Specular Reflection from Roughened Surfaces”, Journal of the Optical Society of America, Vol. 57, No. 9, September 1967.
[20] Bui Tuong Phong, “Illumination for Computer Generated Pictures”, Communications of the ACM, Vol. 18, No. 6, June 1975.
[21] Christophe Schlick, “A Customizable Reflectance Model for Everyday Rendering”, Fourth Eurographics Workshop on Rendering (Paris, France), June 1993, p. 73-83.
[22] Christophe Schlick, “An Inexpensive BRDF Model for Physically-Based Rendering”, Computer Graphics Forum, Vol. 13, Issue 3, 1994, p. 233-246.
[23] Michael Ashikhmin and Peter Shirley, “An Anisotropic Phong BRDF Model”, Journal of Graphics Tools, v. 5, No. 2, 2000, p. 25-32.
[24] Peter N Saveskie, “Earth Constants”, TAI Inc. Consuletter International, Vol. 6, No. 5.
[25] P. Roberts, “Electrical and magnetic properties of materials”, Artech House, 1988. [p.458].
[26] N. J. Hartsock, T. G. Mueller, G. W. Thomas, R. I. Barnhisel, K. L. Wells, and S. A. Shearer, “Soil Electrical Conductivity Variability”, Proc. 5th International Conference on Precision Agriculture, ASA Misc. Pbl., ASA, CSSA, and SSSA, Madison, WI, 2000.
[27] J. Fitch, *Synthetic Aperture Radar,* New York: Springer-Verlag, 1988.
[28] David Halliday, Robert Resnick, and Jearl Walker, Fundamentals of Physics, Fifth Edition, John Wiley & Sons, Inc., New York, 1997.
[29] Russell D. Brown, Braham Himed, E. Douglas Lynch, and Michael C. Wicks, “Thinned Arrays for Ground Penetrating Imaging Radar,” US Air Force Research Laboratory Sensors Directorate, Radar Signal Processing Branch.
[30] John Parker Burg, Maximum Entropy Spectral Analysis, Ph. D. Thesis, Stanford University, May 1975.
[31] Russell Brown, Jerry Genello, Douglass Lynch, et all, “System Survey of Deep Penetrating Radar,” Presented at the 10th International Conference on Ground Penetrating Radar, 21-24 June 2004, Delft, The Netherlands.

Appendix A

Awkward Target

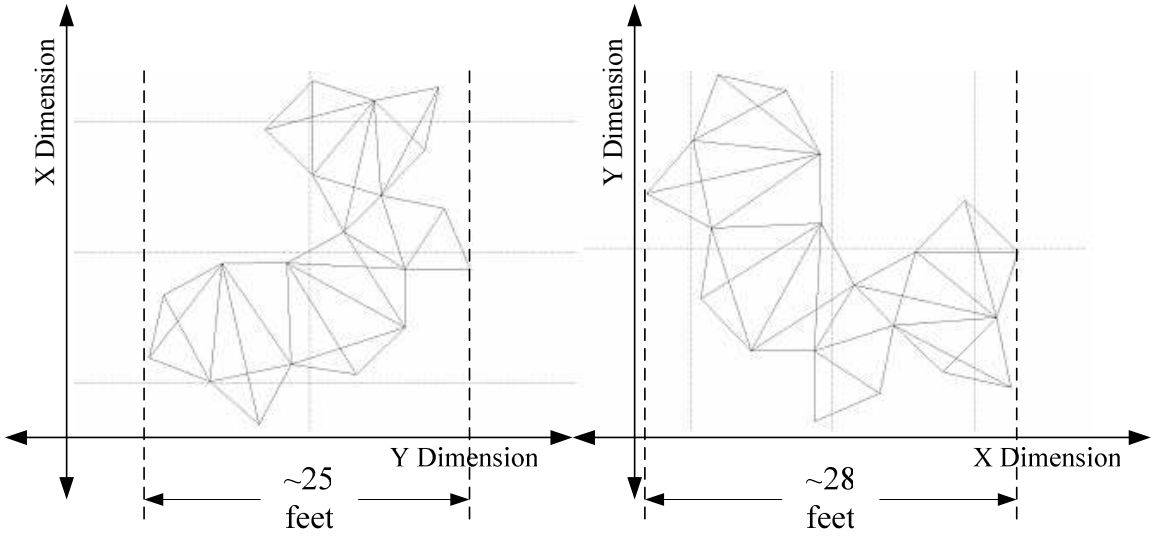

NOTE: Target height dimension is 5’